THE USE OF X-RAY PULSARS FOR AIDING GPS SATELLITE ORBIT

DETERMINATION

THESIS
Dennis W. Woodfork, II
Captain, USAF

AFIT/GA/ENG/05-01

DEPARTMENT OF THE AIR FORCE

AIR UNIVERSITY

AIR FORCE INSTITUTE OF TECHNOLOGY

Wright-Patterson Air Force Base, Ohio

AFIT/GA/ENG/05-01

THE USE OF X-RAY PULSARS FOR AIDING GPS SATELLITE ORBIT DETERMINATION

THESIS

Presented to the Faculty

Department of Electrical and Computer Engineering

Graduate School of Engineering and Management

Air Force Institute of Technology

Air University

Air Education and Training Command

In Partial Fulfillment of the Requirements for the

Degree of Master of Science in Astronautical Engineering

Dennis W. Woodfork, II, B.S.A.E.

Captain, USAF

March 2005

AFIT/GA/ENG/05-01

THE USE OF X-RAY PULSARS FOR AIDING GPS SATELLITE ORBIT DETERMINATION

Dennis W. Woodfork, II, B.S.A.E.

Captain, USAF

Approved:

_____//SIGNED//_____	___1 Mar 05___
Dr. John F. Raquet	date
(Chairman)	
_____//SIGNED//_____	___1 Mar 05___
Dr. Robert A. Racca	date
(Member)	
_____//SIGNED//_____	___1 Mar 05___
Dr. William E. Wiesel	date
(Member)	
_____//SIGNED//_____	___1 Mar 05___
Dr. Juan R. Vasquez, Lt Col, USAF	date
(Member)	

Acknowledgements

First and foremost, I want to extend my thanks to God, my wife, and daughter. Without God's guidance, love, and inspiration, I would certainly not be in a position to achieve my life's goals. To my much neglected family, I want to express my everlasting gratitude. My wife taught me the true meaning of love with her undying devotion and sacrifice. My daughter, with her toothless smile, kept me focused on the important things in life. Thank you both for loving me even when I didn't deserve it.

I also want to thank my family for their extended love and support. Their help with little newborn enabled me to concentrate on graduating. We will always be grateful.

I absolutely need to thank Dr. Robert Racca for all that he has done to help me in my technical career. The endless hours of late night conversations, counseling sessions, and advice on life were more valuable to me than any knowledge I gleaned from the classes I took here. Professionally, all that I am today I owe to your time and guidance.

Thanks to my advisor, Dr. John Raquet, for his wealth of knowledge and insight that guided this research. His encouragement and faith taught me that I was capable of much more than I ever thought possible.

Thanks to Dr. Paul Ray of the Naval Research Lab and Suneel Sheikh of the University of Maryland for entertaining all of my inane and ignorant questions about pulsars. Without their technical guidance, this thesis would not have been possible.

I certainly cannot exclude my fellow astro students who suffered through these past 18 months with me. I'll see you all again when we're back for IDE in a few years!!!

Thank you to my thesis committee for helping to mold my research into a product I can be proud of and to Dr. Chuck Leakeas for the endless hours of Latex help.

Dennis W. Woodfork, II

Table of Contents

ix

AFIT/GA/ENG/05-01

Abstract

Currently, the dominant single-point GPS positioning error sources for military (and some civilian) users are satellite position and clock error. Any improvement in satellite and clock accuracy results in a direct benefit to the user. This research proposes the use of an existing "signal of opportunity" – namely x-ray pulsars – to improve the accuracy and robustness of the GPS satellite and clock estimation algorithm.

A simulation has been developed to determine the effects of using x-ray pulsar measurements on the GPS Operational Control Segment. This simulation uses a nonlinear batch least-squares approach to estimate the position, velocity, and clock errors of all satellites in the specified GPS constellation at a particular epoch time. Both pseudorange measurements and time-difference-of-arrival (TDOA) measurements from pulsars are generated and used. The primary measure of accuracy is a constellation Signal-In-Space Range Error (SISRE).

Results indicate that marginal SISRE improvements (approximately 1%) can be achieved if the x-ray detector is accurate to an order of approximately 40 m for the strongest pulsar. However, increasing the accuracy of the x-ray detector by a factor of 100 can yield accuracy improvements up to 26% over the pseudorange-only based GPS system. Additionally, results show that using only 1 strong pulsar to create TDOA observations, may be equivalent to or better than using tens of pulsars with very weak measurement error statistics. An analysis of the effects of pulsar geometry showed that the geometry does have a significant impact on the overall system performance. Finally, the results indicate that using TDOAs in the absence of pseudoranges for a limited amount of time may aid the OCS in keeping track of the GPS satellites until the ground station links to the constellation can be reestablished. Preliminary analysis shows that the benefits of implementing a TDOA scheme is evident for outage intervals of 20 hours or more.

THE USE OF X-RAY PULSARS FOR AIDING GPS SATELLITE ORBIT DETERMINATION

I. Introduction

1.1 Overview

The Navstar Global Positioning System (GPS) was originally designed to deliver to the United States (US) forces a service that could accurately measure their position, time, and velocity anywhere on the planet and thus provide a distinct military advantage. However, GPS has become an integral part of all our lives since initial operational capability was declared on December 8, 1993 [31]. Areas of influence for GPS range from vehicle navigation to outdoor sportsman activities to international banking operations. In the past decade we have seen an increase and even acceleration of commercial and military applications for GPS. Thus, the requirement for a more precise GPS system is growing. Increasing the accuracy of each satellite position estimate, via the GPS Operational Control Segment (OCS), will result in improvements to military and commercial users' estimates of position, velocity, and time.

1.2 Motivation

This thesis is concerned with the task of increasing GPS navigation accuracy for all users by decreasing the effects of two satellite based errors: ephemeris error and satellite clock error. The GPS constellation of satellites encode and broadcast orbital information, known collectively as the ephemeris, and clock error information down to GPS receivers in two levels of service: Standard Positioning Service (SPS) and Precise Positioning Service (PPS). The SPS signal is primarily used by the global civilian and commercial sectors while PPS is primarily reserved for US (DoD) and (NATO) military operations. The navigation accuracy of the GPS system is dependent upon each satellite having a good estimate of GPS constellation time as well as its own

present position [14]. In order to maintain its specified accuracy requirements of 16 m
50% spherical error probable (SEP)and 100 m 95% 2D-RMS (root mean square) for
the PPS and SPS systems respectively [37], the OCS routinely predicts best estimates
of the current GPS time and satellite positions. Subsequently, the ephemeris and clock
error estimates are uploaded to each satellite on a daily basis [14]. By calculating an
accurate ephemeris, the OCS can precisely estimate the absolute positions of all GPS
satellites. Improving the navigation (ephemeris and clock error) estimates of the GPS
constellation will be directly beneficial to the US military user because the position
and clock errors uplinked to the satellites by the OCS make up the largest error source
degrading the positioning accuracy of GPS for the military PPS signal [31]. Table 1.1
lists the error components of the PPS signal for a typical receiver.

Table 1.1:   GPS Signal Error Sources

Error Source	Typical Range Error Magnitude (meters,1σ) for PPS Receiver
Ionospheric	0.01
Tropospheric	0.7
Clock and Ephemeris Error	3.6
Receiver Noise	0.6
Multipath	1.8

The ephemeris and clock error in Table 1.1 can be quantified as the space-based
component of the PPS signal's error. Together, the GPS satellites' ephemeris and
clock based errors can be quantified as the Signal-In-Space Range Error (SISRE).
SISRE is a measure of the fidelity of the navigation messages broadcast by the GPS
satellites which includes ephemeris and satellite clock errors [37]. The SISRE val-
ues tell us how clock and ephemeris errors affect range measurements to the satel-
lites. This research will look at reducing SISRE because it represents the clock and
ephemeris error, which as shown in Table 1.1, is the most dominant error source
regarding the accuracy of the PPS signal [31].

This research proposes that absolute position and clock bias estimates of satel-
lites in a constellation can be improved by relating the position of each satellite to the

positions of other satellites in the geometry. The relative ranges between satellites can then be used to supplement the orbital data available to the OCS for position and clock error estimation. Currently, all GPS satellites operate nearly independently – no intersatellite information is regularly used to generate the ephemeris and clock errors [14]. Additionally, each satellite is only loosely linked to others in the constellation by virtue of the fact that the pseudoranges to each satellite have the same ground station receiver clock errors in common. In order to produce an ephemeris and clock error improvement link between satellites, which would inherently reduce the SISRE, this thesis will attempt to utilize research being done in the field of pulsar-aided spacecraft navigation.

Using pulsars to aid in SISRE reduction is ideal for three key reasons. First, they are naturally occurring; hence, they are freely available for use at any time. Second, pulsars are spaced throughout the sky in such a manner that several can be used to make simultaneous TDOA measurements between several clusters of GPS satellites. Third, because each pulsar is unique and predictable, a pulsar profile can be made and stored in each GPS satellite for recognition and future use.

1.3 Problem Definition

This effort seeks to improve GPS navigation accuracy using x-ray pulsars to reduce the GPS constellation's ephemeris and clock errors. The research seeks to use the periodic x-ray signals emitted from pulsars in a time-difference-of-arrival (TDOA) scheme to measure the relative distances between GPS satellites. The intersatellite range information obtained via TDOA measurements will augment the ground-based pseudorange measurements already used by the OCS to estimate the ephemeris and clock error values for the constellation. Improved ephemeris and clock error accuracies should yield improved navigational precision for military users of the PPS signal and civilian users of the SPS signal due in part to the inherently lower SISRE components they produce.

1.4   Objectives

The primary goal of this research is to investigate the feasibility of using x-ray signals from pulsars in a TDOA navigation scheme to reduce errors in the OCS estimates of GPS satellite position and clock bias.

The first objective involves determining the timing accuracy needed to make pulsars beneficial to the GPS orbit determination problem. The ability to make precisely timed pulsar measurements is imperative, because the timing errors, measured in units of time, are scaled by the speed of light in a vacuum (3×10^8 m/s). For example, an overall GPS timing error of 1 microsecond (1×10^{-6} s) would translate to an unacceptable GPS satellite position error of 300 m.

Next, a tradeoff study will then be conducted to determine the number of pulsars needed to justify using the x-ray detectors on GPS satellites for TDOA measurements. For example, will 1 or 2 pulsars yield desirable results, or will a feasible pulsar-aided GPS system require several pulsars.

The simulation will then be modified by eliminating all GPS ground links to study the performance and navigation accuracy of GPS using only x-ray signals from pulsars in the absence of ground based pseudoranges. Many studies have been conducted to ascertain how the performance of GPS will be affected in the event of ground station outages [14, 53]. The research will seek to answer the question of whether or not pulsar TDOA measurements could be used to sustain GPS system navigational accuracy requirements in the event that the satellites are fully denied access to the OCS generated ephemeris and clock error updates.

Finally, an analysis of variable pulsar geometry will be conducted. This simulation test will attempt to determine if pulsars located in a dispersed geometry, are any more beneficial to GPS navigation errors than a geometry where all pulsars are located in one general galactic direction.

1.5   Related Research

This section will outline research related to this thesis that has been conducted or is currently being conducted. Topics to be covered include ongoing efforts to improve GPS orbit determination/estimation, intersatellite links for a constellation of satellites, TDOA range measurement techniques, and spacecraft navigation using x-ray signal measurements from pulsars.

1.5.1   GPS Orbit Determination/Estimation Improvement Background. As previously stated, the goal of this research is to augment the accuracy of the methods used to estimate the orbital parameters of the GPS satellites. Currently the 2nd Space Operations Squadron (2SOPS) of the United States Air Force (USAF) operates and maintains the GPS constellation at the Master Control Station (MCS). Together with five other monitor stations this segment of GPS is known as the Operational Control Segment [30]. It is the responsibility of 2SOPS to monitor the health of each GPS satellite, carry out orbital maneuvers when necessary, and estimate the ephemeris and clock errors for each satellite using a Kalman filter. The nature of the 2SOPS Kalman filter will be discussed in Chapter 2 of this thesis. The MCS has implemented the results of many Kalman filter studies over the past decade which have resulted in improvements to its Kalman filter estimation techniques, including the Clock Improvement Initiative [21], Ephemeris Enhancement Endeavor [12], Accuracy Improvement Initiative [29], and the GPS OCS Performance Analysis and Reporting (GOSPAR) project [11]. Each of these improvement projects will be covered in the sections that follow.

1.5.1.1   Clock Improvement Initiative. In 1994, the MCS undertook the task of improving GPS timing accuracy and the stability of the composite clock frequency output [21]. The improvements focused on fine tuning the continuous time update process noises in the MCS Kalman filter for all GPS satellite frequency standards. Until October 1994, a constellation-wide frequency standard tuning had never been attempted [21].

To provide a stable frequency standard for the GPS satellites, one of two types of atomic clocks are employed: a Cesium (Cs) or Rubidium (Rb) clock. Each clock has its strengths and weaknesses. For example, the one-day frequency stability of a Rb clock state is significantly better than that of a Cs clock [21]. However, Cs clocks have proven to be more stable for the MCS Kalman filter than their Rb clock counterparts [21]. Furthermore, Rb clocks have a worse drift rate term than Cs clocks [21]. The poorer drift rate terms of Rb clocks forced the MCS to look at better ways to estimate Rb clock states in order to capitalize on their inherently superior frequency stability [21]. The answer to the Rb clock estimation problem lay in re-tuning the Rb clock state process noises in the Kalman filter. The endeavor proved a success. One parameter used to gauge the new estimator's accuracy lay in the User Range Accuracy (URA), which is a statistical indicator of the range accuracies a user can obtain from a particular GPS satellite [1]. Before the re-tuning, URA values were typically on the order of 5 meters. After the re-tuning effort, URA values dropped to 3.8 meters [21]. The re-tuning technique, based on a Naval Research Lab (NRL) Rb clock study, was subsequently used to improve the accuracy of all GPS Cs clocks as well.

1.5.1.2 Ephemeris Enhancement Endeavor. The Ephemeris Enhancement Endeavor (EEE), conducted in 1997, was a comprehensive effort to improve the MCS Kalman filter's ability to estimate GPS ephemeris, solar, and clock state information [12]. In 1996, a 2SOPS Performance Analysis Working Group (PAWG) identified a periodic 2–3 meter ephemeris estimation error in the MCS Kalman filter. It was determined that deterministic errors and Kalman filter tuning were the primary contributors to this periodic effect. The EEE team was formed to identify and solve the problems leading to the periodic ephemeris error effect [12]. The EEE team decided to analyze the option of re-tuning the MCS Kalman filter to decrease or eliminate the periodic error based on the successes of the clock tuning effort of 1994. Ultimately, the solution lay in calculating new values for the process noises that repre-

sent radial and along-track perturbations as well as two solar pressure terms, K1 and K2. The process noises of the Kalman filter account for the errors when propagating forward in time. The effort to reanalyze the process noise values for these phenomena and recalculate them proved to be a complete success. 2SOPS documented improvements in the periodic ephemeris error, time transfer error, daily upload prediction quality and zero age of data error. The EEE also provided the constellation's lowest ranging errors in the history of the program [12]. In part, because of EEE, the RMS SISRE value for PPS dropped from approximately 2.6 m in 1996 to approximately 2.2 m in 1997 [29].

The success of EEE was corroborated in a study conducted in 2003 which statistically compared the GPS broadcast ephemeris position error to the International GPS Service for Geodynamics final orbit solution over the entire operational lifetime of the GPS System (14 November 1993 through 31 December 2002) [37]. The comparison looked at GPS positional errors in the form of 'orbit-only SISRE' which accounts for a satellite's along-track, cross-track, and radial position but not its clock bias. During the course of the study it was found that the constellation 'orbit-only' SISRE averaged approximately 1.7 m RMS until 1997 when it dropped to approximately 1.1 m RMS [37]. The drop in SISRE value coincided with the implementation of the EEE.

1.5.1.3 Accuracy Improvement Initiative . In 1995 the National Academy of Science's National Research Council (NRC) published a congressionally mandated study of recommended technical improvements and augmentations for the GPS [31]. The recommendations of this report were formally addressed in the Accuracy Improvement Initiative (AII) [29]. The AII was a DoD- funded process sponsored by 2SOPS to look at ways to improve GPS PPS performance for DoD operations in 1997 [29]. The goal of the AII was to decrease RMS SISRE values for MCS Kalman filter states, thereby improving the broadcast navigation message accuracies. The product of the AII was a recommendation to make 3 enhancements to the OCS seg-

ment of GPS. The first suggestion was to include the National Imaging and Mapping Agency's (NIMA) six tracking stations in the global network of GPS monitor stations. The additional monitor stations would fill several global coverage gaps and more than double the amount of tracking data used in GPS operations. It was estimated that this proposal alone could improve the accuracy of the MCS Kalman filter by 50% [29]. The second recommendation of the AII advised performing a modification to the MCS Kalman filter estimation process by eliminating the estimation partition present in the filter. The partitioned filter was a remnant of the computer storage limitations faced in the 1980s, when the original OCS software was developed. The AII team proved that a 10%-15% SISRE performance improvement would be gained due to the nonpartitioned filter's ability to decorrelate parameters in the estimation process. The third proposal suggested a new strategy to upload navigation messages to GPS satellites in order to reduce prediction errors. The new strategy devised an upload schedule for all of the satellites based on their need to receive updated navigation messages. GPS satellite performance is not consistent across the constellation. Some satellites may require more frequent uploads because of the nature of their active on-board clock. The new upload schedule addressed problem-oriented satellites by allocating more uplink time to those satellites while allowing more predictable satellites to fly with older data. All scheduled software and hardware upgrades recommended in the AII report are scheduled for completion in 2005 [20]. When the AII upgrades are completed, the root mean square SISRE value for GPS is not expected to exceed 1.3 m [24].

1.5.2   Intersatellite Links Background.   Ultimately this thesis seeks to treat the system of GPS satellites as an inter-related network. Intersatellite links are advantageous to constellations because they provide additional measurements of the GPS satellite positions and clock errors for the MCS Kalman filter. Several studies have been done involving intersatellite links. The following section will outline research done at the University of Texas at Austin, the Space Applications Corporation, IBM,

the National Research Council, and the University of the Federal Armed Forces in Munich, Germany. Each organization's research attempted to improve current orbit determination techniques using intersatellite links.

1.5.2.1 University of Texas at Austin Study. In 1984, research on the orbit determination of GPS using inter-satellite (cross-link) range measurements was conducted at the University of Texas at Austin. The experiment used a batch estimation filter with ground-to-satellite (L1/L2) and satellite-to-satellite pseudo-range measurements as inputs to simulate 18 fully operational satellites. The cross-link measurements were generated in 36-second cycles allowing each GPS satellite an interval of 1.5 seconds to transmit to all of the other satellites in the constellation. When each satellite was not in transmit-mode it would default to receive-mode to listen for the signals from all other satellites. Ultimately, it was concluded at the end of this research that relative clock errors between satellites could be significantly mitigated with cross-link data [18].

1.5.2.2 Space Applications Corporation Study. In 1985, the Space Applications Corporation conducted research to determine the feasibility of designing an autonomous navigating GPS constellation. The creation of intersatellite links for range measurements and communication was integral to the GPS satellites being able to navigate in an autonomous mode [10]. Cross-linking capabilities for GPS originated in the nuclear detection (NUDET) mission designed for Block II satellites and beyond. Nuclear detection, a secondary mission for the GPS constellation, would mandate that satellites communicate with each other on a L3 link to disseminate detonation information quickly around the globe to our ground or air assets. Secondary uses for cross-links were studied by various organizations such as IBM, Aerospace Corporation, and the University of Texas [10]. It was determined that autonomous navigation is possible and reasonable; navigation accuracy could be maintained for at least 180 days. Only selected parameters of a reference ephemeris would need to be modified in the navigation message to make this a reality. The study predicted that cross-link

ranging and communication could benefit GPS by increasing accuracy of navigation services by at least a factor of two, reducing OCS operation and maintenance cost due to reduced satellite servicing requirements, and providing protection against OCS outages [10].

1.5.2.3 Synchromesh: An IBM Corporation Study. Synchromesh, a concept proposed by IBM in the 1980s, involved enhancing GPS performance by enhancing ground prediction procedures with intersatellite information exchanges to decrease clock and ephemeris errors [14]. Through the synchromesh study, IBM theorized that an increase in performance could be obtained by using a simplified prediction filter coupled with cross-linking range data to estimate and correct clock and ephemeris errors. Researchers proposed that each satellite, at a particular measurement time, could determine the relationship of its own clock with respect to other visible satellites in the constellation; each particular satellite could subsequently adjust its clock toward the best overall fit. Therefore each clock could be safely set to the calculated constellation clock best fit, which would ensure relative clock consistency within the constellation between all of the satellites. Ephemeris errors would be handled in much the same way as the clock errors described above. Intersatellite ranging measurements would be used in a least-squares estimator method to determine what adjustments each satellite would have to make in order to reduce tangential (along-track) orbital error. Ultimately it was found that the synchromesh method drove the User Range Error (URE) for GPS from 2.3 m RMS to 2.1 m RMS when only clock corrections were factored in. The baseline (nominal operations without synchromesh) GPS model was improved by a factor of almost 50 when both clock and tangential orbit corrections were applied using synchromesh. It is important to note that the proposed synchromesh method would be carried out entirely in orbit with no communication needed with the OCS. In fact, the number of uploads needed to adhere to navigation accuracy requirements during the simulation decreased from three times per day to once per two weeks, illustrating the potential power of extensively using

intersatellite communication for GPS [14]. Synchromesh was never practically implemented because the then-current GPS satellites did not posses the necessary two-way communication capability.

1.5.2.4   National Research Council Study.   In 1995 the congressionally funded NRC conducted a comprehensive study of the entire GPS system; the council recommended many improvements such as using intersatellite ranging measurements in the OCS Kalman filter. The NRC advised that the MCS could decrease the GPS system navigation error by approximately 1.2 m (1σ) by incorporating intersatellite ranging data in the filter and uploading that information to all GPS satellites every hour [31].

1.5.2.5   University of the Federal Armed Forces Munich Study.   Intersatellite link research was conducted at the University of the Federal Armed Forces Munich in Germany in 2001. Several orbital scenarios (LEO, MEO, GEO) were analyzed to determine the effects of using intersatellite links and auto-navigation-equipped satellites on the ephemeris errors of simulated constellations. The conclusions of the research were that to optimally apply intersatellite links, all satellites would have to be processed in one large filter. The results also yielded answers to the question of what would happen to the constellation if no ground links were available and the constellation relied on an 'autonav' mode via intersatellite links. In the case of GPS Block IIR satellites used in the simulation, it was found that the intersatellite links could aid in the relative positioning of the satellites. Researchers also found that the elimination of ground links yielded deleterious effects on the absolute positioning of the satellites as well as for the constellation as a whole. For example, a decoupling phenomenon was observed to occur between the constellation and the earth's rotation. Ultimately, if only satellite crosslinks were to be used, position errors (along track, cross track, radial) would increase up to 10 m within 180 days with no updates from the ground links [53].

1.5.3   Spacecraft Navigation Using Pulsars.   Using signals from pulsars to aid in spacecraft navigation is not a new idea. As early as 1974, a method of using radio signals from pulsars to navigate interplanetary spacecraft was proposed in a NASA Technical Report [15]. It was found, however, that radio wave emissions are not technically feasible to use in spacecraft navigation systems [44]. Studies have shown that a large antenna on the order of 25 m in diameter would be needed to detect the faint radio emission from pulsars [44].

In 1981, Chester and Butman first presented the concept of using x-ray pulsars for spacecraft navigation. At the time, approximately 12 x-ray pulsars had been cataloged as good candidates for spacecraft navigation because of their stability and the strength of their signal. Unlike radio source pulsars, it was conjectured that signals from x-ray source pulsars could be collected with the use of a 1000 cm^2 detector to yield three dimensional position accuracies of 150 km [9].

In 1993, Wood outlined the x-ray satellite navigation studies to be performed by the Unconventional Stellar Aspect (USA) experiment onboard the Air Force Advanced Global Research and Global Observation Satellite (ARGOS). The USA experiment was the first space-based laboratory for testing the concepts of attitude and position determination using x-ray detectors. The USA experiment, which launched in 1999, was a collimated proportional counter x-ray telescope with 1000 cm^2 of effective area. The telescope was sensitive to photons in the energy range 1 - 15 keV and was able to time tag all photon events with the help of a GPS receiver [40]. Satellite position, attitude, and timekeeping research was conducted at institutions such as Stanford University [19], the NRL [54], and the University of Maryland [43, 44] based in part from data collected with USA until the detector's demise in November 2000.

The researchers at the Space Systems Laboratory, University of Maryland, are currently utilizing data from USA experiment to refine methods of determining space-craft time, position, and velocity [43]. Four methods of position determination are being investigated, including x-ray pulsar elevation (position angle of pulsar relative

to nearby planets), Earth-limb occultation, delta position estimator, and absolute position determination. Of these four methods, the latter two are the prominent methods studied in detail thus far. The delta position estimator method uses TDOA measurements from two or more x-ray pulsars to measure the difference in relative position between the spacecraft and the solar system barycenter [43]. The absolute position determination method capitalizes on the unique pulse cycles common to all pulsars in a process similar to the GPS integer cycle ambiguity-resolution method. By tracking the phase of several pulsars, a search grid centered about a known point in space can be created of candidate spacecraft locations that match the measured phase cycles [43]. The specific candidate location that best matches the measured pulsar signal over time is selected as the spacecraft's absolute position.

The Defense Advanced Research Project Agency (DARPA) is currently sponsoring research in the field of autonomous navigation for DoD spacecraft. Conceptually, this research is very similar to the University of Maryland research described above. The X-ray Navigation for Autonomous Position Verification (XNAV) hopes to provide the DoD with autonomous navigation capability independent of GPS using pulsars as pseudo lighthouses and x-ray clocks [35]. The mission of the XNAV program is to provide military space assets with a complimentary/backup navigational payload that could be used in the event that potential space threats (e.g., nuclear detonation) disabled satellite communications or impaired GPS usage. XNAV is a milestone based three phase program. The three phases will address three key technology issues in order to accomplish the aforementioned mission [35]:

- Detect Pulsar Sources in the energy range of 0.1 to 20 keV

  1. First, candidate pulsars must be located to angular resolutions < 0.0001 arcsec.

  2. Next, pulsar sources with fluxes $> 10^{-5}$ photons/cm^2/sec must be characterized and modeled.

3. Finally, pulsars will be observed for time durations between 10^3 to 10^6 seconds.

- Develop x-ray detectors with high signal to noise capabilities

  1. Detector area < 1 m^2.

  2. Timing resolution from 1 to 10 nanoseconds.

  3. Electronic response times of < 1 nanosecond.

- Develop a sensor package with expected time and position determination accuracies of less than 10 m CEP (3 σ)

1.5.4 Time Difference of Arrival Based Navigation.   The TDOA measurements of x-ray signals from pulsars are integral to the research of this thesis to improve the accuracy of the GPS orbit estimation process. TDOA measurements will be used to estimate relative ranges and clock errors between satellites. The proposed pulsar-based TDOA navigation system is not the first TDOA-based navigation system in history. TDOA based systems range in application from search and rescue systems [55] to GPS radio interference locators [45]. This section will discuss two other examples of TDOA systems: Long Range Navigation (Loran) System [30], and a study done at the Air Force Institute of Technology which proposed a television-based TDOA system [16].

1.5.4.1 Loran.   Loran is a radionavigation system conceived and constructed during World War II. Loran, developed at the Radiation Laboratory of the Massachusetts Institute of Technology, was designed primarily for ship navigation. Loran is composed of a chain of synchronized transmitters which radiate pulses of RF energy. A receiver measures the time difference of arrival between pulses from the master and secondary transmitter stations. Each measured time difference aides in fixing the location of the receiver on a hyperbolic line of position. When the time difference of at least two pairs of transmitters are recorded, the receiver can fix its longitude and latitude on the earth because the receiver uses the intersection of two

hyperbolic lines of position will define a 2-D position [26, 30]. A variant of the original Loran called Loran-C is still in use today. Located in the northern hemisphere, Loran-C provides 2-D RMS positioning accuracy of approximately 250 m [30].

1.5.4.2 Television Signal Based Navigation. In 2003, research was conducted at (AFIT) to investigate the use of existing analog television signals for navigation. The concept of TDOA-based range measurements was fundamental to this proposed navigation system. The experiment involved using a single transmitter with two receivers to estimate the range between one of the receivers and the transmitter. These ranges, which factored in clock errors (also known as "pseudoranges"), were then processed in a multilateration algorithm to determine position and clock errors for the target receiver. It was discovered that using 8 simulated National Television System Committee (NTSC) broadcast signals around Dayton, OH in a TDOA algorithm, 40 m position accuracy could be attained . This study is an example of using "signals of opportunity" (like Pulsars) for navigation [16].

1.6 Thesis Overview

Chapter 1 introduced the concept of GPS navigational accuracy and how this research will endeavor to improve it through a TDOA navigation scheme. A summary of research related to improving GPS navigational accuracy, TDOA navigation, and pulsar-based spacecraft navigation was then presented.

Chapter 2 describes the background theory used in this research to develop the GPS simulation. First, an overview of the different GPS segments will be given. Next, an analysis of the current OCS Kalman filter will be conducted followed by an analysis description of a batch filter – which was chosen over the Kalman filter to be used in the simulation supporting this research. A development of the ground based pseudorange, pulsar based x-ray signal Time of Arrival (TOA), and TDOA measurement will be presented. The theory of clock modeling and the integral role clocks play in the GPS system will be outlined. Next, five reference coordinate systems important for GPS

will be studied. Finally, navigational errors fundamental to GPS, to include SISRE, will be defined and their utility for interpreting simulation results will be explained.

Chapter 3 will discuss how the simulation was created and implemented to yield research results. Chapter 3 will discuss how the GPS constellation was modeled using Fortran® 90 and Matlab® Releases 13 and 14. The methodology of incorporating pseudoranges and various pulsar TDOA range measurement scenarios into the batch filter will also be addressed.

Chapter 4 will analyze the effect of incorporating pulsar TDOA measurements on current operational SISRE values for GPS. The results of using different noise values for a varying number of pulsars to calculate SISRE will also be evaluated. Finally, Chapter 5 will make overall system conclusions and recommendations for future research.

II. Background

This chapter presents the background topics fundamental to this research. First a brief overview of the GPS segments will be given. The current GPS orbit determination methods using the Kalman filter will then be described. Subsequently, a method of orbit determination using a batch least squares estimator will be outlined. The concept of estimating and modeling GPS clocks and their corresponding errors will then be developed. Next, the equations describing pseudorange measurements and x-ray signal TOA measurements from pulsars will be introduced. The theory of TDOA measurements will be described. The five reference coordinate systems essential to the GPS simulation will then be outlined and explained. Finally, the GPS navigational measurements of error will be addressed both conceptually through figures and mathematically through the corresponding equations.

2.1 GPS Overview

GPS was developed by the Department of Defense (DoD) to offer the U.S. military and other selected users accurate estimates of position, velocity, and time. U.S. military requirements stipulated that position, velocity, and time errors be kept below 10 m, 0.1 m/s, 100 ns (nanoseconds) respectively in a RMS sense [30]. The three separate GPS segments, working in concert in order to accomplish the mission of GPS and achieve its quantitative position, velocity, and, time goals are the OCS, the space segment, and user segment. Figure 2.1 depicts all three GPS segments.

2.1.1 Operational Control Segment. The OCS itself can be partitioned into three sub-elements: the Master Control Station (MCS), monitor stations, and ground antennas. Figure 2.2 portrays the global locations of each element. The MCS, which provides command and control for the entire GPS system, is the heart of the OCS. Located at Schriever Air Force Base near Colorado Springs, Colorado, the specific functions of the MCS include tracking satellite orbits, monitoring and sustaining satellite health, maintaining GPS time, predicting satellite ephemerides and clock parameters, updating the satellite navigation messages, commanding the small maneuvers of

THE MAJOR SEGMENTS OF THE GPS SYSTEM

PLANNED CONSTELLATION:
6 PLANES
3 SATELLITES EACH PLANE
55° INCLINATION

SPACE SEGMENT

RF SIGNAL LEVELS
(MINIMUM VALUES RECEIVED)

FREQUENCY	PRN SIGNALS (FOR C/NO. ≥ 29 dB)	
	C/A NORMAL MODE (dBW)	P (dBW)
L₁	-160	-163
L₂	-166 OR -166	

DOWNLINK DATA
· CODED RANGING SIGNALS
· POSITION INFORMATION
· ATMOSPHERIC DATA
· ALMANAC

UPLINK DATA
· SATELLITE EPHEMERIS (POSITION) CONSTANTS
· CLOCK-CORRECTION FACTORS
· ATMOSPHERIC DATA
· ALMANAC

TRANSMISSION BANDS

DATA LINK	FREQUENCY (MHz)
L₁ (DOWNLINK)	1575.42
L₂ (DOWNLINK)	1227.6
S-BAND (DOWNLINK)	2227.5
S-BAND (UPLINK)	1783.74

USER SEGMENT

MONITOR STATIONS

GROUND ANTENNA

MASTER CONTROL STATION

CONTROL SEGMENT

Figure 2.1:   The GPS has three major segments: OCS, space, and user [26]

satellites in order to maintain the orbits, and relocating satellites to compensate for failures when necessary [30]. The monitor stations, which are unmanned and remotely operated by the MCS, continuously track GPS satellite signals. The equipment at the monitor stations essentially consists of GPS receivers with cesium atomic clocks, meteorological instruments, and communications gear to transmit the measurements to the MCS via ground and satellite links [30]. As mentioned in Chapter 1, the implementation of the AII will introduce 6 new NIMA operated monitor stations to the OCS network to increase the amount of tracking data available [20]. Finally, the ground antennas, which are co-located with several monitor stations, are used for communications with the GPS satellites via S-band radio links. The antennas are also operated remotely by the MCS. Communications to the satellites consist of telemetry from the satellites on the status of subsystems and functions, uplink commands, and navigation messages generated by the MCS to be uploaded to the satellites for global broadcast [30].
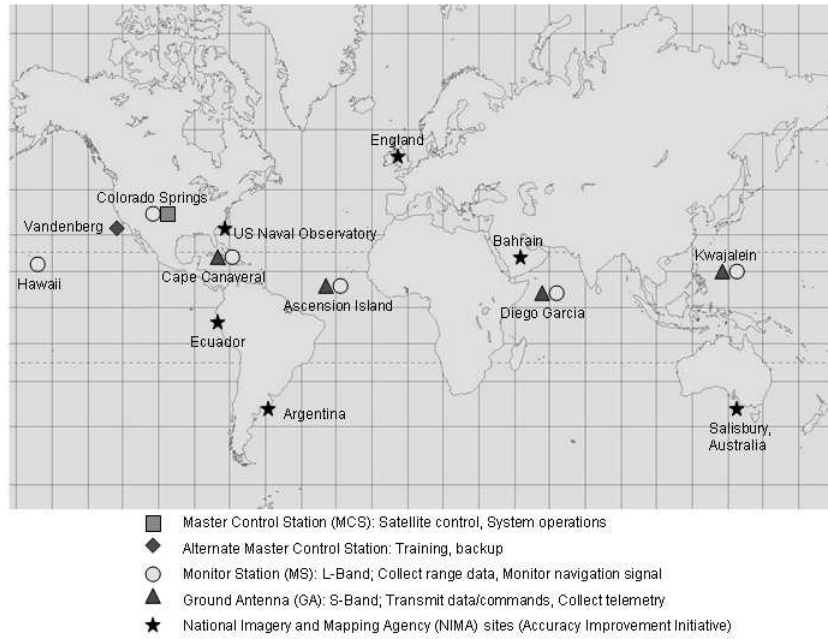
Figure 2.2:   Map of GPS monitor stations. The Accuracy Improvement Initiative (AII) proposes to amplify the tracking power of the OCS by adding 6 NIMA monitor stations

2.1.2 Space Segment.   The baseline GPS constellation consists of 24 satellites. The approximate orbital characteristics are listed below [30]:

- Semi-Major axis: 26,560 km

- Altitude: 20,200 km

- Eccentricity: < 0.01

- Period: ≈ 12 hours, mean sidereal time

- Six orbital planes all with inclinations of 55 degrees. The orbital planes are labeled A through F

- The right ascensions of ascending node for each orbital plane are separated by 60 degrees relative to the equatorial plane

- Four satellites per plane with room for a spare satellite in a fifth slot in each plane

Figure 2.3:   The GPS satellite constellation [32]

Figure 2.3 depicts the GPS constellation and the equally spaced orbital planes. The initial prototype satellites, called Block I satellites, were launched between 1978 and 1985. The production model satellites, called Block II and IIA, were subsequently launched to create the operational GPS constellation. Beginning in 1997, the next generation GPS satellites, called Block IIR satellites were launched to sustain and upgrade the capabilities of the constellation [30]. The current GPS constellation consists of a mix of Block II, IIA, and IIR satellites [2].

2.1.2.1 *Satellite Ephemeris.*   An ephemeris can be defined as a complied set of state vectors for a given satellite predicted over time [50]. The ephemeris values are computed when the OCS uses a Kalman filter to propagate the GPS satellites' positions and velocities to future instances in time. A constellation's combined ephemeris values are referred to as ephemerides. The ephemerides describe the GPS

Figure 2.4:   Diagram of Keplerian (classical orbital) elements
used to describe GPS satellite orbits [30]

orbits in terms of Keplerian orbital elements. Figure 2.4 depicts the Keplerian or-
bital elements, commonly referred to as the classical orbital elements, which form
the foundation of the GPS ephemeris parameters. There are additional terms in the
ephemeris to account for orbit perturbations using time dependent orbital element
terms and sinusoidal geoid correction terms. The ephemeris parameters broadcast
by a GPS satellite are described fully in the ICD-GPS-200c [1]. The ICD also pro-
vides instructions on how to compute satellite positions and velocities in the ECEF
coordinate frame [30].

2.1.2.2   Navigation Message.   Perhaps the most important function of
the space segment is the broadcast of the navigation message to the global users of
GPS. The satellites transmit precisely timed GPS signals primarily on two L-Band
frequencies: 1.57542 GHz and 1.2276 GHz [33]. The purpose of the navigation mes-
sage is to provide users with satellite positions and satellite clock corrections for use
in the user's navigation (position, velocity, time) solution. The message, unique to
each satellite, is modulated on a pseudo-random noise (PRN) signal. Among the in-
formation encoded in the broadcast message are the current orbital parameters of the
satellites predicted by the MCS. Table 2.1 lists the ephemeris parameters broadcast

Table 2.1:   Elements of the ephemeris in the GPS Navigation
              Message [30]

Parameter	Description
t_{0e}	ephemeris reference time
$\sqrt{a}$	square root of semi-major axis
e	eccentricity
i_0	inclination angle at reference time
Ω_0	longitude of the ascending node at the beginning of the GPS week
ω	argument of perigee
M_0	mean anomaly at the reference time
Δn	correction to the computed mean motion
$\dot{i}$	rate of change of inclination with time
$\dot{\Omega}$	rate of change of right ascension of ascending node with time
C_{uc}, C_{us}	amplitudes of harmonic correction terms for the computed argument of latitude
C_{rc}, C_{rs}	amplitudes of harmonic correction terms for the computed orbit radius
C_{ic}, C_{is}	amplitudes of harmonic correction terms for the computed inclination angle

in the navigation message. Detailed information about the GPS satellite message can be found in [33].

2.1.3   User Segment.   The early years of GPS saw a user community primarily populated by military users. Investments made in GPS receiver technology by the government and private technology companies, however, has spawned a recent explosion in civilian GPS usage. The expansion of civilian use can primarily be attributed to the creation of more portable and affordable receivers. A typical GPS receiver is composed of [33]:

- Omnidirectional antenna - to receive the encoded navigation message broadcast from GPS satellites on the L1 and L2 bands

- Filter/Amplifier - to filter out interfering signals and amplify the GPS signal

- Delay Lock Loop Receiver/Demodulator - to provide estimates of the pseudor-ange, carrier phase, and navigation data for each satellite

- Navigation Data Processor - to calculate the position of each satellite based on the navigation data

- Kalman Filter - to estimate the user position and velocity state vector

- Reference Oscillator - to provide time and frequency reference for the receiver

The typical GPS receiver is also able to make corrections for ionospheric delays and electromagnetic disturbances by simultaneously receiving GPS signals on both the L1 and L2 bands. A detailed description of a typical GPS receiver architecture can be found in [33].

2.2   Current GPS Kalman Filtering Techniques

A partitioned Kalman filter is at the heart of the GPS orbit estimation process conducted by the MCS at Shriever AFB, CO [31]. The Kalman filter is ideal for this task for many reasons. The Kalman filter has proven itself to be useful for situations in which data is available in a continuous stream. In fact, the Kalman filter is also known as a sequential filter because it continuously improves the estimate of the state vectors by sequentially incorporating new data measurements into the estimate as they become available [52]. In other words, the Kalman filter utilizes data from the past up to the present to achieve a current state estimate [34]. Additionally, Kalman filters are able to compensate in situations where forces in a dynamical system are not completely known or have been incompletely modeled [50]. Kalman filters are ideal for handling stochastic systems. The Kalman filter begins with an estimate of the state (e.g., position and velocity) $\hat{X}_t$ and the state's estimated covariance $\hat{P}_t$ at time t. The covariance matrix is a statistical measure of how good our estimate, $\hat{X}_t$, is. Next, an a priori solution of the state $\tilde{X}_{t+1}$ and covariance $\tilde{P}_{t+1}$ is generated for the next epoch. These new epoch predictions are computed with no new real data –

they are simply calculated predictions. This step is sometimes referred to as the time propagation. The predicted state is found by:

$$\tilde{X}_{t+1} = \Phi_{t+1,t}\hat{X}_t \qquad (2.1)$$

where

$\tilde{X}_{t+1}$ is the current state vector

$\Phi_{t+1,t}$ is the state transition matrix. The state transition matrix is used to propagate the state estimate and its covariance through time

$\tilde{X}_{t+1}$ is the state vector propagated to the next epoch time prior to incorporating new measurements

The covariance is correspondingly propagated by:

$$\tilde{P}_{t+1} = \Phi_{t+1,t}(\hat{P}_t)\Phi_{t+1,t}^T + Q_t \qquad (2.2)$$

where

$\tilde{P}_{t+1}$ is the covariance propagated to the next epoch time using no new real data

Q_t is the second moment of the process noise. Q_t is a covariance matrix associated with the process noise error that occurs when the covariance matrix is P_t is propagated through time [50]. Essentially Q_t accounts for the uncertainty in the Φ matrix's ability to model the dynamics inherent in the GPS prediction problem [50]

$\tilde{X}_{t+1}$ is the state vector propagated to the next epoch time with no new real data

When new data[1] from the monitor stations is sequentially added to the estimator, new estimates of the state vector $\hat{X}_t$ and covariance matrix $\hat{P}_t$ are generated as a result. The estimated state and covariance can be thought of as corrected versions of the predicted values, $\tilde{X}_{t+1}$ and $\tilde{P}_{t+1}$ respectively. This step is sometimes referred to as the measurement update [34]. The state is updated by:

---

[1]In this research, data used in a filter will also be referred to as a measurement and/or observation (e.g. TDOA measurement, pseudorange observation).

$$\hat{X}_{t+1} = \tilde{X}_{t+1} + K_{t+1}(\vec{z}_{t+1} - H_{t+1}\tilde{X}_{t+1}) \qquad (2.3)$$

where

$(\vec{z}_{t+1} - H_{t+1}\tilde{X}_{t+1})$ represents the residual vector $(\vec{r})$

$\vec{z}$ represents the new real data vector

K is the Kalman gain matrix

The K matrix weights the predicted residual vector and can be computed from:

$$K_{t+1} = \tilde{P}_{t+1}H_{t+1}^T(H_{t+1}\tilde{P}_{t+1}H_{t+1}^T + R_t)^{-1} \qquad (2.4)$$

where

R is the measurement noise covariance matrix

H is the observation partial derivative matrix. H relates the linearized observations (z) to the estimated states in the X matrices

The updated covariance matrix is calculated by the equation:

$$\hat{P}_{t+1} = \tilde{P}_{t+1} - K_{t+1}H_{t+1}\tilde{P}_{t+1} \qquad (2.5)$$

The MCS at 2SOPS implements an extended[2] Kalman filter for its deterministic and stochastic modeling advantages. In the deterministic domain, the task of continuously predicting satellite states for hours, days, or weeks into the future is essential to GPS user navigational operations [52]. The Kalman filter allows the MCS to exploit a proper dynamics model through the state transition matrix Φ to continuously predict satellite states and covariances.

Clock errors, radial / along-track / cross-track orbit perturbations, and solar radiation perturbations characterize the stochastic aspect of accurately predicting GPS states. These quantities are stochastic because of their random nature. Statistical

---

[2]See [50] for the definition of an extended Kalman filter and its applications

losses of information caused by process noise uncertainty and the passage of time can be accounted for by the Kalman filter through a method called "tuning." The tuning strategy involves experimentally changing the Q_t term in the propagation covariance Equation (2.2). The tuning process has been applied several times (EEE and Clock Improvement Initiative) by the MCS as was mentioned in Chapter 1.

Finally, the Kalman filter serves the MCS well because of its computationally amenable nature. The Kalman filter characteristically processes data sequentially in relatively small time steps, making it easier for computers to make calculations; computational resources are conserved because they are not forced to deal with all the data for a given interval at once. Additionally, because of technological limitations present during the design phase, the MCS Kalman filter was partitioned to process subsets of GPS satellites and states separately. The partitioned computations are subsequently combined just before the estimates of the state vectors at epoch are found. With the implementation of the AII outlined in Section 1.5.1.3, the MCS Kalman filter will be recombined into a single partition. It has been conjectured that the single partitioned Kalman filter will result in satellite ephemeris and clock errors that are 15% below its partitioned predecessor [31].

2.3   Nonlinear Least Squares (Batch) Filter

A Kalman filter may not be necessary in conditions where the states are not continuously being estimated. If all measurements for a given time interval are available before the estimation process begins, then the states can be processed as one group in another type of filter - the batch filter [52]. The batch filter differs from the Kalman filter in several significant ways. Unlike a Kalman filter which continuously updates the state (and thus epoch time) after each successive observation time, the batch filter updates the state estimate after all measurements are available. Also, the Kalman filter carries all the information concerning past measurements by using past estimates as inputs into the current state and covariance estimates. The objective of a batch filter is to find a trajectory among all possible trajectories that will mini-

mize the mean square difference between the actual observations and the theoretical observations derived from the calculated trajectory [50]. The process of minimizing the sum of the squares of the observation residuals (actual - theoretical) is called the method of least squares.

Obtaining an estimate of the true trajectory by computing linear corrections to a reference (nominal) trajectory is necessary because of the nonlinear nature of the orbit determination problem. The process of solving for a satellite's states, which are embedded in an unobtainable true trajectory, involves using a nonlinear least squares technique to turn the reference trajectory into an estimate that is suitably close to the true trajectory [50]. The nonlinear least squares technique, used to iteratively estimate corrections to the initial reference trajectory [50], starts with an initial state vector X. The state vector is integrated to the first observation time using the equations:

$$\dot{X}(t) = \vec{F}(X, t) \tag{2.6}$$

$$\dot{\Phi}(t_i, t_0) = A(t)\Phi(t_i, t_0) \tag{2.7}$$

where

X is the initial state vector
$\vec{F}(X, t)$ represents the nonlinear equations of motion
$\dot{X}(t)$ is the time derivative of the initial state vector
$\Phi(t_i, t_0)$ is the state transition matrix
$\dot{\Phi}(t_i, t_0)$ is the time derivative of the state transition matrix
$A(t)$ is the matrix of partial derivatives of the equations of motion with respect to the elements of the state vector

Equation (2.7) represents the linearization of Equation (2.6). Equation (2.6) is integrated to the first observation time and can now be called the reference trajectory x_{ref}. At each observation time the residual vector is calculated from the equation:

$$\vec{r}_i = z_i - G(x_{ref}(t_i), t_i) \tag{2.8}$$

2-11

where

$\vec{r_i}$ is the measurement residual vector

z_i is the observation vector

$G(x_{ref}(t_i), t_i)$ is the calculated value of the reference trajectory. The G function describes the measured data in terms of the states of the reference trajectory x_{ref} [52]

i is the index, from 1 to N, of the number of observations in the batch corresponding to each row of $\vec{r}$

Next, the observation matrix H is calculated

$$H_i = \frac{\partial G(x_{ref}(t_i), t_i)}{\partial X} \tag{2.9}$$

where

H is the observation matrix which contains the partials of the observations with respect to the state vector components

i is the index, from 1 to N, of the number of observations in the batch corresponding to each row of the H matrix

The observations are mapped to the epoch state by multiplying each row (H_i = observation) of the H matrix by the corresponding $\Phi(t_i, t_0)$ matrix

$$T_i = H_i \Phi(t_i, t_0) \tag{2.10}$$

The successive observations (T_i) are subsequently added as rows to the final T matrix. When all of the data has been processed into the T matrix, the covariance $P_{\delta x}$ and the correction to the reference trajectory state vector is computed.

$$\delta x(t_0) = (T^T W T)^{-1}(T^T W \vec{r}) \tag{2.11}$$

$$\delta x(t_0) = P_{\delta x}(T^T W \vec{r}) \tag{2.12}$$

where

W is the measurement weighting matrix which weights the different types of

observations using the inverses of the squared standard deviations [50]

$P_{\delta x}$ is the state vector covariance matrix equal to $(T^T W T_i)^{-1}$

$\delta x(t_0)$ is the correction to the precomputed reference trajectory

Finally Equation (2.11) is used to turn the reference trajectory into an estimate of the true trajectory

$$\bar{x}(t_0) = x_{ref}(t_0) + \delta x(t_0) \qquad (2.13)$$

where $\bar{x}(t_0)$ is the estimate of the state vector.

As noted earlier, nonlinear least squares is an iterative technique. Typically, before $\bar{x}(t_0)$ can be arrived at, the sum of $x_{ref}(t_0) + \delta x(t_0)$ is equal to $x_{ref+1}(t_0)$ and the entire process begins again with $x_{ref+1}(t_0)$ being declared as the new $x_{ref}(t_0)$ [52]. The convergence of Equation (2.13) is determined by analyzing the RMS of the residuals (often referred to as the 'cost function') calculated in Equation (2.8). The goal of the nonlinear least squares technique is to minimize the sum of the residuals squared and therefore the least squares algorithm must be iterated through until the cost function stops changing within a specified tolerance [50].

2.4   Pseudorange Measurements

2.4.1   Pseudorange Calculation.   The primary observations used in this simulation to determine the position of GPS satellites will be pseudoranges. Conceptually, we follow the description in [30] and [50] to describe the generation of an operational GPS pseudorange measurement. As was mentioned in Section 2.1, each satellite generates a navigation message on two L-band frequencies, L1 (1575.42 MHz) and L2 (1227.60 MHz). Two PRN-codes, the Coarse-Acquisition (C/A) code and the Precision (P(Y)) code, are modulated onto the L1 and the L1 and L2 bands respectively [50]. The PRN-codes are unique to each satellite. To determine a PRN signal transit time, the user/receiver first compares an internal copy of the PRN signal with the one received from the GPS satellite [18]. A user can determine the pseudorange

between the receiver and the GPS satellite by calculating the time shift required to align the internal PRN signal with the observed signal from the satellite; a pseudo-range is obtained by multiplying this phase time shift by the speed of light. The measurement, called a "pseudo-range", is derived from a time difference between the satellite and the receiver and thus it includes the effects of clock errors [18]. Therefore, pseudoranges can be described as the measure of the PRN signal travel time between the GPS satellite at some transmit time, T_{trans}, and the receiver at some receive time, T_{rec} [50]. The transit time is scaled by the speed of light and represented as a distance. The pseudorange equation can then be represented as:

$$\hat{\rho} = c(T_{trans} - T_{rec}) \tag{2.14}$$

where

c is the speed of light

T_{trans} is the perceived time of transmission of the PRN-code from the GPS satellite

T_{rec} is the perceived time of reception of the PRN-code by the receiver

The time difference, derived from the transmitter and receiver clock biases, make it impossible to determine the true range between the two points with just one measurement [50]. Accounting for the clock biases, the transmit and receive times are defined as

$$T_{trans} = t_{trans} + \delta t_{trans} \tag{2.15}$$

$$T_{rec} = t_{rec} + \delta t_{rec} \tag{2.16}$$

where

t_{trans} is the true transmission time

t_{rec} is the true reception time

δt_{trans} is the GPS satellite clock error

δt_{rec} is the receiver clock error

The clock error terms δt_{trans} and δt_{rec} will be explained in greater detail in Chapter 3. The expanded pseudorange equation $\hat{\rho}$ can then be expressed as:

$$\hat{\rho} = \rho + c(\delta t_{trans} - \delta t_{rec}) \tag{2.17}$$

$$\rho = \sqrt{(x_{trans} - x_{rec})^2 + (y_{trans} - y_{rec})^2 + (z_{trans} - z_{rec})^2} \tag{2.18}$$

where

ρ represents the geometric distance between the satellite and the receiver. It is merely the product of the speed of light, c, and the difference in the PRN-code's true time of transmission and true time of reception

$x_{trans}, y_{trans}, z_{trans}$ is the position of the transmitter

$x_{rec}, y_{rec}, z_{rec}$ is the position of the receiver

Equation (2.17) physically makes sense, because if the satellite and receiver were synchronized (i.e., $\delta t_{trans} - \delta t_{rec} = 0$), the pseudorange equation would reduce to the geometric range between transmitter and receiver.

2.4.2 Estimating Positions.   Equation (2.17), when other miscellaneous measurement noises are added, can be used by the GPS system to find the position of the user or the position of the GPS satellites. When determining the position of the user, x_{trans}, y_{trans}, z_{trans}, and δt_{trans} are assumed to be known and Equation (2.17) will be used to solve for x_{rec}, y_{rec}, z_{rec}, and δt_{rec}. Mathematically, a minimum of four satellites are needed to solve for the four unknowns. Figure 2.5 depicts this pseudorange solution situation. In practice a receiver can track anywhere from 6 – 12 satellites simultaneously, which means that the nonlinear least-squares methods used to solve for the receiver position must be implemented in an overdetermined sense [30].
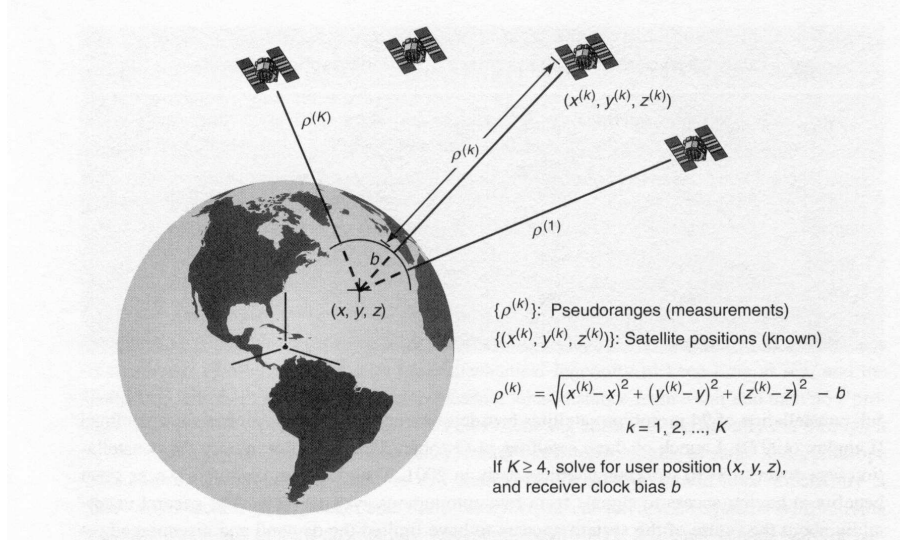
Figure 2.5:   Pseudorange measurements are needed from at least four satellites to estimate the user position $(x,\ y,\ z)$ and the receiver clock bias (δt_{rec}). In this figure b = c $(\delta t_{trans} - \delta t_{rec})$ [30].

Conversely, to determine the position and clock error $(x_{trans},\ y_{trans},\ z_{trans},\ \delta t_{trans})$ of a GPS satellite, the pseudorange solution must be inverted. Now $x_{rec},\ y_{rec},\ z_{rec}$, and δt_{rec} represent the position of a single GPS monitor tracking station. A minimum of four monitor stations containing GPS receivers are needed for the solution; in reality, hundreds of extra pseudoranges are obtained and used in an overdetermined nonlinear least-squares algorithm to determine satellite ephemeris values [26].

Operationally, when the components of Equation (2.17) are solved for, nonlinear techniques are normally used because of the nonlinear nature of the pseudorange equation. In order to use these techniques, the pseudorange equation must be linearized using a first order Taylor's series expansion. The nonlinear form of Equation (2.17) will be developed in Chapter 3. Additionally, in a situation where there are more equations than unknowns, it is advantageous to utilize all of the equations to solve for the unknowns in a least squares method. Sections 2.2 and 2.3, which outline Kalman and Batch filter techniques, are two prominent methods used to estimate unknowns in an overdetermined situation.

2.5   Pulsar Signal Time of Arrival Measurements

Pulsar TDOAs will be used to measure relative distances between GPS satellites. To obtain a TDOA, each satellite must be able to accurately measure and time-tag pulses from a corresponding pulsar. In the real-world implementation, a GPS satellite might have a pulsar template profile stored for each pulsar (much like GPS receivers have a PRN-code template for each GPS satellite – see Section 2.4). The incoming pulses for a particular pulsar would be cross correlated with its corresponding stored profile allowing a certain point on the observed pulse to then be time-tagged as the TOA. This same procedure would be conducted on another GPS satellite observing the same pulsar. The two satellites would difference their time-stamps for the same point on the pulse to determine the TDOA. This section seeks to develop the concepts and equations necessary to justify TOA measurement accuracies and noise values that will be used in the GPS TDOA simulation.

2.5.1   Pulsar Timing Profiles.   To effectively utilize the clock-like properties of a pulsar in a TOA measurement, a standard pulse template – conventionally called a pulse profile, must first be generated. A pulse profile is a representation of the integrated signal of multiple detected pulses from the pulsar. Every pulsar has a unique signal – a fingerprint, that distinguishes it from all other pulsars at that particular observing frequency with respect to its amplitude, duration, number of peaks, and stability [28] . A pulse profile is made by observing a pulsar over periods of time that range from hundreds of seconds to days. These time periods allow the detector to collect groups of individual pulses. While individual pulses can fluctuate in both intensity and shape, a profile integrated over several hundred or thousand pulses produces a standard profile shape that is reproducible for a given pulsar at a given frequency [47]. Figure 2.6 shows several pulses which are integrated to form the pulse profile [47]. Multiple pulse periods are averaged (typically called "folding") to
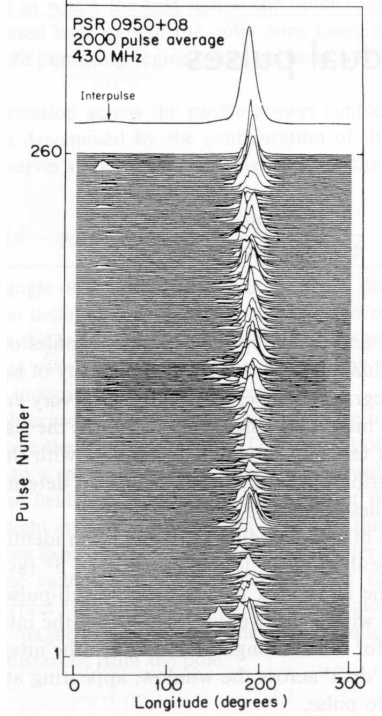
Figure 2.6: A sequence of pulses from PSR B0950 + 08 with the integrated profile obtained by adding together the sequence of individual pulses. Diagram illustrates pulse-to-pulse variability in shape and intensity. [28]

create a very high signal-to-noise ratio profile [28]. Figure 2.7 shows a profile of PSR J1811-1925[3].

2.5.2 Measuring TOAs.   A standard pulsar template recorded for each pulsar allows TOA measurements to be collected from each pulsar. Conceptually, a pulse TOA can be defined as the time at which a predetermined reference point of a pulse profile has arrived at the detector [22]. In order to measure a TOA, first a clock must record the instant that the first x-ray photons are received by the detector [46]. Typically, the observation's start time is projected forward to the midpoint of the

---

[3]The name of a pulsar is derived from its celestial coordinates. The number in front of the '+' or '-' is the right ascension in hours and minutes, and the number behind it is the declination in degrees. The letter 'B' or 'J' describes the coordinate system B1950.0 or J2000.0 respectively. For example, PSR J1811-1925 mentioned above is referenced in the J2000.0 coordinate system. The pulsar is located at a right ascension of $18^h\ 11^m$ and a declination of $-19°25'$ [28]
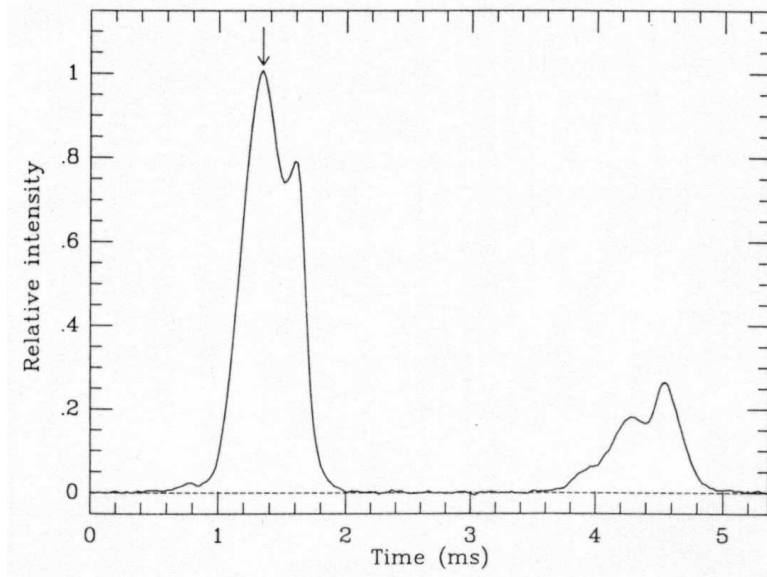
Figure 2.7:   Standard profile of PSR 1855 + 09 used to obtain
pulse times of arrival. The phase defined as the
TOA is marked with an arrow. [49]

integration time (by adding an integer number of pulse periods) to account for poorly
known pulse periods [47] and intrinsic pulsar timing irregularities. The time to a
"fiducial point"(usually the peak) in the pulse is then calculated. Finally, the time
offset between the observed profile and the standard pulsar profile is calculated. The
time offset can be calculated by determining the phase shift between the two profiles
in the Fourier domain. The TOA measurement can then be calculated as

$$TOA = t_{start} + \Delta t_{midpoint} + \Delta t_{fiducialpoint} + \Delta t_{offset} \qquad (2.19)$$

where

t_{start} is the beginning of the x-ray photon collection/integration time

$\Delta t_{midpoint}$ is the time differential between the integration start time and the
projected integration midpoint

$\Delta t_{fiducialpoint}$ is the time differential between the designated beginning of a pe-
riod and a reference (fiducial) point in the period. Often the fiducial point is a peak
in the pulsar pulse

Δt_{offset} is the time difference between fiducial points in the observation and

standard profiles

The TOAs calculated at a pair of satellites from a given pulsar pulse will yield a TDOA measurement for use in the orbit determination filter. The nature of how TDOAs are calculated will be discussed in a following section.

2.5.3 Millisecond Pulsars.   To collect TOAs for subsequent use in calculating TDOAs for the GPS constellation, it is desirable to use the most stable pulsars available. One such group of pulsars are called millisecond pulsars (MSPs). MSPs are classified as the group of pulsars with spin periods between 1.5 ms and 30 ms and spin rate slowdowns of less than 10^{-19} s/s [27]. MSPs, also called "recycled" pulsars, are extremely old pulsars (1 - 14 Gyr[4]) whose spin rates have been rejuvenated from the accretion of mass and angular momentum from a companion star [3]. MSPs are a special breed of pulsars that are especially desirable in pulsar-based spacecraft navigation (see [44]), because these pulsars display extraordinarily stable and predictable rotation rates. Figure 2.8 illustrates the comparative stabilities of MSP as compared to other time keeping devices. Short predictable pulses can mean unusually high measurement precision [49] and therefore can yield highly accurate TOA measurements. This simulation will rely on MSPs to create TDOA measurements because of their aforementioned desirable attributes.

2.5.4 Accuracy of TOA measurements.   The fundamental goal of pulsar pulse timing is to measure the location of the pulse peak as accurately as possible. The pulse peak measurement is constructed through the act of detecting photon events in a detector. The phenomena of measuring photons arriving from a x-ray pulsar source to a x-ray detector represents a Poisson statistical process because photon events are assumed to occur independently and over a constant area [38]. Therefore, the accuracy of a TOA can be approximated by the uncertainty equation [38]:

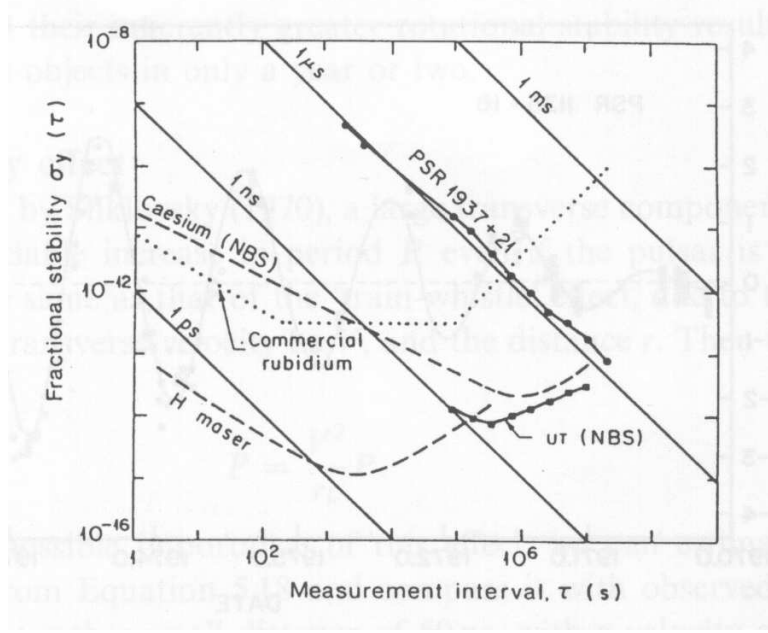---

[4]1 Galactic Year = 10^9 years

Figure 2.8:   Allan variance plot depicting the fractional stabilities of PSR 1937 + 21 as compared to atomic clocks. Fig. ref. [28]

$$\sigma_{TOA} \approx \frac{HWHM^*}{S/\sqrt{S+B}} \qquad (2.20)$$

$$HWHM^* = \sqrt{HWHM^2 + \sigma_\gamma^2} \qquad (2.21)$$

where

$HWHM$ is the measured half-width at half maximum of the pulsar pulse shape

$HWHM^*$ is the half-width at half maximum of the pulsar pulse shape summed in quadrature with the photon timing error

S is the number of photons detected from the pulsed signal of the pulsar during the observation

B is the total number of all other photon events in the observation including any unpulsed emission from the source, the diffuse x-ray background, and particle-induced background counts in the detector

σ_γ is the timing error of any individual photon. The ability of a detector to distinguish one pulse from another in units of time

Astronomers use the half-width half-maximum ($HWHM$) value to measure the wavelength dependent emission properties of pulsars near the emission maximum for each pulse [17]. Operationally, the $HWHM$ is measured by simply taking the difference in phase between the peak maximum and the points where the flux drops to one-half of the maximum value [17]. Each pulsar has been observed to have its own unique $HWHM$ measurement. It is important to note that in order to achieve a more accurate TOA measurement, σ_{TOA} must be made as small as possible. Thus, the numerator of Equation (2.20) must be driven down with respect to the denominator. Therefore, a small $HWHM^*$ is preferable to a large $HWHM^*$. A more comprehensive description of $HWHM$ and its applications can be found in [17].

The denominator of Equation (2.20) represents the signal-to-noise ratio (SNR) of the observation [38].

$$SNR = (S/\sqrt{S + B}) \qquad (2.22)$$

$$S = A_{eff} Flux \Delta t \qquad (2.23)$$

$$B = A_{eff} Flux_{background} \Delta t \qquad (2.24)$$

where

A_{eff} is the effective area of the detector in cm^2

$Flux$ is the energy (or number of photons) per second passing through a unit area at the detector in photons/cm^2/sec

$Flux_{background}$ is the energy (or number of photons) per second passing through a unit area at the detector from every source other than the targeted pulsar in units of photons/cm^2/sec

Δt is the duration of the observation in seconds

Equations (2.20), (2.22), and (2.23) illustrate that an accurate TOA is dependent on an observation that maximizes the SNR by using a large area detector to observe as many photons in a short time period [38]. A more comprehensive description of pulsar timing errors and noise can be found in [13, 28, 46, 49].

2.6   TDOA Measurements

At its core, a TDOA measurement consists of one transmitter and two receivers. The sender transmits a signal which is received at the first receiver as TOA_1 (Time of Arrival 1) at time t_1. The same signal is subsequently received at the second receiver at time t_2 as TOA_2. Correlation analysis of the two TOAs yields a time delay τ_{1-2} which corresponds to a distance between the two receivers when scaled by the speed of light in the direction of the pulsar. A TDOA measurement can be defined as the time differential in TOAs between two receivers scaled by a speed to yield a distance between them in the direction of the transmitter.

The true TDOA measurement can be represented by the equation:

$$TDOA_{i-j} = c(t_i - t_j) \qquad (2.25)$$

where

t_i is the true time of arrival of the signal from the transmitter to $receiver_i$
t_j is the true time of arrival of the signal from the transmitter to $receiver_j$
c is the speed of light

Equation (2.25) cannot be used in a real world model however, because it erroneously assumes that receivers i and j were able to perfectly time-tag the TOA signals from the transmitter. A perfect timing assumption would mean either no intrinsic receiver clock errors or absolute receiver synchronization which would act to mask the clock errors between them.

To develop the operational (real world) TDOA equation, the TOAs for a pair unsynchronized (different clock biases) receivers must first be defined as:

$$TOA_{receiveri} = t_i + \delta t_i \qquad (2.26)$$

$$TOA_{receiverj} = t_j + \delta t_j \qquad (2.27)$$

where

δt_i is the time according to receiver i. It represents the clock bias intrinsic to receiver i

δt_j is the time according to receiver j. It represents the clock bias intrinsic to receiver j

The operational TDOA measurement can be generated by the equations:

$$TDOA_{i-j} = c(TOA_{receiver_i} - TOA_{receiver_j}) \tag{2.28}$$

$$TOA_i - TOA_j = t_i - t_j + \delta t_i - \delta t_j \tag{2.29}$$

$$TDOA_{i-j} = R_{i-j} + c(\delta t_i - \delta t_j) \tag{2.30}$$

where R is a distance between receiver i and j in the direction of the transmitter.

Equation (2.30) yields the relative distance between receiver i and j in the direction of the transmitter. Graphically we can depict equation (2.30) using Figure 2.9. Line r_1 represents the signal traveling from the satellite and arriving at receiver 1 at time TOA_1. Line r_2 represents the signal traveling from the satellite and arriving at receiver 2 at time TOA_2. The known distance between receivers 1 and 2 is represented as d. A unit vector in the direction of the transmitter is represented by $\hat{n}$. The segment r_2 - r_1 pictorially represents Equation (2.25), the true TDOA, when multiplied by the speed of light. Geometrically, the true TDOA of Equation (2.25) can be calculated by calculating the dot product of segment d (in vector form) with the directional unit vector $\hat{n}$. The dot product of $\vec{d}$ and $\hat{n}$ is the projection of the relative position vector $\vec{d}$ in the direction of the transmitter. Factoring in the clock errors of each receiver yields the desired TDOA measurement represented in Equation (2.30). The simulation specific TDOA measurement, based on Figure 2.9 and Equation (2.30), will be developed in Chapter 3.
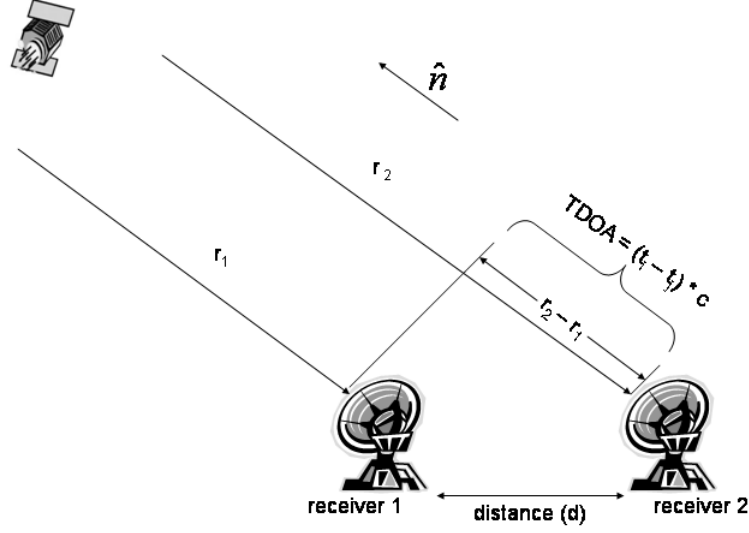
Figure 2.9: Diagram graphically depicts a time-difference-of-arrival (TDOA) measurement

2.6.1 Phase Integer Ambiguity Resolution. One characteristic of MSPs that is both beneficial and detrimental to this research is the inherent periodic stability of MSP signals. Pulsar stability aids in the generation of pulse profiles as well as TOA measurements through periodic-signal correlation. A regularly periodic signal however, also introduces phase ambiguity to the TDOA correlation process. The question arises: with a MSP periodic signal, how would each satellite know which peak was being time-tagged? In fact, the satellites, in receiving their respective TOA measurements, would only be able to discern fractional phase differences of the pulsar signal. In reality, there could be an integer number of signal peak differences, plus the fractional difference, between the peak that satellite 1 measured and the peak that satellite 2 measured. It is difficult for one satellite to know which peak was measured in relation to the other satellite because each pulse period looks identical to the one before and after it. Figure 2.10 depicts the phase ambiguity phenomena. The ambiguity is an integer number N which represents the unknown number of cycles between the true TOA point on the pulse for satellite 1 and that for satellite
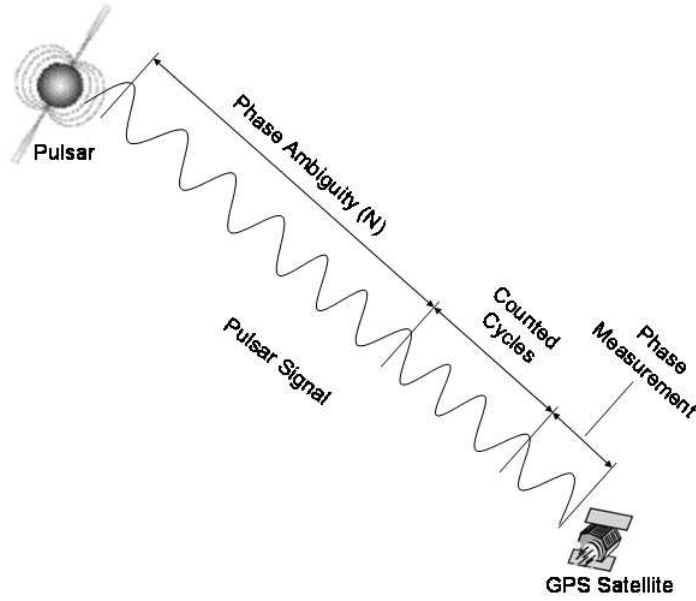
Figure 2.10:   Diagram of phase integer ambiguity

2. Resolving the phase ambiguity issue is frequently called phase integer ambiguity resolution. It is essential that ambiguity resolution be performed on the TOAs before a true TDOA measurement between satellites 1 and 2 can be determined. There are several ways to solve the problem of phase integer ambiguity which will not be covered here. However, the following comments are important to note about phase ambiguity: the ambiguity is always an integer number, the ambiguity will be different for the phase observations for different pulsars, the ambiguity will be different for each pulsar-satellite pair, and the ambiguity is constant for each pulsar-satellite pair as long as there is a continuous tracking period [41]. For a detailed discussion of a phase integer ambiguity and a list of possible solutions to this problem see [30]. For this research and simulation, it will be assumed that phase integer ambiguity resolution has been performed and the resulting TOAs represent a correlated measure of the same point on a pulsar pulse for both satellites 1 and 2.

2.7 Reference Coordinate Systems

Five different coordinate systems will be used in this research: Earth Centered Inertial (ECI) , Earth Centered Earth Fixed (ECEF), Geodetic (Latitude, Longitude, Altitude), Right Ascension/Declination(RA-Dec), and Radial / Along-Track / Cross-Track (RSW). Each coordinate system has its advantages in describing the positions of Earth-stationary objects or the motions of the GPS satellites. In this section each coordinate system will be defined and described; mathematical derivations for these coordinate systems can be found in [50] or [42]. Chapter 3 will show how these coordinate systems can used to determine satellite state vectors, and depict orbital ephemeris errors.

2.7.1 ECI Reference Frame.   The Earth Centered Inertial coordinate system, also known as ECI, is typically used when describing the motion of a satellite orbiting the Earth. This coordinate system is defined with the origin at the center of the Earth, the $\hat{X}$ axis pointing toward the vernal equinox in the equatorial plane, and the $\hat{Z}$ axis extending through the North Pole along the axis of rotation. The $\hat{Y}$ axis completes a right handed coordinate system $90°$ from the $\hat{X}$ axis in the equatorial plane. Figure 2.11 depicts this coordinate system sometimes referred to as the "IJK" frame. In reality, this coordinate system actually moves because the Earth's axis of rotation precesses with a period of 26,000 years and nutates with a period of 18.6 years. This phenomenon has the effect of slightly altering the coordinates of the reference celestial objects for coordinate system. For the purposes of this simulation, it will be assumed that these effects are negligible to the results we are trying to obtain.

2.7.2 ECEF Reference Frame.   The ECEF frame is useful for Earth-based satellite tracking operations and therefore will be used extensively in this simulation. The main difference between ECEF and ECI is the fact that the ECEF frame is always aligned with a particular meridian (usually the Prime Meridian at Greenwich) and thus rotates with the Earth. The $\hat{X}$ axis of this frame points toward a chosen
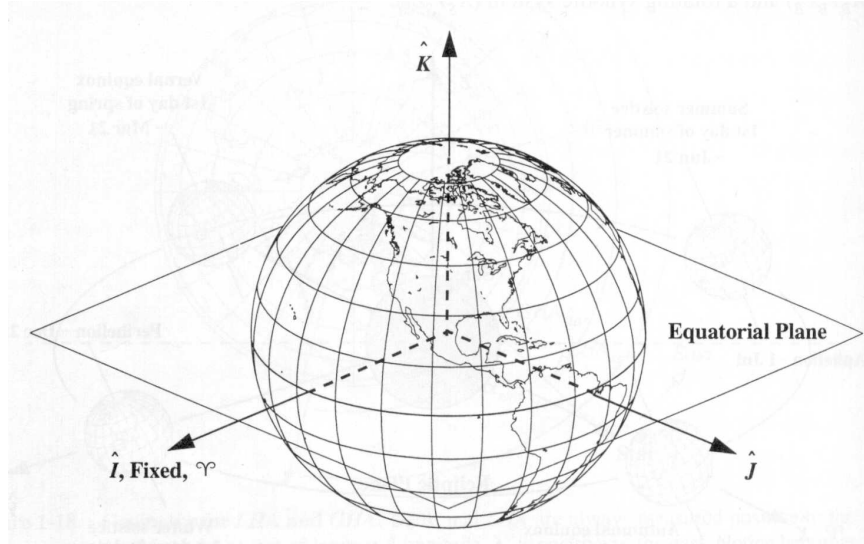
Figure 2.11:   The coordinates of ECI are commonly described
as $\overrightarrow{IJK}$ or $\overrightarrow{XYZ}$
[50]

meridian in the plane of the equator. The $\hat{Y}$ axis points 90° from the $\hat{X}$ axis in the direction of Earth rotation. The $\hat{Z}$ axis is aligned with the $\hat{Z}$ axis of the ECI frame. Figure 2.12 illustrates this coordinate system. ECEF is not considered an inertial frame because it rotates in synch with the rotation of the Earth.

2.7.3   Geodetic Reference Frame.   The geodetic coordinate frame can be used to describe the position of GPS monitor stations on the surface of the Earth. Longitude (λ) is an east-west angular displacement measured positive to the east from
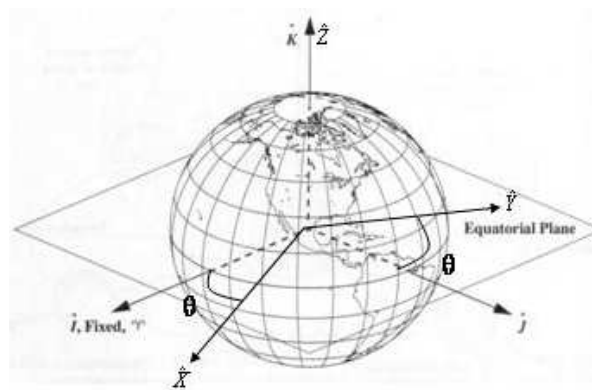

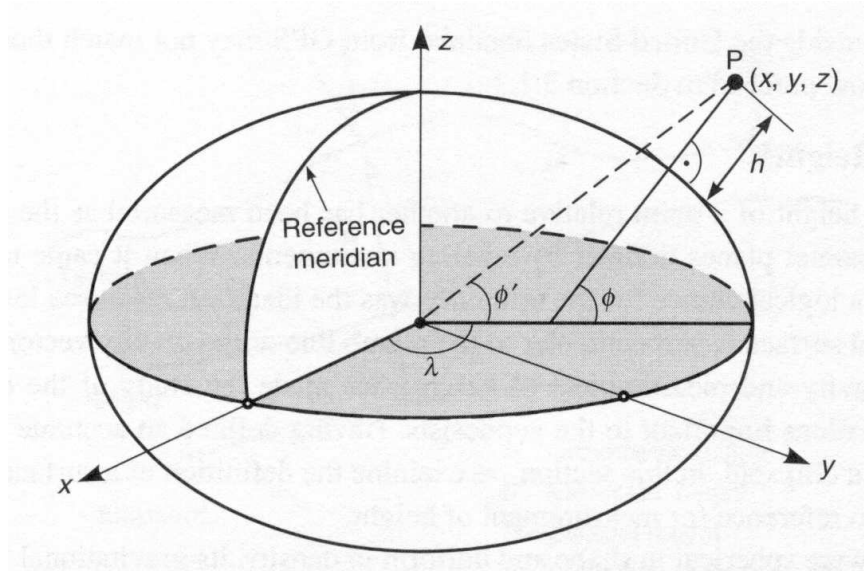Figure 2.12:   The ECEF coordinate system

Figure 2.13:   Geodetic coordinate frame [30]

the prime meridian (so traveling west from the prime meridian will yield a negative longitude angle). Latitude (ϕ) is the north-south angular displacement, referenced from the Earth's equator, measured positive traveling north from the equator into the Northern Hemisphere. Altitude (h), also known as geodetic height, is measured as positive from the local horizon up to the target. Figure 2.13 shows the geodetic frame, which is based on the surface of the Earth, and is defined by first modeling the Earth as an oblate ellipsoid. The geoid, a model based on the equipotential surface of the Earth, is fit to the oblate ellipsoid. The geoid is used for mapping, charting, and more importantly, GPS navigation. GPS uses a WGS-84 based ellipsoid to describe user positions in the geodetic frame [30].

2.7.4 Right Ascension/Declination Frame.   The right ascension, α, and declination, δ, frame is typically used by astronomers to catalog star positions. This frame is convenient for astronomical measurements because the vernal equinox, which is a fixed point in space, is used as a reference point [50]. The right ascension is measured positive to the east (0° to 360°) in the Earth's equator plane from the vernal equinox direction. The declination is positively measured northward from the
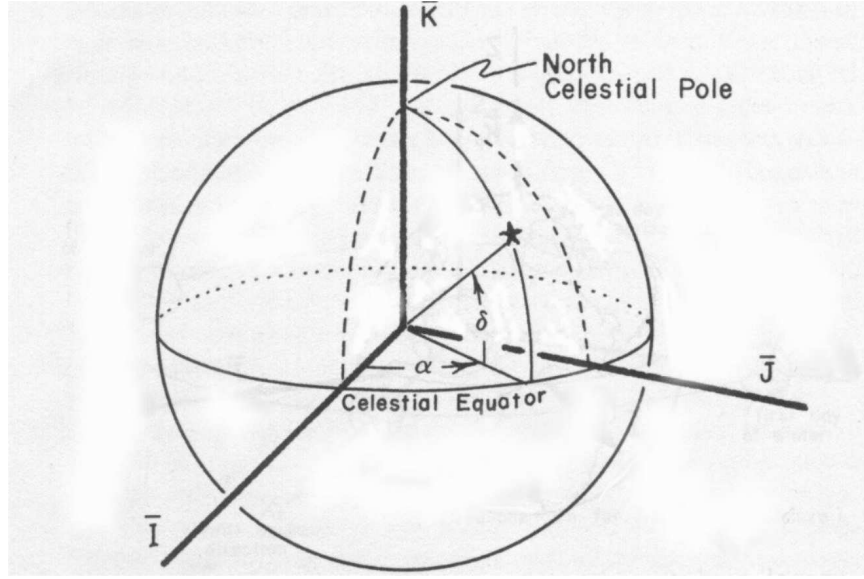
2-29

Figure 2.14:   The Right Ascension/Declination coordinate
system is typically used by astronomers to cata-
log stars. [42]

equator (0° to 90°). All declination measurements south of the equator are considered
negative (0° to -90°) [50]. Figure 2.14 illustrates this coordinate system.

   2.7.5   RSW Reference Frame.   The RSW coordinate system will be used in
this research to compute SISRE values for the GPS satellites. Figure 2.15 illustrates
this satellite-based orthogonal coordinate system that, unlike the aforementioned ref-
erence systems, moves with the satellite as it orbits. The $\hat{R}$ axis is aligned with the
radius vector that points from the center of the Earth towards the satellite as it moves.
The $\hat{S}$ axis points in the direction of the velocity vector and is perpendicular to the
radius vector. It is important to note that the $\vec{S}$ vector only aligns with the satellite
velocity vector when the orbit is circular. The $\hat{W}$ axis points 90° in the direction of
the local vertical but usually is not aligned with the $\vec{Z}$ vector of the ECI frame unless
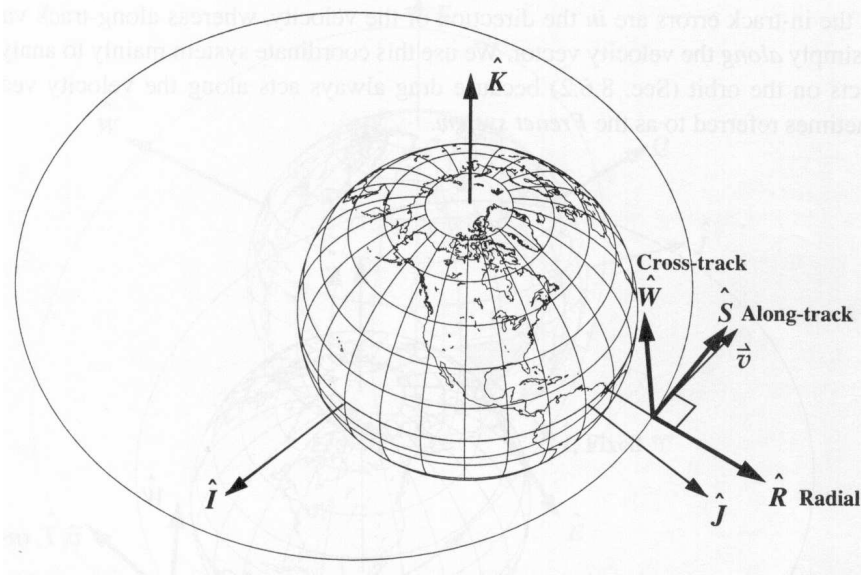the orbit is equatorial.

Figure 2.15:   The Radial, Along-track, Cross-track (RSW) co-
ordinate system. [50]

2.8   GPS Navigational Errors

GPS receivers use satellite position and clock error data together with the pseu-
dorange measurements to determine accurate user position, velocity, and time esti-
mates [20]. The total error budget for a GPS real-time PPS user (referred to as the
User Navigation Error (UNE)) can be separated into SISRE and User-Equipment
Range Error (UERE) components. UERE includes receiver noise, tropospheric re-
fraction, ionospheric delays, multipath errors, and other errors endemic to the user's
local area. SISRE comprises of errors solely associated with the GPS satellites [29].
As introduced in Chapter 1, SISRE is a measure of the fidelity of the navigation mes-
sages broadcast by the GPS satellites. Therefore, a PPS user's total navigation error
can be represented as

$$UNE(1\sigma) = GDOP\sqrt{SISRE^2 + UERE^2} \qquad (2.31)$$

where

$GDOP$ is the geometric dilution of precision
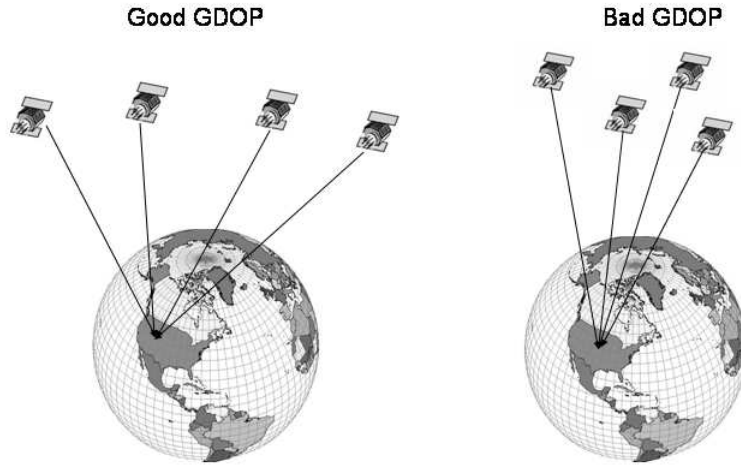$SISRE$ is the composite of all satellite-based errors

2-31

Figure 2.16:   These two diagrams illustrate instances of good
and bad GDOP geometries

$UERE$ is the composite of all user-equipment based errors

GDOP expresses the geometry of the GPS satellites relative to the receiver. Figure 2.16 illustrates instances of a good and bad GDOP. Pseudorange observation angles, which are a measure of the angles between a receiver and a group of satellites, yield increased positioning accuracies when the observation angles are farther apart [50]. GDOP is very important for GPS receiver performance theory. Indeed all receivers use a GDOP-based algorithm to select the best set of satellites available to track from among the $6-12$ satellites in view [30, 33]. Equation (2.31) tells us that GDOP is very significant in the computation of the user's navigational accuracy. In fact, geometric error is categorized as the second most significant non-environmental error source for GPS [37]. A detailed derivation of GDOP can be found in [33].

SISRE can also be decomposed into a weighted RMS of many individual errors [37].

$$SISRE = \sqrt{(R - CLK)^2 + \frac{1}{49}(A^2 + C^2)} \qquad (2.32)$$

where

R is the radial direction ephemeris error

A is the along-track direction ephemeris error

C is the cross-track direction ephemeris error

CLK is the satellite clock phase error with respect to GPS time

The first term in Equation (2.32) tells us that the radial error (R) and clock error (CLK) of SISRE are correlated – meaning that if the errors were equal, they would cancel each other and we'd be left with only the along-track and cross-track terms. Physically, this assertion makes sense because both R and CLK represent measurements to the GPS satellite projected in the direction of the range vector (the vector between the satellite and the receiver). R is a calculated range and CLK is related to the measurement of the range with respect to time - a pseudorange. The error in a pseudorange measurement is the projection of the satellite ephemeris error in the satellite-receiver line of sight [30]. The line of sight error is primarily dependent on the R component of the ephemeris error and to a lesser degree, the A and C components [30]. Equation (2.32) corroborates this SISRE component weight assignment because A and C are given a weight equal to 1/7 the weight of the ($R - CLK$) term. Figure 2.17 illustrates how the radial error is more detrimental to the line of sight range measurement than the cross-track or along-track errors [37]. For example, a 1 m radial error would directly translate into a 1 m range error, whereas because of geometry, a 1 m along-track or cross-track error would translate into a $\frac{1}{7}$ (square root of $\frac{1}{49}$) range error.

Decreasing UERE is the job of the user community through the improvements in GPS receiver technology. SISRE improvement is the responsibility of the OCS and the primary goal of this thesis. Currently, SISRE measures anywhere between $2 - 4$

m for the PPS user [29]; this research seeks to decrease this value using TDOAs to expand the measurement geometry of the GPS constellation.
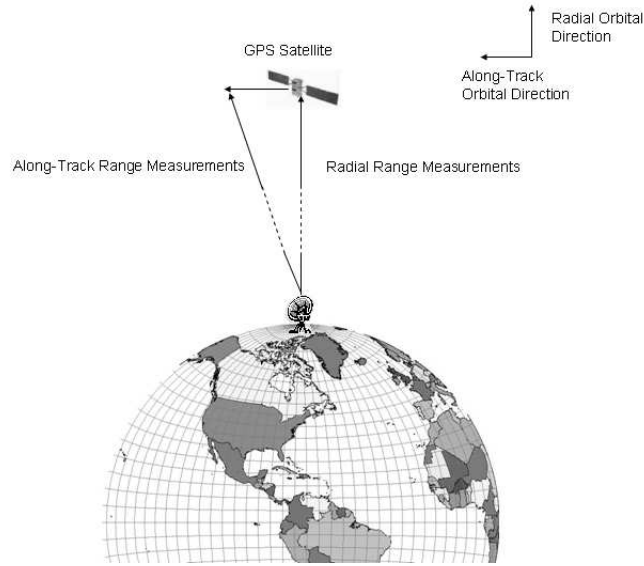

Figure 2.17: Radial range measurements have a greater effect on the overall range error than their orthogonal axes counterparts (along-track and cross-track).

2.9   Summary

This chapter presented the mathematical theory and concepts necessary to develop a GPS OCS simulation and pulsar-based TDOA scheme. An overview of the 3 segments of GPS was given. Next, current GPS Kalman filtering techniques were discussed. An introduction of the nonlinear least squares (batch) filter was given. Next, pseudoranges, x-ray signal TOAs, and TDOA measurements were presented. Finally, relevant coordinate frames were discussed. Chapter 3 will present the simulation's algorithms used to model GPS and pulsars that emit x-ray radiation.

III. GPS and Pulsar Algorithm Development

This chapter describes the methodologies, algorithms, and assumptions used to accomplish the research objectives outlined in Chapter 1. Section 3.1 gives an overview of how the simulation was set up. Section 3.2 explains the simulation's reference truth model. Section 3.3 discusses how pseudorange observations using ground stations were simulated. Section 3.4 describes how pulsars were used to develop an experimental TDOA measurement scheme between GPS satellites. Section 3.5 discusses the development of a batch filter algorithm to accommodate both pseudorange and TDOA observations. Finally Section 3.6 briefly introduces the analysis that will be presented in Chapter 4.

3.1 Introduction

3.1.1 Simulation Overview.   The objectives of this study, as stated in Chapter 1, can be summarized in five key points:

- Quantify impact of using pulsars to decrease the GPS SISRE to levels lower than pseudorange-only based SISREs.

- Conduct a tradeoff study to determine how many pulsars are needed to make pulsar measurements a significant contributor to SISRE decrease.

- Study the use of pulsars measurements in the absence of pseudoranges.

- Analyze possible advantages of using pulsars in certain galactic geometries in the attempt to decrease the SISRE.

The bullets above are the desired outputs of the simulation. In order to achieve these results, a simulation was developed of the GPS constellation, six ground stations, up to 16 pulsars, as well as the pseudorange and TDOA measurements. A top-level diagram of the simulation is shown in Figure 3.1. The simulation was implemented in Matlab®, and each block was an individual function.

Block A1 represents the simulation's truth model, including the reference trajectory. The A2 function simulated observed pseudoranges of the GPS constellation

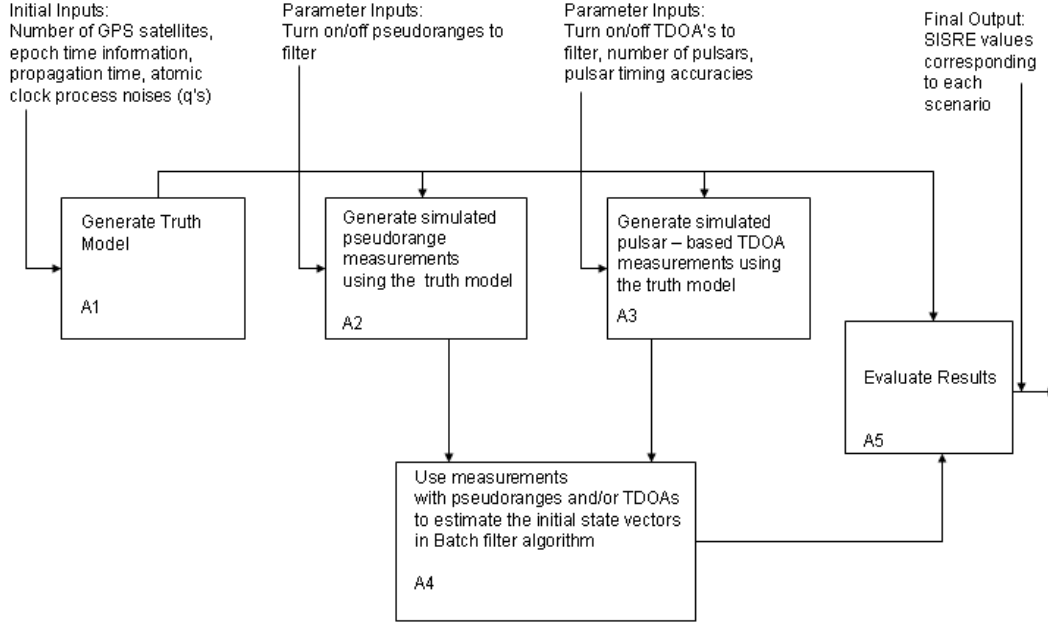## GPS / Pulsar Simulation Data Flow Diagram

Figure 3.1:   Simulation Data Flow Diagram

from six ground stations. Block A3 generated TDOA measurements between GPS satellites using x-ray signals from up to 16 pulsars. A4 contained the batch filter function which was used to estimate the state vector components of the GPS constellation. Block A5 represented the function which took the batch filter estimated state vectors and compared them with the truth trajectory state vectors using metrics such as the SISRE equation. The following sections will describe each function in detail.

3.1.2 Method of Analysis.   Several Matlab®-based scenarios were created to address the study objectives. By varying the inputs to each function block depicted in Figure 3.1, different scenarios were created to evaluate the expected improvements of TDOA measurements to the GPS SISRE. The scenarios were designed to answer the questions posed in Section 3.1.1 and Chapter 1.

3.2 Truth Model(A1)

The truth model, composed of algorithms implemented in both Fortran 90 and Matlab ®, took the predetermined positions and velocities of the GPS satellite constellation and propagated their positions and velocities forward in time.

The inputs into the truth model included an ephemeris file for each satellite and the desired propagation time. The ephemeris file describes the satellite constellation. An example is shown in Table 3.1. The files utilized were taken from the GPS Yuma almanac [23] which contains weekly cataloged ephemeris information for each GPS satellite.

Table 3.1: An example of the GPS satellite ephemeris elements used as inputs to the truth model

Parameter	Value	Description
Satellite ID	01	satellite identification number
Eccentricity	0.5290031433E-002	eccentricity of satellite orbit
Week	259	number of weeks since the GPS reference time
Time of Applicability(s)	589824.0000	time in seconds since the beginning of the GPS week
Orbital Inclination(rad)	0.9800063964	inclination of satellite orbit
Rate of Right Ascension(rads/s)	-0.8103194673E-008	time rate of change of the right ascension of the ascending node
$\sqrt{a}(m)$	5152.589355	square root of the semi-major axis
Argument of Perigee(rad)	-1.663235148	calculated argument of perigee
Mean Anomaly(rad)	-0.3063022203E+001	calculated mean anomaly
Af0(s)	0.3585815430E-003	estimated clock bias
Af1(s/s)	0.3637978807E-011	estimated clock drift

The constellation ephemeris information in Table 3.1 was used to calculate an initial position, velocity, and clock error of the satellites in the ECEF frame at the epoch time. The ECEF frame became the standard reference frame used throughout the simulation. The satellite state vector components used throughout the simulation are listed below:

3-3

- x - x-component of the satellite ECEF position

- y - y-component of the satellite ECEF position

- z - z-component of the satellite ECEF position

- $\dot{x}$ - x-component of the satellite ECEF velocity

- $\dot{y}$ - y-component of the satellite ECEF velocity

- $\dot{z}$ - z-component of the satellite ECEF velocity

- clock bias - intrinsic clock error of each satellite and ground station

- clock drift - time rate of change of the clock bias

Using a Runge-Kutta fourth-order numerical integrator, the ECEF state vector components for each satellite were propagated forward in time to a designated t_{final} time. Thus, the final output for the truth model was a set of propagated ECEF state vector components for each satellite at each time step.

3.2.1   Equations of Motion.   In order to prove the concept of SISRE improvement, only the fundamental two-body satellite dynamics were modeled in the Runge-Kutta algorithm. Lagrangian dynamics were used to propagate the state vector for each satellite. The Lagrangian function in the inertial frame is:

$$L = \frac{1}{2}(\dot{x}_{ECI}^2 + \dot{y}_{ECI}^2 + \dot{z}_{ECI}^2) - V \tag{3.1}$$

$$V = \frac{-\mu}{r} \tag{3.2}$$

where

$\dot{x}$, $\dot{y}$, $\dot{z}$ are the inertial velocity components
V is the Earth geopotential per unit mass of the satellite
μ is the Earth's gravitational constant
r is the distance of the satellite from the center of the Earth

Using the transport theorem, the inertial velocity components can be converted to the ECEF frame which is the reference coordinate system of the GPS system

3-4

$$\vec{v}_{ECI} = \vec{v}_{ECEF} + \omega_\oplus \times \vec{r}_{ECEF} \tag{3.3}$$

where

$\vec{v}_{ECI}$ is the inertial velocity vector

$\vec{v}_{ECEF}$ is the ECEF velocity vector

$\omega_\oplus$ is the rotational velocity of the Earth (assumed to be constant)

The ECEF frame Lagrangian function now becomes

$$L = \frac{1}{2}[(\dot{x}_{ECEF} - \omega_\oplus y_{ECEF})^2 + (\dot{y}_{ECEF} + \omega_\oplus x_{ECEF})^2 + \dot{z}_{ECEF}^2] - V \tag{3.4}$$

All x, y, z components are now assumed to be in the ECEF frame and subsequently all ECEF subscripts will be dropped for simplicity.

The equations of motion in the ECEF frame can now be obtained from the Lagrange's equations of motion

$$\frac{d}{dt}\left(\frac{\partial L}{\partial \dot{X}}\right) - \frac{\partial L}{\partial X} = 0 \tag{3.5}$$

where

L is the Lagrangian function based in the ECEF frame from Equation (3.4)

$\dot{X}$ represents a vector of velocity state components $\dot{x}$, $\dot{y}$, and $\dot{z}$

X represents a vector of position state components x, y, and z

Equation (3.5) resolves into three independent equations of motion representing the x, y, and z components of motion. The component terms of Equation (3.5) for x resolve to become

$$\frac{d}{dt}\left(\frac{\partial L}{\partial \dot{X}}\right) = \ddot{x} - \omega_\oplus \dot{y} \tag{3.6}$$

3-5

$$\frac{\partial L}{\partial X} = (\dot{y} + \omega_\oplus x)\omega_\oplus - \frac{\partial V}{\partial x} \tag{3.7}$$

Subtracting the terms of Equations (3.6) and (3.7) according to Equation (3.5) yields

$$\ddot{x} - 2\omega_\oplus \dot{y} - \omega_\oplus^2 x = -\frac{\partial V}{\partial x} \tag{3.8}$$

where

$$\frac{\partial V}{\partial x} = \frac{\mu x}{r^3} \tag{3.9}$$

and

$$r = \sqrt{(x^2 + y^2 + z^2)} \tag{3.10}$$

Applying a method similar to that mentioned above for y and z components, the final three independent equations of motion for x, y, and z become

$$\ddot{x} - 2\omega_\oplus \dot{y} - \omega_\oplus^2 x = -\frac{\mu x}{r^3} \tag{3.11}$$

$$\ddot{y} + 2\omega_\oplus \dot{x} - \omega_\oplus^2 y = -\frac{\mu y}{r^3} \tag{3.12}$$

$$\ddot{z} = -\frac{\mu z}{r^3} \tag{3.13}$$

Equations (3.11), (3.12), (3.13) were solved by transforming each second-order differential equation into two first-order differential equations. Integrating these 6 components of Lagrange's equations yielded the 6 (x, y, z, $\dot{x}$, $\dot{y}$, $\dot{z}$) ECEF-based equations of motion for the GPS satellites.

3.2.2   Orbital Perturbations.   The most significant force acting on any given GPS satellite is the Earth's central gravitational force (geopotential) which adds accelerations of approximately .56 m/s^2 to the motion of the satellites [30]. Other orbital perturbation forces such as solar/lunar gravity, solar radiation, drag, etc., contribute far less acceleration to the satellites' motion ($\leq 10^{-6}$ m/s^2) [30]. Although a simple

two-body satellite dynamics model was used in this research, the Runge-Kutta algorithm could be modified to incorporate lesser acceleration terms (e.g., solar radiation, three-body dynamics, etc.) for a higher fidelity simulation model.

The primary perturbation for this simulation came from the highest order term of the gravitational geopotential model, which is represented by Equation (3.2). To simulate a higher fidelity Earth geopotential, a WGS 84 Earth Gravitational Model 96 (EGM96) function developed by NASA/NIMA can be used. The EGM96 gravitational potential function is modeled as [30]:

$$V(r, \phi', \lambda) = \frac{\mu}{r}[1 + \sum_{n=2}^{maxord} \sum_{m=0}^{n} \left(\frac{a}{r}\right)^n P_{nm}(sin\phi')(C_{nm}cos(m\lambda) + S_{nm}sin(m\lambda))] \quad (3.14)$$

where

    n and m are the spherical harmonic indices degree and order respectively

    μ is the Earth's gravitational constant

    ϕ' is the geocentric latitude

    r is the radius of the satellite's orbit from the center of the Earth

    λ is the longitude

    a is the semi-major axis length of the WGS 84 ellipsoid

    P_{nm} are the associated Legendre functions and polynomials

    C_{nm} and S_{nm} are the spherical harmonic coefficients used to describe the gravity field

    $maxord$ is the maximum order of the geopotential

The degree(n) and order(m) of the coefficients ranged from 0 to a maximum value of 50. To ensure that a truth model represented a highly accurate trajectory, a simulation could propagate the GPS satellite equations of motion using a 50 by 50 (order/degree) geopotential function.

For this simulation, it was determined that a two-body physics model would be sufficient to conduct research on relative SISRE improvement with the introduction

of TDOAs. It is important to note that a more realistic simulation would model the small stochastic perturbations (e.g., y-axis bias) that slowly build up over time if not accounted for. It is not necessary to model the large, deterministic errors such as solar/lunar gravity because the GPS operational Kalman filter is able to deterministically account for these large effects on the GPS satellite orbits. However, the stochastic perturbations cannot be deterministically eliminated. Therefore, in order to generate operationally realistic SISREs for the GPS constellation, it is recommended that only the small effects of the stochastic errors be incorporated into the batch filter because it can be assumed that the large error sources have been accounted for.

Lastly, it should be emphasized that the results of this simulation, even without the implementation of small perturbing forces, can still be considered valid. In an orbit determination problem, most of the perturbing force acceleration for a satellite in Medium Earth Orbit (MEO) comes from the Earth's central gravity force – which has been accounted for by the 2-body propagator in this simulation. The incorporation of small perturbations was desired for realism but, as stated earlier, take time to build up in a satellite's orbit. It has been assumed that relative SISRE magnitudes will not be significantly affected by the omittance of the small perturbations affecting GPS satellites. Therefore, the central goal of analyzing the **relative** SISRE behavior of the GPS constellation with the introduction of TDOAs is still a valid and attainable goal with the 2-body orbit propagator.

3.2.3 Clock Model. At the heart of GPS is a system of precisely synchronized clocks. Satellite clock synchronization is achieved by estimating the time offset, drift, and drift rate of each satellite clock relative to GPS time and transmitting the clock parameters of this estimated model in the satellite's navigation message. Subsequently, each satellite broadcasts its characteristic clock parameters to the user [30].

This research was concerned with properly simulating the real performance of Cs and Rb atomic clocks used by the GPS satellites and monitor stations in the truth model. Therefore, the true GPS clock performance had to be measured and

approximated for use in the batch filter estimator. Without accurately estimating the time dependent clock errors of GPS, it would not have been possible to correctly simulate the satellite positions and velocities or model the pseudorange measurements between the monitor stations and the satellites. We start first with the development of the equations and concepts of a GPS atomic clock truth model.

The performance of atomic clocks can be simulated using a 3-state polynomial process driven by white noise. The discrete process model and its covariance can be written as [6]:

$$\Phi(\tau) = \begin{bmatrix} 1 & \tau & \frac{1}{2}\tau^2 \\ 0 & 1 & \tau \\ 0 & 0 & 1 \end{bmatrix} \tag{3.15}$$

$$\begin{bmatrix} x_1(t_{k+1}) \\ x_2(t_{k+1}) \\ x_3(t_{k+1}) \end{bmatrix} = \begin{bmatrix} 1 & \tau & \frac{1}{2}\tau^2 \\ 0 & 1 & \tau \\ 0 & 0 & 1 \end{bmatrix} \begin{bmatrix} x_1(t_k) \\ x_2(t_k) \\ x_3(t_k) \end{bmatrix} + \begin{bmatrix} w_1(k) \\ w_2(k) \\ w_3(k) \end{bmatrix} \tag{3.16}$$

$$Q_k(\tau) = E\left[w(k)w(k)^T\right] = \begin{bmatrix} q_1\tau + \frac{1}{3}q_2\tau^3 + \frac{1}{20}q_3\tau^5 & \frac{1}{2}q_2\tau^2 + \frac{1}{8}q_3\tau^4 & \frac{1}{6}q_3\tau^3 \\ \frac{1}{2}q_2\tau^2 + \frac{1}{8}q_3\tau^4 & q_2\tau + \frac{1}{3}q_3\tau^3 & \frac{1}{2}q_3\tau^2 \\ \frac{1}{6}q_3\tau^3 & \frac{1}{2}q^3\tau^2 & q_3\tau \end{bmatrix} \tag{3.17}$$

where

$x_1(t_k)$ and $x_1(t_{k+1})$ are the clock bias error at times t_k and t_{k+1}
$x_2(t_k)$ and $x_2(t_{k+1})$ are the clock drift error at times t_k and t_{k+1}
$x_3(t_k)$ and $x_3(t_{k+1})$ are the clock drift rate error at times t_k and t_{k+1}
$\tau = t_{k+1}\text{-}t_k$, the time interval
$w_1(k)$, $w_2(k)$, and $w_3(k)$ are independent white noises
q_1, q_2, and q_3 are the continuous process noise power spectral densities representing the bias, drift, and drift rate respectively

$\Phi(\tau)$ is the state transition matrix which propagates the current clock bias, drift, and drift rate errors forward in time from t_k to t_{k+1}. The clock process noise

terms are w_1, w_2, and w_3. The clocks, because of their stochastic nature, cannot be modeled deterministically. By modeling the performances of the random walk noise values w_1, w_2, and w_3, the characteristic Allan Variance curves of the atomic frequency standards can be matched [7]. Figure 3.2 depicts an example of a 3-state random clock process. Drawing a best fit curve through the plot, it is evident that the performance of a three-state atomic clock is quadratic in nature.
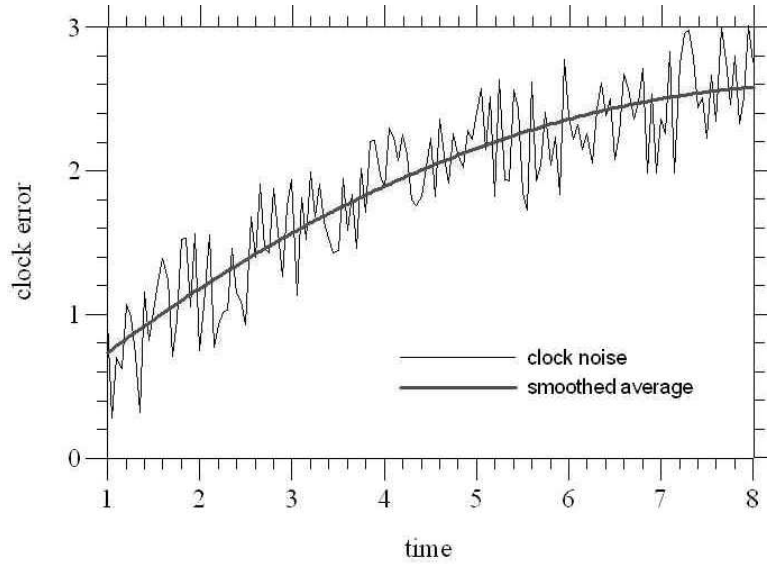

Figure 3.2:   Comparison of simulated clock error and quadratic fit (used in batch filter)

The statistics of w_1, w_2, and w_3 are determined by the values of the variance elements (q_n) of Q_k in Equation (3.17) [5].

As was stated earlier in Section 1.5.1.1, each GPS satellite depends on either a Cesium (Cs) or Rubidium (Rb) clock to provide a stable output frequency. This simulation used research conducted in the Clock Improvement Initiative [21] to choose q values for Equation (3.17). Table 3.2 shows the resulting q values for the Rb and Cs clocks following the conclusion of the Clock Improvement Initiative [21].

In order to calculate each GPS satellite clock's 3-state random process in the simulation, initial clock bias and drift parameters were gathered from [23] for each satellite. The initial drift rate (derivative of drift) for each GPS clock was assigned

3-10

Table 3.2:   Process Noise Values for GPS Rb and Cs Clocks

	Rubidium Clock	Cesium Clock
q_1 (bias)	$1.11 \times 10^{-22} s^2/\text{s}$	$4.44 \times 10^{-22} s^2/\text{s}$
q_2 (drift)	$2.22 \times 10^{-32} s^2/s^3$	$3.33 \times 10^{-32} s^2/s^3$
q_3 (drift rate)	$6.66 \times 10^{-45} s^2/s^5$	$0 s^2/s^5$

a value of zero. The bias, drift, and drift rate initial values were propagated each time step using Equation (3.16). In order to calculate the w_1, w_2, and w_3 terms of each GPS clock for each time step, Equation (3.17) was multiplied by a Matlab® random number generator in order to scale the amount of random walk for each clock at each time step. Rb clock q values were chosen for each GPS clock because of the singularity that the Cs clock q_3 value created when propagating the clock states with the 3-state model being implemented.

3.2.4 Ground Stations.   In order to replicate operational pseudorange observations, the locations of the six current global ground stations were simulated. Table 3.3 lists the six ground stations used to observe and track the positions of the GPS satellites [48].

The operational clock biases, drifts, and drift rates for all ground stations were approximated in the simulation to be similar to the satellites. Scaled by the range of known clock bias and clock drift terms for GPS satellite constellation, each ground station was given a random initial bias and drift. The drift rate was assumed to start at zero for each ground station. The ground station clocks were subsequently propagated using the satellite clock propagation procedure explained in Section 3.2.3.

3.3 Pseudoranges(A2)

Using the state vector outputs of the truth model in block A1, block A2's function was to convert satellite state vectors into pseudorange observations. The pseudoranges were meant to simulate imperfect measurements of the true GPS satellite

positions generated in block A1 from one of the six ground stations located around the Earth.

    3.3.1   Pseudorange Calculation.   In order to calculate the set of possible pseudorange observations for a given simulation time period, the simulation first had to determine which satellites were visible for each ground station location at each time step. The visibility of each satellite by each ground station is a function of the satellite position and ground station position. A satellite was defined as visible from a ground station if the satellite's elevation was greater than 0 deg. Elevation is defined as the angle measured from the local horizon up to the satellite position vector in the topocentric-horizon based SEZ (south-east-zenith) frame. The elevation angle is depicted in Figure 3.3.

Table 3.3:   Ground Station Locations

Location	Latitude (North)	Longitude (East)
Cape Canaveral	28.4 deg	279.4 deg
Ascension Island	-8.0 deg	345.6 deg
Diego Garcia	-7.3 deg	72.4 deg
Kwajalein Atoll	8.7 deg	167.7 deg
Colorado Springs	38.8 deg	255.2 deg
Hawaii	21.2 deg	202.5 deg

    An elevation calculation algorithm was designed to keep track of every satellite's position with respect to each ground station location. An elevation angle was calculated for each satellite-ground station pair for each time step. The algorithm stored every satellite-ground station pair where the elevation angle was above 0 deg. The A2 function block generated pseudoranges for all visible (elevation > 0 deg) satellite-ground station pairs.

    To calculate each pseudorange, a geometric distance was first calculated using Equation (2.18). For each geometric range, measurement errors were added to simulate actual measurements. It is the measurement errors that convert a geometric
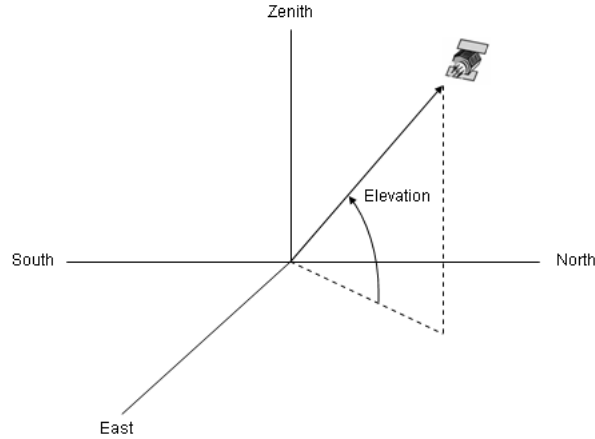
3-12

Figure 3.3:   The satellite elevation angle is measured from the
local horizon up to the satellite position vector.

range into a pseudorange. The measurement errors modeled in this simulation will
be described in the next section.

3.3.2   Pseudorange Measurement Effects.   The clock and measurement er-
rors that exist between each satellite-ground station pair yield uncertainties in Equa-
tion (2.18) that must be accounted for before the position of each satellite can be
determined. This simulation modeled four major sources of signal error - clock bias,
tropospheric delay, multipath delay, and receiver error due to noise. Other signal
propagation sources of error that exist between any given satellite-ground station
pair, such as ionospheric delay and relativism, were not explicitly modeled. These
and other errors were accounted for because of either their deterministic nature or
because they were negligible compared to the other modeled errors.

3.3.2.1   Pseudorange Clock Errors.   Before the clock biases of the satel-
lites and ground stations can be understood, we must first understand the composite

3-13

time, called GPS Time (GPST), which provides a common reference. GPST is defined as a composite time because there is no master clock that serves as the benchmark for its output time. GPST is derived from a set of measurements of the atomic frequency standards that reside in every satellite and ground station [30]. Using a Kalman-Bucy filter, all the clocks are estimated together to create an ensemble time [6]. The bias of a satellite and ground station in a pseudorange measurement can be represented as:

$$\delta t_{sat} = t_{sat} - t_{GPS} \tag{3.18}$$

$$\delta t_{G/S} = t_{G/S} - t_{GPS} \tag{3.19}$$

where

δt_{sat} and $\delta t_{G/S}$ are the clock biases of the GPS satellites and ground stations respectively

t_{sat} and $t_{G/S}$ are the times kept by the satellite and ground station clocks respectively

t_{GPS} is the composite GPS system time

The deviations of each individual satellite and ground station clock from the composite GPST are represented by δt_{sat} and $\delta t_{G/S}$ [30]. As explained in Section 2.4, the inherent clock biases of each satellite and ground station affect our ability to measure the true transmission and reception time of a signal from the satellites to the Earth. The clock biases distort the true measurement of satellite position calculated in Equation (2.18).

3.3.2.2 Tropospheric Delay. In addition to the clock biases that affect our measurements of the satellite transmitted signals, GPS signals are also delayed and refracted on their path to the receiver because of effects in the tropospheric region of the atmosphere. The troposphere can be characterized as the lower neutral part of the atmosphere. The GPS signal delays in this region are a function of the atmospheric pressure, temperature, and humidity [50]. Knowledge of these tropospheric

effects allows one to model the refractivity and corresponding signal delays due to the troposphere.

The tropospheric errors for each site were functions of the ground station altitudes, the local relative humidity at each site, as well as satellite elevation angles for each satellite-ground station pseudorange pair. To calculate tropospheric errors at each ground station, a tropospheric error value was calculated by defining modeled and true tropospheric delay values for each ground station. The modeled tropospheric errors used a relative humidity of 50%. The true tropospheric values used a random relative humidity of 50% +/- 10%. The tropospheric errors for each site were calculated by differencing the modeled and true tropospheric values. Using a modified Hopefield tropospheric model, a tropospheric delay value was assigned to each pseudorange observation. This approach simulates the effect of not having a perfect model of the troposphere at each ground station (which is true in of the operational GPS system).

3.3.2.3 Multipath Delay. Another major error source in GPS signal propagation is the effect of multipath. Multipath occurs when GPS signals, reflected off of another surface, simultaneously arrive together at a receiver with unimpeded (nonreflected) signals from the same source [50]. Mathematically modeling (and correcting for) multipath errors is not feasible because the errors depend on complex factors involving the geometry of the situation. Multipath is more likely to occur in a city with many buildings than in the middle of the ocean. Solutions to the problem of multipath will not be detailed here but can be found in [30] and [50]. In this simulation, multipath was modeled as a white, Gaussian random error with a standard deviation of 1.4 m [33]. The random multipath delay values were added to each pseudorange observation. Note that real multipath errors will tend to be time-correlated, and a more realistic multipath error model would attempt to take this into account.

3.3.2.4 Receiver Error. Finally, other systematic unmodeled pseudorange errors are characterized in a noise term that include receiver noise and miscel-

laneous system hardware errors. The signal delays accounted for in this term include noise from antennas, amplifiers, cables, interference from other GPS signals and GPS-like broadcast signals [30]. In this simulation, receiver error was modeled as a white, Gaussian random error with a standard deviation of .5 m [33].

3.3.3 A2 Block Output. The "noised" pseudorange equation can be expressed as:

$$\rho = \sqrt{(x_{sat} - x_{G/S})^2 + (y_{sat} - y_{G/S})^2 + (z_{sat} - z_{G/S})^2} + c(\delta t_{G/S} - \delta t_{sat}) + \nu_{PR} \quad (3.20)$$

$$\nu_{PR} = c(\delta t_{tropo} + \delta t_{multipath} + \varepsilon_{noise}) \quad (3.21)$$

where

$x_{sat}, y_{sat}, z_{sat}$ is the ECEF position of the GPS satellite

$x_{G/S}, y_{G/S}, z_{G/S}$ is the ECEF position of the ground station

$x_{trans}, y_{trans}, z_{trans}$ is the position of the transmitter

δt_{tropo} is the delay in signal due to tropospheric effects expressed in units of seconds

δt_{tropo} is the delay in signal due to multipath effects expressed in units of seconds

δt_{tropo} is the delay in signal due to ground station noise and receiver hardware errors expressed in units of seconds

ν_{PR} is the combined pseudorange error term expressed in units of meters

c is the speed of light in meters per second

Block A2 passed out calculated values of Equation (3.20) into the simulation batch filter (block A4). Block A2's pseudoranges represented real world observations of the GPS constellation. These observations will be used later in block A4 to calculate measurement residuals for the batch filter.

3.4 Pulsar Based TDOAs(A3)

Block A3, in Figure 3.1, represented the generation of operational TDOA measurements using a bank of selected millisecond pulsars as the transmitters and pairs of GPS satellites as the receivers. Table 3.4 lists the pulsars used in this simulation. For each simulation scenario, various pulsars were selected to be utilized for that particular experiment; all pulsars were not necessarily used simultaneously. Pulsars were chosen based on their attributes that matched the following set of criteria:

- Pulsars had to be millisecond pulsars exhibiting rotation periods ranging between 1.5 ms and 30 ms

- Pulsars had to emit radiation in the x-ray waveband

- Pulsars had to emit pulsed radiation and not solely point radiation

- Pulsar fluxes or pulsed luminosities must have been observed in the x-ray wave band

As stated in Chapter 2, the pulsar name describes the pulsar direction (RA/Dec) in terms of degrees, hours, and minutes. In order to be useful, pulsar directions were converted to decimal degrees then subsequently into the ECEF frame. This procedure will be outlined in the next section.

The flux attribute was approximated for each pulsar. Using references [4,36,51], the flux, in units of $ergs/cm^2/s$ was converted to $photons/cm^2/s$, because the desired measurement for the detector would be the number of photons that pass through the detector area per second and not just the total energy that was detected. Based on the millisecond pulsar criteria outlined in Section 2.5.3, the Crab Pulsar does not meet the requirements for the pulsar selection process. However, the Crab Pulsar's relatively large flux value and near-millisecond pulsar period made it advantageous to the simulation in terms of the low σ_{TOA} it could provide for the TDOA measurements. Sample flux calculations are presented in Appendix B.

Table 3.4:   Characteristics of the pulsars used in this simulation [4, 36, 38, 43, 51]

Pulsar	Period (s)	Flux (photons/cm^2/s)	Observation Energy Level (keV/photon)
B0531+21 (Crab Pulsar)	.0334	10.34375	0.6
B1821-24	0.00305	0.000710227	1.1
B1937+21	0.001557	0.00023125	1.0
B1257+12	0.00622	0.00001375	0.5
B1820-30A	0.00544	1.21	2.5
B1620-26	0.001107	0.0000125	0.5
J1012+5307	0.00525	0.000015625	0.5
J0218+4232	0.00232	0.0001075	2.5
J0751+1807	0.00347	0.000053625	0.5
J2322+20	0.0048	0.0000075	0.5
J2019+24	0.00393	0.000022375	0.5
J2124-3358	0.00493	0.00010325	0.5
J1024-0719	0.00516	0.000011075	0.5
J1744-1134	0.00407	0.00000805	0.5
J0030+0451	0.00486	0.00015875	0.5
J0437-4715	0.00575	0.0005375	0.5

The pulsar flux is a function of the energy level at which it is observed (see Appendix B). Operationally, the telescopes observe pulsar fluxes over an energy range in units of kilo-electron volts (keV) per photon [4, 36, 51]. The pulsars used in this simulation were observed at energy levels that ranged from 0.1 - 10 keV [4, 36, 51]. As an approximation, the pulsar fluxes in this simulation were calculated at specifically chosen energy levels within their stated range.

It is important to note that this research attempted to approximate reasonable flux values for the set of pulsars in Table 3.4. For pulsars J1012+5307, J0751+1807, B1257+12, B1820-30A, B1620-26, J2322+20, J2019+24, J1024-0719, and J1744-1134 there is uncertainty in the actual x-ray pulse characteristics that contribute to their flux. However, for the purposes of this simulation it was important to simulate the ability to collect x-ray signals from a varying range of bright and dim galactic x-ray sources in a widely dispersed geometry and use them to create TDOA observations. Subsequent simulations that are not concerned solely with proving the concept of

TDOA observations might only use the pulsars that are widely known to exhibit observable, identifiable, pulse profiles. The following pulsars are recommended for an operationally accurate simulation because their attributes (e.g., flux, period) have been experimentally verified - PSRs B0531+21, J0437-4715, B1821-24, J2124-3358, B1937+21, and J0030+0451.

3.4.1 TDOA Calculation. In order to use the pulsars in the TDOA observations, their positions had to be converted from a RA/Dec frame to the ECEF frame – the reference coordinate system of GPS. All pulsars were first converted to the J2000.0 coordinate system if they were not already expressed as such. The RA/Dec coordinates of each pulsar were subsequently converted to ECI unit vectors. The position of each pulsar can only be expressed as a unit vector because the RA/Dec frame is directional based and not distance based. Pulsar distances are so large that they are essentially considered to be at infinity for the simulation [38]. The ECI unit vectors were then converted to the ECEF frame. In the ECI frame these vectors are constant, because the inertial positions of the pulsars are constant. However, in the ECEF frame, the pulsar unit vectors rotate once per day with the Earth. Physically, this concept makes sense because observers in the ECEF frame (i.e., on the Earth's surface) observe the stars rising and setting each day.

To account for this time varying phenomenon in the simulation, the initial position of each pulsar was rotated to its next position at the next time step using successive rotations about the third axis (z-axis). It was assumed that the Earth's rotation is constant and therefore the following equation could be used to rotate from one ECEF position to another:

$$ECEF_{k+1} = \begin{pmatrix} \cos(\omega t) & \sin(\omega t) & 0 \\ -\sin(\omega t) & \cos(\omega t) & 0 \\ 0 & 0 & 1 \end{pmatrix} ECEF_k \qquad (3.22)$$

where

ECEF is the position unit vector of the pulsars

t is the time step interval

k is the current time

$k + 1$ is the future time step

ω is the Earth's rotational velocity

Figure 3.4 depicts the successive rotations from the inertial ECI frame to the ECEF frames at each time step.

Using the propagated pulsar positions combined with the A1 generated satellite propagated positions, a visibility algorithm was implemented to determine which satellites could see which pulsars at every time step. Figure 3.5 illustrates how pulsar-satellite visibility requirements were satisfied.
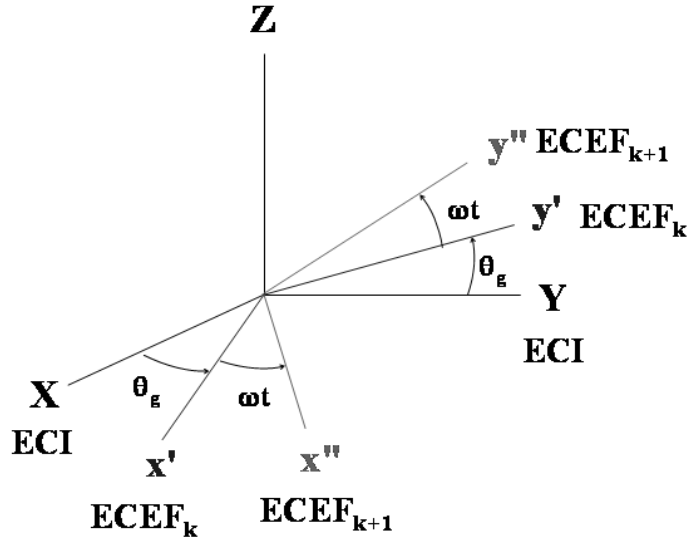
Figure 3.4:   In the ECEF frame the positions of the pulsar are not constant and in fact rotate once per day with the Earth's rotation. θ_g represents the rotation angle between the ECI and ECEF frames. At each successive time step, the Earth's rotational velocity (ω) is multiplied by the elapsed time interval (t) since epoch to yield the pulsars' new ECEF position at time $k+1$
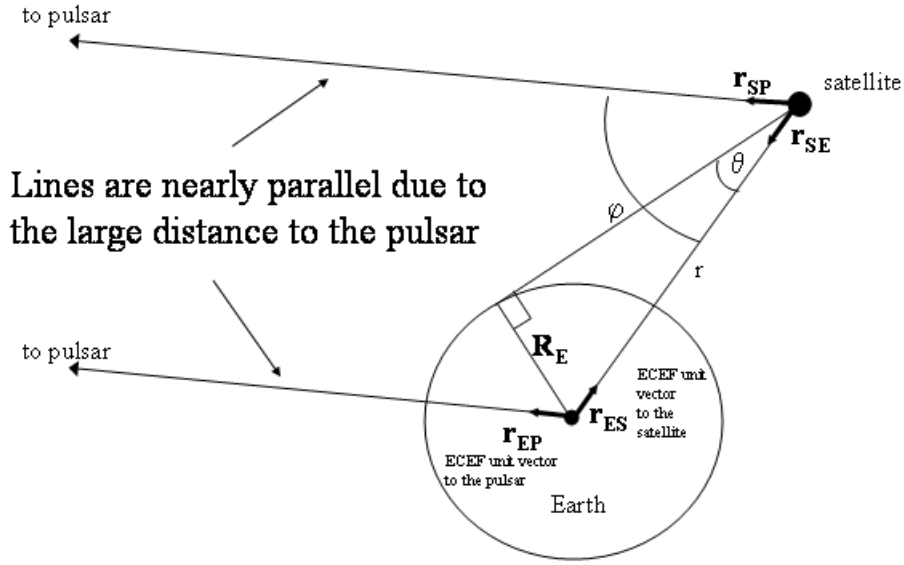
Figure 3.5:   Pulsar Visibility Diagram

The central assumption made during the implementation of the pulsar visibility algorithm was that the distances of all pulsars from the Earth is so great that they approach infinity when compared to the Medium Earth Orbit (MEO) distances of the GPS constellation. Therefore, the unit vectors from the Earth to the pulsar and from the satellite to the pulsar are essentially parallel as depicted in Figure 3.5. Following the vectors and angles presented in Figure 3.5 and using the infinite distance assumption, it can be said that:

$$\hat{r}_{SP} \cong \hat{r}_{EP} \tag{3.23}$$

where

$\hat{r}_{SP}$ is the ECEF unit vector from the satellite to the pulsar

3-21

$\hat{r}_{EP}$ is the ECEF unit vector from the center of the Earth to the pulsar

and since

$$\hat{r}_{SE} = -\hat{r}_{ES}$$

$$\cos\varphi = \hat{r}_{SE} \cdot \hat{r}_{SP} = -\hat{r}_{ES} \cdot \hat{r}_{EP}$$

the angle φ can be calculated as

$$\varphi = \arccos(-\hat{r}_{ES} \cdot \hat{r}_{EP})$$

Finally, the angle θ can be computed using the equations,

$$\sin\theta = \frac{R_E}{r}$$

$$\theta = \arcsin\left(\frac{R_E}{r}\right)$$

It can therefore be said that a pulsar will only be visible to any given satellite when $\varphi \geq \theta$. The pulsar visibility algorithm used the above equations to determine which satellites were able to detect x-ray signals from one of the pulsars utilized in the simulation. If $\varphi \leq \theta$, then that TOA was discarded due to the pulsar signal being blocked by the Earth.

Perfect TDOAs were calculated by projecting the distance between the satellites in the direction of the transmitting pulsar source. Using the concepts developed in Chapter 2, a perfect (unnoised and unbiased) TDOA was represented as:

$$TDOA_{i-j} = (\vec{r}_i - \vec{r}_j) \cdot \hat{n} \tag{3.24}$$

where

$\vec{r}_i$ is the ECEF position vector of satellite i

$\vec{r}_j$ is the ECEF position vector of satellite j

$\hat{n}$ is the unit vector in the direction of the transmitting pulsar

Mathematically, the projection of the distance between satellites in the direction of the pulsar was accomplished by computing the dot product of the satellite distance vector and the pulsar direction vector. Equation (3.24) corresponds to the R_{i-j} term in Equation (2.30). Figure 3.6 graphically depicts Equation (3.24) and is analogous to Figure 2.9.
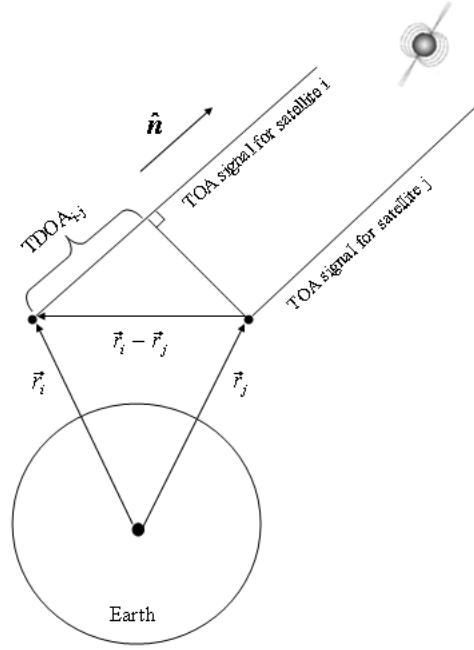
Figure 3.6:   TDOA Diagram

3.4.2   TDOA Measurement Effects.

3.4.2.1   Clock Bias.   Satellite clock biases were added to Equation (3.24) to account for the timing errors between satellite i and satellite j. The TDOA clock bias concept was described in Section 2.6 by Equation (2.30).

3.4.2.2   TOA Measurement Errors.   The error in measuring a pulsar signal TOA is embodied in Equation (2.20). This section will outline how each component of Equation (2.20) was calculated for the simulation. The operational method for determining *HWHM* for a pulsar pulse was described in Chapter 2. However, *HWHM* was approximated in this simulation using two assumptions:

- Each pulse width was approximated as a Gaussian curve which forced the *HWHM* to represent the 1σ value of a pulsar pulse [38, 43]

- The pulse widths of pulsars can typically be approximated by using anywhere from 2% to 20% of their pulse periods [38, 43]

Physically, these assumptions make sense when a Gaussian shaped pulsar pulse is visualized. As stated in Chapter 2, the fundamental goal of pulsar pulse timing is to measure the location of the pulse peak as accurately as possible. Geometrically, it is easier to precisely determine the peak location of a narrow pulse than if the pulse was wider and flattened. A *HWHM* that is approximated by 2% of its period would make each pulsar pulse appear narrower and correspondingly, a *HWHM* approximated by 20% of its period would make that same pulse appear wider. Therefore, using this approximation, it was possible to artificially lower σ_{TOA} for each pulsar. Using 2% of the pulse period represented an optimistic value that would produce lower σ_{TOA}'s whereas 20% yielded very conservative (i.e., higher and less accurate) σ_{TOA} values.

To calculate *HWHM* for this simulation, the assumptions listed above were used to derive the equation [38, 43]:

$$HWHM = X\% \frac{(PulsePeriod)}{2} \qquad (3.25)$$

where

X represents a percentage that ranges between 2% and 20%
$PulsePeriod$ is the characteristic period of each pulsar listed in Table 3.4

As a starting point for the simulation, a nominal value of 10% was used to calculate the $HWHM$ value for each σ_{TOA}. A value of 1μs was chosen for σ_γ. This number was chosen based on research conducted of current operational x-ray detectors [25, 38, 39]. $HWHM^*$ (as described in Section 2.5.4) was calculated by summing the $HWHM$ and σ_γ in quadrature. The area and time components of S and B from Equation (2.23) and Equation (2.24) were given a range of values to vary the overall σ_{TOA} values.

Based on the pulse period and flux attributes, which are characteristic of each pulsar, every pulsar was assigned a unique σ_{TOA}. Each time a TOA was calculated between a satellite and a particular pulsar, the pulsar's particular σ_{TOA} was used to compute a randomly generated pulsar measurement error for each satellite:

$$\alpha = \sigma_{TOA}(X) \tag{3.26}$$

where X represents a randomly selected number with a mean of 0 and a variance of 1.

In each TOA observation, the simulation assigned a randomly generated pulsar measurement error for each involved satellite. The randomness ensured that no two TOAs exactly duplicated themselves from two different satellites. The TDOA measurement noise term was then calculated by adding the two satellite generated pulsar measurement errors together. The TDOA measurement noise term can be expressed as:

$$\nu = \alpha_i + \alpha_j \tag{3.27}$$

where

α represents the satellite generated pulsar measurement error measured in units of time

i is the index for satellite 1, the primary satellite in each TDOA observation

j is the index for satellite 2, the secondary satellite in each TDOA observation

Finally, ν, measured in seconds, was added to the perfect TDOA equation (Equation (3.24)) for each generated TDOA.

3.4.3   A3 Block Output.   The final TDOA equation, which accounts for clock bias and measurement noise can be expressed as:

$$TDOA_{i-j} = (\vec{r}_i - \vec{r}_j) \cdot \hat{n} + c(\delta t_i - \delta t_j) + c\nu \qquad (3.28)$$

where c represents the speed of light used to scale the bias and noise terms as distances.

Block A3 output TDOA distances calculated for all visible pulsar-satellite-pair events at each time step. These observations were passed into the batch filter to be used in the residuals calculations.

3.5   Batch Filter(A4)

In order to accomplish the research objectives, block A4 was designed to handle three different types of estimation scenarios

- Estimation of initial epoch states using pseudoranges only

- Estimation of the initial epoch states using both pseudoranges and TDOAs

- Estimation of the initial epoch states during pseudorange blackouts using TDOA-only observation intervals

The purpose of block A4 is to calculate corrections to the approximations of the GPS satellite initial states at epoch. In an operational setting, the true epoch state will never be precisely known. Therefore, in order to simulate our ignorance of the true state, the initial ECEF states of each GPS satellite had to be "corrupted." Ideally, the filter estimated corrections for each GPS satellite state vector should align the corrupted state values to the true epoch state values.

The first operation of A4 was to load in the initial states of the GPS constellation calculated in A1 and subsequently randomly offset each component of the initial state vector from its corresponding truth value. Table 3.5 lists each component of the state vector and the 1σ to offset its value from truth.

Table 3.5:   Corrupted state vector generation

State Component	1σ Offset
x	3m
y	3m
z	3m
$\dot{x}$	0.01 m/sec
$\dot{y}$	0.01 m/sec
$\dot{z}$	0.01 m/sec
bias	3 m
drift	.03 m/15 min

Next, the simulated operational pseudoranges from A2 and the simulated real world TDOAs from block A3 were input into A4. A successful batch filter would use the pseudoranges and/or TDOAs to differentially correct or improve the initial "corrupted" estimates of the true epoch states so that they approached the true epoch state vector values [50]. In order to accomplish its estimate of truth, the simulation batch filter used the following equation based on the concepts developed in Section 2.3.

$$\delta x(t_0) = (T^T W T)^{-1}(T^T W \vec{r}) \qquad (3.29)$$

The value of $\delta x(t_0)$, which represents the batch filter's correction to the original estimate of the state vector, was used in an iteration scheme to compute the final best estimate of the GPS satellite state vectors. Equation (3.29) was used to differentially correct the original estimate of the GPS satellite state vectors in order to align them with the truth model state vectors in the following equation

$$\tilde{x}(t_0) = \bar{x}(t_0) + \delta x(t_0) \qquad (3.30)$$

where

$\tilde{x}(t_0)$ is the current best estimate of the state vector based on the corrections to the previous estimate

$\bar{x}(t_0)$ is the previous estimate of the state vector

The following sections will outline how the components of Equation (3.29) were calculated in order to compute the best estimate of the GPS satellite state vectors. First, the concept of clock estimation will be outlined. Next, calculation of the T, W, and r matrices will be treated for each basic type of observation - pseudorange and TDOA.

3.5.1 Clock Error Estimation Model. The output of the atomic frequency standard can be written as

$$T(t) = t + \delta(t) \tag{3.31}$$

where

$T(t)$ is the clock output time
t is the true clock output time
$\delta(t)$ is the clock error

The ideal atomic clock would forever remain stable and output the true time (t) with no error. However, no clock is perfect. The ability of a clock to keep time is related to its frequency stability. The $\delta(t)$ term, which is used to model and approximate clock truth model error, can itself be written as an equation [30]

$$\delta(t_1) = \Delta t(t_0) + \frac{\Delta f}{f_0}(t_1 - t_0) + \frac{\dot{f}}{2f_0}(t_1 - t_0)^2 + \int_{t_0}^{t_1} \frac{\tilde{f}(t)}{f_0} dt \tag{3.32}$$

where

t_0 is the epoch time
t_1 is the final time
Δt is the time error (bias)

3-28

f_0 is the true frequency of the source. Each frequency term is divided by this value to create a normalized or relative term

Δf is the frequency deviation of the clock from its specified value $(f - f_0)$ where f is the actual frequency of the clock

$\dot{f}$ is the frequency drift

$\tilde{f}(t)$ is the random frequency error

The first three terms in Equation (3.32) represent systematic effects that are estimated by comparing the clock with a reference clock. The last term represents a random clock performance effect and is characterized by its variance [30].

In order for the MCS to maintain precise synchronization of the clocks aboard the satellites, it is essential that $\delta(t)$ be modeled to accurately simulate the errors of the clock's true frequency behavior. The MCS determines the error in each satellite clock on the basis of pseudorange measurements from the monitor stations [30]. The error of each satellite clock can be written as

$$\delta(t)^s = t^s - t_{GPS} \tag{3.33}$$

where

$\delta(t)^s$ is the clock error for satellite s

t^s is the time kept by the clock for satellite s

t_{GPS} is GPS time. GPS time is determined by estimating all the clocks in the GPS system together as an ensemble by treating no individual clock as the master

The clock error, $(\delta(t)^s)$, for each satellite is modeled as a quadratic function over a time interval

$$\delta(t)^s = af_0 + af_1(t_{GPS} - t_{0c}) + af_2(t_{GPS} - t_{0c})^2 + \eta(t) \tag{3.34}$$

where

t_{0c} is the reference epoch time for the generation of the clock error model

af_0 is the clock offset (clock bias) in seconds

af_1 is the fractional frequency offset (clock drift) in seconds/second

af_2 is the fractional frequency drift (clock drift rate) in seconds/second^2

$\eta(t)$ represents the random frequency error

The clock error correction terms (af_0, af_1, and af_2) represent numerical coefficients of the quadratic function used to model the clock error in Equation (3.31). These correction terms are regularly uploaded to each GPS satellite by the OCS and are broadcast to GPS users as part of the navigation message to help correct for each satellite's inherent clock bias. Proper correction terms keep the satellite clocks synchronized with GPS time to within 5 – 10 ns [30]. The best fit line drawn through the plot in Figure 3.2 depicts a quadratic best fit of the clock's performance using the af_0, af_1, and af_2 correction terms. It is immediately obvious that Equation (3.34) is related to Equation (3.32). The terms of Equation (3.34) and Equation (3.32) can be exactly equated so that we can write

$$af_0 = \Delta t(t) \tag{3.35}$$

$$af_1 = \frac{\Delta f}{f_0} \tag{3.36}$$

$$af_2 = \frac{\dot{f}}{2f_0} \tag{3.37}$$

$$\eta(t) = \int_{t_0}^{t_1} \frac{\tilde{f}(t)}{f_0} dt \tag{3.38}$$

This simulation will use the clock correction terms to simulate the bias of each satellite and monitor station. The $\eta(t)$ term also represents the relativistic corrections. However, because this term is deterministic, this simulation will assume that it has been corrected for.

Finally, it is important to note that two assumptions were made concerning the estimation of the clocks for the GPS system. First, of the three clock terms to estimate in Equation (3.34), only af_0 and af_1 were estimated in the filter. The quadratic drift

rate term, af_2, which is on the order of 10^{-45}, was found to have a negligible effect on the the linearity of the $[af_0 + af_1(t_{GPS} - t_{0c})]$ part of Equation (3.34) for the time periods in question (1 day or less). Secondly, the ground station clocks were not estimated in the filter (the ground station clock errors were assumed to be perfectly known). Only the satellite clocks were estimated in the batch filter.

3.5.2   T Matrix.   This simulation computed the position and velocity components of the T matrix numerically as an approximation to the analytical solution in Equation (2.10)

$$
\begin{aligned}
T &= \frac{\partial observations}{\partial X_0} \\
&= \frac{\partial observations}{\partial X} \frac{\partial X}{\partial X_0} \\
&= H\Phi
\end{aligned}
$$

(3.39)

where

X is the current state vector

X_0 is state vector at epoch

$\frac{\partial observations}{\partial X}$ is equal to H the observation partial derivative matrix

$\frac{\partial X}{\partial X_0}$ is equal to Φ the state transition matrix

Analytically, H is calculated using Equation (2.9). As stated in Chapter 2, the G function describes the measured data in terms of the states of the reference trajectory x_{ref} [52].

$$z_j = G(x_{ref}) + \varepsilon \tag{3.40}$$

where

z_j is the measurement used to obtain an estimate of the satellites' state and j

is the number of available measurements

$G(x)$ is the measured data function described in Equation (2.8)

This simulation used two different types of measurements in the numerical computation of the T corresponding to the two different types of observations:

$$z_1 = \rho = \sqrt{(x_{sat} - x_{G/S})^2 + (y_{sat} - y_{G/S})^2 + (z_{sat} - z_{G/S})^2} + c(\delta t_{G/S} - \delta t_{sat}) + \varepsilon$$
(3.41)

$$z_2 = TDOA_{i-j} = (\vec{r_i} - \vec{r_j}) \cdot \hat{n} + c(\delta t_i - \delta t_j) + \varepsilon$$
(3.42)

where ε is the zero-mean random process such that $\mathrm{E}[\varepsilon] = 0$ [34].

For each measurement z_j, ε represents the uncertainty in each measurement. For the pseudoranges, ε is representative of the tropospheric, multipath, and receiver measurement errors outlined in Section 3.3. For the TDOA measurements, ε represents the σ_{TOA} term explained in Section 3.4.

As presented in Chapter 2, if T were to be calculated analytically, each row of the H matrix, which corresponds to a separate observation, would be multiplied by a corresponding Φ matrix to map the observations to the epoch time. However, in this simulation, the position and velocity elements of T were numerically approximated in one calculation. Symbolically, the T matrix takes the form of:

$$T_{n,m} = \begin{bmatrix} A_{1,1} & A_{1,2} & A_{1,3} & A_{1,4} & A_{1,5} & A_{1,6} & A_{1,7} & A_{1,8} \\ B_{1,1} & B_{1,2} & B_{1,3} & B_{1,4} & B_{1,5} & B_{1,6} & B_{1,7} & B_{1,8} \end{bmatrix}$$
(3.43)

$$A_{1,1} = \frac{\partial TDOA_i}{\partial x_0} \qquad B_{1,1} = \frac{\partial Pseudorange_i}{\partial x_0}$$

$$A_{1,2} = \frac{\partial TDOA_i}{\partial y_0} \qquad B_{1,2} = \frac{\partial Pseudorange_i}{\partial y_0}$$

$$A_{1,3} = \frac{\partial TDOA_i}{\partial z_0} \qquad B_{1,3} = \frac{\partial Pseudorange_i}{\partial z_0}$$

$$A_{1,4} = \frac{\partial TDOA_i}{\partial \dot{x}_0} \qquad B_{1,4} = \frac{\partial Pseudorange_i}{\partial \dot{x}_0}$$

$$A_{1,5} = \frac{\partial TDOA_i}{\partial \dot{y}_0} \qquad B_{1,5} = \frac{\partial Pseudorange_i}{\partial \dot{y}_0}$$

$$A_{1,6} = \frac{\partial TDOA_i}{\partial \dot{z}_0} \qquad B_{1,6} = \frac{\partial Pseudorange_i}{\partial \dot{z}_0}$$

$$A_{1,7} = \frac{\partial TDOA_i}{\partial bias} \qquad B_{1,7} = \frac{\partial Pseudorange_i}{\partial bias}$$

$$A_{1,8} = \frac{\partial TDOA_i}{\partial drift} \qquad B_{1,8} = \frac{\partial Pseudorange_i}{\partial drift}$$

where

n is the number of observations corresponding to the number of rows of T

m is the number of states to be estimated corresponding to the number of columns of T

i is the index from 0 to N of the number of available TDOA observations

j is the index from 0 to N of the number of available pseudorange observations

In actuality, Equation (3.43) represents the partial derivative components for only one satellite in the GPS constellation. The simulation's T matrix contained n rows corresponding to each observation and up to 232 columns (8 states by 29 satellites). Each satellite's state vector was assigned a column for each row of T. For example, satellite 1's partial derivatives spanned from columns 1 to 8; satellite 29's partial derivative elements spanned from columns 225 to 232. In the larger T matrix, each row took the form:

$$T = \left[satellite1 | satellite2 | \cdots | satelliteN \right] \qquad (3.44)$$

where

3-33

satellite $1 \cdots$ satellite N represents one of the partial derivative sets ($A_{n,1} \cdots A_{n,8}$ or $B_{n,1} \cdots B_{n,8}$) of Equation (3.43) depending on if the satellite was involved in a pseudorange or TDOA.

For each row of T, the only elements populated with nonzero partial derivative values were for satellites involved in the observation. For example, if row 1 represents a pseudorange involving satellite 1, then only the first 8 columns of row 1 would be populated with nonzero elements. If row 2 represented a TDOA between satellites 1 and 3 then only columns 1 through 8 and 17 through 24 would be populated with nonzero elements.

To calculate each position and velocity element of T, a numerical method called finite differencing was used. A brief explanation of finite differencing will be presented here. A more thorough treatment of this topic can be found in [50]. Finite differencing approximates the partial derivatives of T by calculating the effects that making small changes in each component of the state vector (e.g., x, y, and z) has on the system. Equation (3.39) dictates that these small changes to the state vector components at epoch be made at the epoch time.

Each position and velocity T element was computed in the simulation by first propagating the state vector components forward in time to each observation time. The trajectory that resulted from this propagation was known as the nominal trajectory.

For each component of the state vector, the nominal state trajectory was perturbed by some value then propagated again. This trajectory was called the perturbed trajectory. For the state components x, y, and z, which were in units of meters, a perturbation of .05 m was chosen. For the state components $\dot{x}$, $\dot{y}$, and $\dot{z}$, which were expressed in units of m/s, a perturbation of .001 m/s was chosen. The perturbation values were empirically chosen to be large enough that an actual change in the trajectory could be calculated for the partial derivative, but small enough that the linearity assumption of the partial derivative was still valid.

3-34

Therefore, each numerical partial derivative was represented as one of two equations depending on if the state component was a position or velocity component:

$$\frac{\partial observations}{\partial X_0} = \frac{Obs_{perturbed} - Obs_{nominal}}{\delta position} \tag{3.45}$$

$$\frac{\partial observations}{\partial X_0} = \frac{Obs_{perturbed} - Obs_{nominal}}{\delta velocity} \tag{3.46}$$

where

Obs is either a TDOA or pseudorange

$\delta position$ is equal to .05 m. It represents the small change in position used to calculate the partial derivative.

$\delta velocity$ is equal to .001 m/s. It represents the small change in velocity used to calculate the partial derivative.

The nominal and perturbed trajectories were propagated with no simulated random errors. The ε terms from Equations (3.41) and (3.42), which represented the observations' random errors, were estimated by the filter.

3.5.2.1   Pseudorange Partial Derivatives.   Each pseudorange contained a single partial derivative corresponding to the one satellite involved in the measurement whose states were being estimated. Figure 3.7 depicts the calculation of Equations (3.45) and (3.46) for pseudorange observations. As described above, the simulation only calculated the partial derivatives of the satellite involved in each pseudorange, because only the satellite's states were being estimated by the filter.

Contrary to the position and velocity components, the partial derivatives calculated with respect to the clock components of the state vector were computed analytically for pseudorange contributions to the T matrix. Using Equation (3.41), the partial derivatives of the H matrix for the bias and drift were calculated:

$$\frac{\partial G(x)}{\partial bias} = -1 \tag{3.47}$$

$$\frac{\partial G(x)}{\partial drift} = 0 \qquad (3.48)$$

Using the two-state (bias and drift) derivative of the Φ matrix in Equation (3.16), the clock components of T were analytically computed using Equation (2.10)

$$T = \begin{bmatrix} -1 & 0 \end{bmatrix} \begin{bmatrix} 1 & \tau \\ 0 & 1 \end{bmatrix}$$
$$= \begin{bmatrix} -1 & \tau \end{bmatrix}$$

$$(3.49)$$

where

$\tau = t_{k+1}\text{-}t_k$, the time interval

3.5.2.2 TDOA Partial Derivatives.

Each TDOA was composed of two separate partial derivatives corresponding to the two satellites involved in the observation whose state components were both being estimated. Figure 3.8 illustrates the TDOA-based partial derivative of Equations (3.45) and (3.46). The TDOA partial derivatives involved a primary and secondary satellite as shown in Figure 3.8. In this simulation, the primary satellite was considered the satellite that received the pulsar signal TOA before its secondary counterpart satellite. The primary satellite was considered the reference satellite and thus all calculated TDOAs from the perspective of the secondary satellite had opposite signs of the TDOAs that were computed from the perspective of the primary satellite.

In Figure 3.8, satellite 1 is considered the primary receiver and satellite 2, the secondary receiver. Conceptually, the numerical partial derivatives of satellite 1 involved making successively small changes to each of satellite 1's position and velocity state vector components while keeping the state vector components of satellite 2 con-
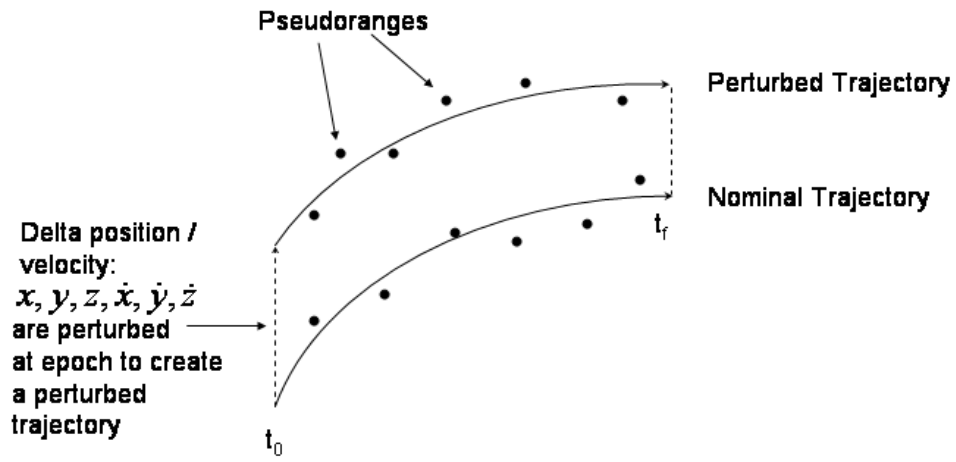
$$\frac{\partial pseudorange}{\partial x, \partial y, \partial z} \cong \frac{\Delta pseudorange}{\Delta x, \Delta y, \Delta z} = \frac{pseudorange_{perturbed} - pseudorange_{nominal}}{Delta\_position}$$

$$\frac{\partial pseudorange}{\partial \dot{x}, \partial \dot{y}, \partial \dot{z}} \cong \frac{\Delta pseudorange}{\Delta \dot{x}, \Delta \dot{y}, \Delta \dot{z}} = \frac{pseudorange_{perturbed} - pseudorange_{nominal}}{Delta\_velocity}$$

Figure 3.7:   Illustration of Pseudorange Observation Numerical Partial Derivatives

$\hat{n}_{pulsar}$

Nominal TDOA

Satellite 1   Satellite 2

Primary Satellite
Perturbed TDOA

Δx_{sat1}

Satellite 1

Satellite 2

Secondary Satellite
Perturbed TDOA

Δx_{sat2}

Satellite 1

Satellite 2

Primary Satellite TDOA Partial Derivative

$$\frac{\partial TDOA_{1-2}}{\partial x_1} \cong \frac{TDOA_{1-2\,perturbed} - TDOA_{1-2\,nominal}}{\Delta x_{sat1}}$$

Secondary Satellite TDOA Partial Derivative

$$\frac{\partial TDOA_{2-1}}{\partial x_2} \cong \frac{-\left(TDOA_{2-1\,perturbed} - TDOA_{2-1\,nominal}\right)}{\Delta x_{sat2}}$$
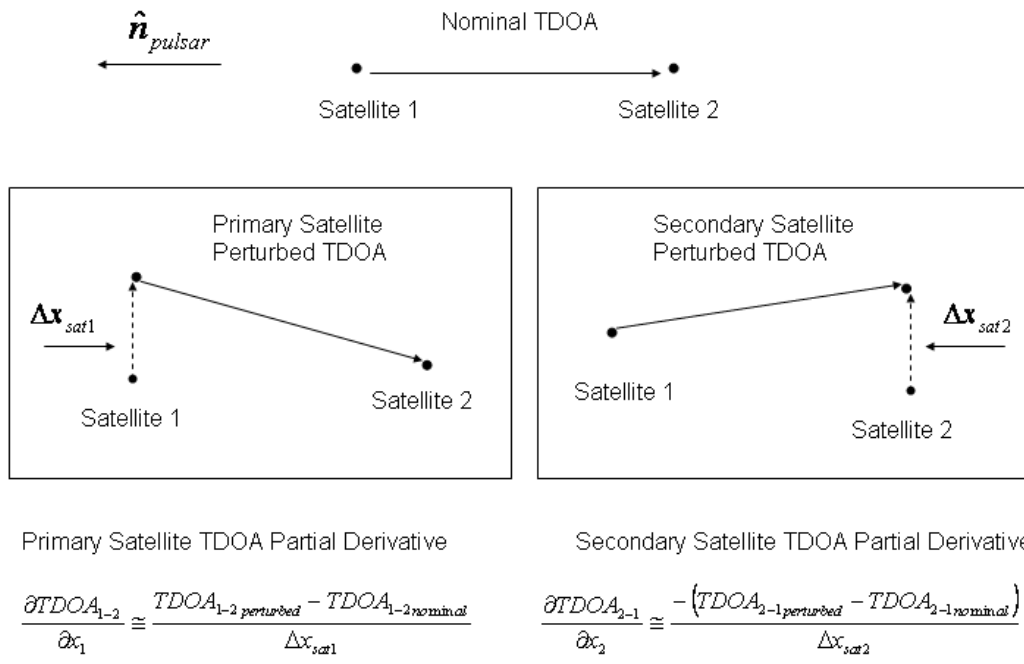
Figure 3.8:   Illustration of TDOA Observation Numerical Partial Derivatives

stant. By observing the effect of satellite 1's changes on the TDOA computation between satellites 1 and 2 (TDOA$_{1-2}$), the numerical partial derivatives for the primary receiver could be calculated.

Analogously, the secondary partial derivatives were conceptually calculated by perturbing each of satellite 2's position and velocity state vector components and noting their effect on the TDOA calculations while keeping satellite 1's state vector constant. These partial derivatives were based on TDOA$_{2-1}$ and were given a sign opposite of the primary partial derivatives, because they are referenced from the opposing perspective of the primary satellite.

In the simulation, the x, y, z, $\dot{x}$, $\dot{y}$, and $\dot{z}$ components were perturbed at epoch in accordance with Equation (3.39) then the perturbed trajectories were propagated. Subsequently, new TDOAs between satellites 1 and 2 were calculated using state vector information from the perturbed state vector. Finally, the TDOAs resulting from the perturbed trajectories were differenced from the nominally (unperturbed) calculated TDOA values for the calculation of the actual partial derivatives.

The clock partial derivatives for the TDOA-based portion of the T matrix were calculated analytically in a manner similar to the methods described above for the pseudoranges. Additionally, the assumption of opposite signs for the primary versus secondary partial derivatives was also used to compute the partial derivatives of the bias and drift at epoch with respect to the TDOA's. Using Equation (3.42), the primary satellite partial derivatives of the H matrix for the bias and drift were calculated:

$$\frac{\partial G(x)}{\partial bias} = 1 \tag{3.50}$$

$$\frac{\partial G(x)}{\partial drift} = 0 \tag{3.51}$$

The two-state Φ matrix was used to calculate the T matrix partials:

$$T = \begin{bmatrix} -1 & 0 \end{bmatrix} \begin{bmatrix} 1 & \tau \\ 0 & 1 \end{bmatrix}$$

$$= \begin{bmatrix} 1 & \tau \end{bmatrix}$$

$$(3.52)$$

Using the secondary satellite opposite sign assumption, the clock partial derivative components of the T matrix for satellite 2 could be calculated:

$$T = \begin{bmatrix} -1 & -\tau \end{bmatrix} \qquad (3.53)$$

An important simplifying assumption that was made during the generation of the T matrix is the principle of linear independence of the measurements. Figure 3.9 illustrates a possible scenario of 4 satellites involved in a set of TDOAs using 1 pulsar. If satellite 1 was considered the primary satellite, then a set of TDOAs can be generated between satellites 1, 2, 3, and 4 (1-2, 1-3, and 1-4). All other possible TDOAs (e.g., 2-3) were not calculated, because those observations are linear combinations of measurements 1-2, 1-3, and 1-4. For example, $TDOA_{2-3}$ could be calculated as a linear combination of $TDOA_{1-2}$ and $TDOA_{1-3}$. Essentially these TDOAs offered no new information that could not already be derived from the first set of TDOAs. Only the set of linearly independent measurements were incorporated into the T matrix. In the event that satellite 1 did not detect a particular pulsar, the TDOA calculation algorithm would use the next satellite (satellite 2) as the primary and begin the same calculations.

3.5.3 W Matrix. Using the ε terms of Equation (3.41) and (3.42), the weighting matrix for the batch filter was computed. First, the measurement noise covariance matrix, R, was calculated. To calculate the elements of R, an assumption was made that both the pseudorange observations and TDOAs were all independent

4-Satellite TDOA Observation Scheme

Primary Satellite	Secondary Satellite
1	2
	3
	4
2	3
	4
3	4

Figure 3.9:   Redundant TDOA Observations Table (4 satellite case). TDOAs 2-3, 2-4, and 3-4 are redundant since TDOAs 1-2, 1-3, and 1-4 are available.

measurements. For the pseudoranges, measurement independence makes intuitive sense because one pseudorange measurement between a satellite and ground station cannot be affected by a second satellite or ground station. In the case of the TDOAs, it was assumed in the simulation that for every TDOA calculated, independent TOAs to a given pulsar were calculated by each satellite. Furthermore, for each individual satellite, it was assumed that the satellite did not carry the same TOA measurement error for any given observation. Instead, it was assumed that a satellite generated a new TOA measurement error for each TDOA. Using these observation assumptions, each element of the R matrix was computed using the following equations:

$$R_{i,i} = E\left[\varepsilon\varepsilon\right] = \sigma^2_{TDOA,PR} \tag{3.54}$$

$$\sigma_{TDOA} = c\sqrt{(\sigma^2_{TOA1} + \sigma^2_{TOA2})} \tag{3.55}$$

$$\sigma_{PR} = c\sqrt{(\sigma^2_{tropo} + \sigma^2_{multipath} + \sigma^2_{noise})} \tag{3.56}$$

3-41

where

σ_{TDOA} is the variance of the TDOA measurement noise
σ_{PR} is the variance of the pseudorange measurement noise
c is the speed of light

Measurement independence means that there is no correlation of measurement errors and thus R was a diagonal matrix. The R matrix took the form

$$R = \begin{bmatrix} R_{TDOA} & 0 \\ 0 & R_{PR} \end{bmatrix} \tag{3.57}$$

where

$$R_{TDOA} = \begin{bmatrix} \sigma_{TDOA_1} & & 0 \\ & \ddots & \\ 0 & & \sigma_{TDOA_N} \end{bmatrix} \tag{3.58}$$

$$R_{PR} = \begin{bmatrix} \sigma_{PR_1} & & 0 \\ & \ddots & \\ 0 & & \sigma_{PR_N} \end{bmatrix} \tag{3.59}$$

where

R_{TDOA} represents the matrix of diagonal σ_{TDOA}^2 terms
R_{PR} represents the matrix of diagonal σ_{PR}^2 terms
$\sigma_{TDOA_{1...N}}$ represents a block of diagonal terms equal to the number of TDOA measurements for the time interval
$\sigma_{PR_{1...N}}$ represents a block of diagonal terms equal to the number of pseudorange measurements for the time interval
0 represents a block of elements equal to 0 above and below the matrix diagonal

The weighting matrix W was simply calculated by inverting the R matrix. Thus the diagonal elements of R were inverted:

$$W = R^{-1} = \begin{bmatrix} R_{TDOA}^{-1} & 0 \\ 0 & R_{PR}^{-1} \end{bmatrix} \qquad (3.60)$$

where

$$R_{TDOA}^{-1} = \begin{bmatrix} \frac{1}{\sigma_{TDOA_1}^2} & & 0 \\ & \ddots & \\ 0 & & \frac{1}{\sigma_{TDOA_N}^2} \end{bmatrix} \qquad (3.61)$$

$$R_{PR}^{-1} = \begin{bmatrix} \frac{1}{\sigma_{PR_1}^2} & & 0 \\ & \ddots & \\ 0 & & \frac{1}{\sigma_{PR_N}^2} \end{bmatrix} \qquad (3.62)$$

Note that in reality, there is a correlation between TDOA measurements at a given epoch, because they all share the same base satellite. This will lead to cross-correlation terms in the covariance matrix. These cross-correlations were not accounted for in the current simulation. Implementing them is a recommendation for future work.

3.5.4   Residuals Matrix.   The residuals matrix was calculated by subtracting all of the operational pseudorange and TDOA observations garnered from A2 and A3 respectively from the corresponding calculated pseudorange and TDOA quantities from the $G(x)$ terms in Equations (3.41) and (3.42).

$$
r = \begin{bmatrix} TDOA_{calc}1 - TDOA_{obs}1 \\ TDOA_{calc}2 - TDOA_{obs}2 \\ \vdots \\ TDOA_{calc}N - TDOA_{obs}N \\ PR_{calc}1 - PR_{obs}1 \\ PR_{calc}2 - PR_{obs}2 \\ \vdots \\ PR_{calc}N - PR_{obs}N \end{bmatrix} \tag{3.63}
$$

Using the residuals matrix as the foundation, the convergence of the batch filter was determined using the following equations taken from [50]:

$$
RMS = \sqrt{\frac{r^T W r}{N}} \tag{3.64}
$$

$$
\left| RMS_{old} - RMS_{new} \right| \leq \epsilon \tag{3.65}
$$

where

r is the residuals matrix

W is the weighting matrix

N is equal to the number of total observations in the time interval

ϵ is the tolerance level representing the successive changes of the RMS of the residuals from one iteration to the next (a value of .9 was used)

RMS_{old} is the root mean square of the residuals matrix from the previous iteration

RMS_{new} is the root mean square of the residuals matrix in the current iteration

In this simulation, the batch filter stopped its iterations when the RMS of the residuals stopped changing within a tolerance (ϵ) of .9 m. The value of ϵ was chosen as an engineering tradeoff between reasonable algorithm processing time and accuracy.

3.6   Evaluate Results(A5)

The A5 block took the output of A1, the truth model epoch state vectors for the GPS constellation, and compared them with the estimated epoch state vector outputs of block A4, the batch filter. Various metrics such as the SISRE, were used to determine how well the batch filter's estimate of the state vectors agreed with the propagated truth model state vectors. Block A5 used a series of simulation test cases, called scenarios, as tools to determine results such as the SISRE. An analysis of this comparative study will be covered in Chapter 4.

3.7   Summary

This chapter mathematically developed the concepts fundamental to the simulation algorithms. The architecture of the simulation, which was divided into 5 function blocks, was broken down and discussed function-by-function. Any modeling assumptions and approximations made were introduced according to their corresponding function block. Chapter 4 will present the results and analysis of this simulation.

IV. TDOA Results and Analysis

This chapter presents and analyzes the results from scenarios used to answer the questions posed by the research objectives. The results of each scenario run, as they apply to the research objectives, will be presented in the following sections.

The introduction, presented in Section 4.1, will first discuss the specific SISRE metrics used to quantify the accuracy of the state vector estimation for each scenario run. Additionally, the concept of state vector estimate covariance will be introduced. Next, the initial conditions used to set up each scenario as well as the modeling assumptions general to all scenarios will then be discussed. Finally, the general structure of a typical scenario will be described in detail. Section 4.2 will present the techniques used to validate the proper operation and accuracy of the batch filter.

Analysis for this research will be encompassed in four separate tests. Section 4.3 will present the results and analysis for Test 1 whose purpose will be to determine if pulsar-based TDOAs will generally help to decrease the pseudorange(PR)-based SISREs for the GPS constellation. Section 4.4 will present the results and analysis of Test 2 wherein a parametric study will be conducted to determine if the number of pulsars used to create TDOA observations can significantly affect SISRE levels. Section 4.5 will present the results and analysis of Test 3 whose goal will be to determine if TDOAs can help maintain SISRE levels in the event of a ground station outage. Finally, Section 4.6 will present the results and analysis of Test 4 whose goal will be to determine if there is an optimal geometry for TDOA receivers to be situated in order to lower SISRE levels of the GPS constellation.

4.1 Introduction

4.1.1 SISRE Metrics.   Central to the analysis of this research was the SISRE metric. Conceptually presented in Chapter 2, the SISRE was used in 2 forms to determine the batch filter's ability to estimate clock and ephemeris errors. This research used two forms of SISRE to conduct scenario analysis. The first variant of

SISRE, called SISRE$_{satellite}$, quantified the errors of each individual satellite separate from its constellation counterparts.

$$SISRE_{satellite} = \sqrt{(R - CLK)^2 + \frac{1}{49}(A^2 + C^2)} \tag{4.1}$$

The second form of SISRE used for the analysis was called SISRE$_{constellation}$. SISRE$_{constellation}$ quantified the SISRE errors of all satellites together in a *RMS* sense. SISRE$_{constellation}$ was used to yield an overall average measure of how well TDOAs improved the estimation of the satellite state vectors.

$$SISRE_{constellation} = \sqrt{\frac{SISRE^2_{satellite1} + SISRE^2_{satellite2} + \cdots + SISRE^2_{satelliteN}}{N}}$$
$$\tag{4.2}$$

where N is the number of satellites in the constellation.

It is important to note that the SISRE values presented in subsequent sections were generated using a simulation that incorporated no model errors in the satellite dynamics or batch filter. Therefore, all SISRE values were inherently lower than the operational SISRE's that would be calculated by the MCS in Colorado Springs, CO. However, this research is primarily concerned with relative SISRE values and not absolute ones. The analysis presented here will determine how much a SISRE value that is generated using only pseudorange observations can be lowered if TDOAs are introduced into the estimation problem. The analysis depended less on how well the SISREs generated by the simulation agreed with operational data and more on quantification of the decrease in *relative* SISRE.

4.1.2 Covariance of the Estimate at Epoch . The state covariance matrix, P, introduced in Section 2.3 by Equations (2.11) and (2.12), was calculated in this simulation for the estimate of the state at epoch. In order to directly relate the covariance of the estimate in the ECI frame for several of the scenarios, the ECEF-

based covariance, P_{ECEF}, was transformed to the ECI frame. For each satellite, a 4-state covariance matrix was calculated. The four states included the position vector (x, y, z) and the clock bias. P_{ECEF} is expressed as

$$P_{ECEF} = \begin{bmatrix} \sigma_x^2 & \sigma_{x,y} & \sigma_{x,z} & \sigma_{x,bias} \\ \sigma_{y,x} & \sigma_y^2 & \sigma_{y,z} & \sigma_{y,bias} \\ \sigma_{z,x} & \sigma_{z,y} & \sigma_z^2 & \sigma_{z,bias} \\ \sigma_{bias,x} & \sigma_{bias,y} & \sigma_{bias,z} & \sigma_{bias}^2 \end{bmatrix} \tag{4.3}$$

where

the σ_n^2 terms represent the variances of the estimate; $n = x, y, z, bias$
the $\sigma_{n,m}$ terms represent the covariances of the estimate; $m = x, y, z, bias$

In order to express the covariance in the ECI frame, the ECEF states, along with the clock bias, must be rotated for each satellite using the equation

$$\begin{bmatrix} X_{ECI} \\ X_{CLK} \end{bmatrix} = \begin{bmatrix} C_{ECEF}^{ECI} & 0 \\ 0 & 1 \end{bmatrix} \begin{bmatrix} X_{ECEF} \\ X_{CLK} \end{bmatrix} \tag{4.4}$$

where

X_{ECI} represents the state vector expressed in the ECI frame
X_{CLK} represents the clock bias
X_{ECEF} represents the state vector expressed in the ECEF frame
C_{ECEF}^{ECI} represents the direction cosine matrix that transforms the state components of the ECEF frame to the ECI frame

Correspondingly, the covariance expressed in the ECEF frame can be transformed into the ECI frame

$$P_{ECI} = C P_{ECEF} C^T \tag{4.5}$$

where

$$C = \begin{bmatrix} C_{ECEF}^{ECI} & 0 \\ 0 & 1 \end{bmatrix} \qquad (4.6)$$

where C represents the combined direction cosine matrix that transforms both the ECEF-based components and the clock component to the ECI frame.

Finally, P_{ECI} can be written as

$$P_{ECI} = \begin{bmatrix} \sigma_X^2 & \sigma_{X,Y} & \sigma_{X,Z} & \sigma_{X,bias} \\ \sigma_{Y,X} & \sigma_Y^2 & \sigma_{Y,Z} & \sigma_{Y,bias} \\ \sigma_{Z,X} & \sigma_{Z,Y} & \sigma_Z^2 & \sigma_{Z,bias} \\ \sigma_{bias,X} & \sigma_{bias,Y} & \sigma_{bias,Z} & \sigma_{bias}^2 \end{bmatrix} \qquad (4.7)$$

where

X is the ECI based X-component of the covariance matrix
Y is the ECI based Y-component of the covariance matrix
Z is the ECI based Z-component covariance matrix

For each satellite, the covariance of the estimate, $\sigma_{satellite}$, was calculated by computing the trace (sum of the diagonal elements) of each satellite's P_{ECEF} matrix.

$$\sigma_{satellite} = \sqrt{Trace(P_{ECEF})} \qquad (4.8)$$

It is recognized that the eigenvalues of the covariance matrix, P, are invariant to the coordinate frame, and therefore the covariance of the estimate is equivalent in the ECI and ECEF frames. However, the P matrices were transformed to the ECI frame in order to relate them more directly with the ECI positions of the pulsars for certain scenarios discussed below.

Using the individual $\sigma_{satellite}$ values, a constellation covariance estimate, $\sigma_{constellation}$, was also computed by calculating the RMS of all 29 $\sigma_{satellite}$ values.

$$\sigma_{constellation} = \sqrt{\frac{\sigma_{satellite1}^2 + \sigma_{satellite2}^2 + \cdots + \sigma_{satelliteN}^2}{N}} \qquad (4.9)$$

where N is the number of satellites in the constellation.

Throughout this chapter, the $\sigma_{constellation}$ values will be compared to the results of each test introduced above. The covariance estimates are independent of any specific random errors that were introduced into the measurements of each scenario. Therefore an attempt will be made to validate the results of specific scenarios by illustrating that the covariances should generally behave (i.e., shrink or grow) in a manner consistent to the results of a set of scenarios. That is, if a set of scenarios show that the SISRE will decrease or increase, then the comparison of the covariance matrices should also show the same trend. Note that the SISRE results also have a different "weighting" of the error components than $\sigma_{satellite}$, since the radial and clock errors are more significant than the along-track or cross-track. As a result, a direct comparison between SISRE$_{constellation}$ and $\sigma_{constellation}$ is not appropriate. Nevertheless, it is expected that the trends should be consistent.

4.1.3 Initial Conditions. Before every scenario run, the simulation implemented a set of initial conditions that remained constant for every scenario. The epoch time of the GPS constellation was determined using the initial satellite ephemerides (see Appendix A) gleaned from the GPS Yuma Almanac [23] for each satellite. The epoch time used to initialize every scenario is listed below:

- Year = 2004

- Month = 08

- Day = 14

- Hours = 19

- Minutes = 50

- Seconds = 24

Using the above mentioned epoch time, each scenario run was propagated for the same duration and used the same time step. The propagation initial conditions are listed below.

- $t_{initial} = 0$ seconds

- $t_{final} = 86400$ seconds (1 day)

- time step = 900 seconds (15 minutes)

4.1.4 Scenario Overview.   This section will describe how a typical scenario was set up to run in order to yield SISRE results for analysis. A scenario matrix will be presented which will describe the scenarios used in this simulation. Additionally, the use of the Matlab® pseudo-random number generator to compare large numbers of scenarios will be discussed.

4.1.4.1 Scenario Structure.   The architecture of each scenario was a function of the A1 - A5 algorithm blocks presented in Section 3.1.1. For each scenario the architecture of block A1, the truth model was exactly the same. The GPS constellation always consisted of 29 satellites. The initial conditions, common to each scenario and described in Section 4.1.3, were all set in A1.

In the block A2 algorithm, a boolean flag existed which allowed pseudorange (PR) observations to be turned on and off for each scenario. When PRs were turned on, the PR error parameters (as described in Section 3.3.2) could also be set. The values of these 1σ errors (i.e., troposphere, multipath, receiver error) were defined in Chapter 3.

Analogously, in block A3, a boolean flag was designed to allow TDOAs to be turned on and off. If TDOAs were activated for a scenario, the TDOA measurement error parameter (as described in Section 3.4.2) could also be turned on and off.

After the initial flags were set and various parameter values were selected, the number of pulsars had to be selected if TDOAs were being incorporated into the

scenario run. Pulsars that were not desired for use in the simulation were manually set to a very high σ_{TOA} level in order to de-weight their batch filter contributions, to a negligible level, for all TDOA measurements. The unused pulsars were not completely removed from the simulation, because that would have changed the sequencing of random numbers that were applied to the various components of the system, as described in the following section.

   4.1.4.2   Nominal TDOA Scenario.   The majority of the scenarios that incorporated TDOAs were based on a nominal TDOA scenario. This section will present the parameters and associated assumptions of the nominal TDOA scenario.

   The most important characteristic of pulsars used in the computation of TDOAs was their intrinsic time of arrival uncertainty, σ_{TOA}. Equation (2.20), which characterized the pulsar timing error used in the simulation, is restated below for clarity. The components of Equation (4.10) have been previously defined in Section 2.5.4.

$$\sigma_{TOA} \approx \frac{\sqrt{HWHM^2 + \sigma_\gamma^2}}{S/\sqrt{S+B}} \tag{4.10}$$

   Equation (4.10) was instrumental in formulating a nominal TDOA scenario. The known pulsars have a *HWHM* that can be approximated using a value that ranges from 2% to 20% of their pulse period. The *HWHM* range of values comes from the results of empirical analysis conducted at the University of Maryland [43]. In reality, as stated in Section 2.5.4, each pulsar has a naturally occurring and unique *HWHM* value that can be measured and used in Equation (4.10). However, during the course of research, it was found that the x-ray band *HWHM* for each pulsar that was listed in Table 3.4 was not readily available. The lack of pulsar pulse-width knowledge is a result of the fact that measuring the width of a pulsar pulse is not an intrinsically useful metric in pulsar physics research [38]. Additionally, the radio band based *HWHM* values that have been determined for each pulsar do not necessarily correlate the the *HWHM* measurements in the x-ray waveband [38]. Consequently,

a nominal value 10% was assigned to each pulsar in order to yield overall reasonable σ_{TOA} values for each pulsar.

As stated in Section 2.5.4, B represents the total number of all other photon events in an observation including any unpulsed emission from the pulsar source, the diffuse x-ray background, and the particle-induced background counts that arrive at the detector. Essentially, B accounts for all extraneous photon events that can corrupt a detector's measurement of the pulsar's pulsed x-ray emissions. A value of .005 was chosen based on the empirical research done at the Naval Research Laboratory (NRL) [38]. The detector σ_γ value of 1μs was also gleaned via research done at NRL [38].

It was observed that the detector area (A_{eff}) of current x-ray detectors ranged from approximately 1000 cm^2 to 6500 cm^2. Based on this research and discussions with the NRL, a nominal detector value of 3100 cm^2 was chosen [25, 38, 39]. A 3100 cm^2 detector would measure approximately 1.9 ft on one side. The frame of a Block IIR GPS satellite is a cube that measures approximately 6 ft on a side [33]. Therefore it was decided that 3100 cm^2 of effective area would be feasible for a GPS satellite. Finally, the detector integration time (Δt) of 10^3 seconds was chosen based on the specifications of previous x-ray observatories [25, 38, 39, 54].

In choosing detector specifications that will fulfill the requirements of our nominal TDOA scenario, it is important to note that the purpose of this research is not to conduct an engineering study concerning the optimal characteristics of an x-ray detector. The components of σ_{TOA} listed in Equation (4.10) are simply a means to vary the σ_{TOA} potential of each pulsar. Therefore, in the analysis that follows, several parameters (e.g., $HWHM$, area, integration time) will be varied in order to yield σ_{TOA} values of different magnitudes for each pulsar. The analysis of this chapter will focus on associating the trends of SISRE with the values of σ_{TOA} in a given scenario. Table 4.1 lists the nominal σ_{TOA} values, expressed in meters, for each pulsar. σ_{TOA}

varies for each pulsar, because the flux values (see Table 3.4), characteristic of each pulsar, directly affect the 'S' term in Equation (4.10) giving each pulsar its own σ_{TOA}.

Table 4.1:   Nominal Pulsar σ_{TOA}

Pulsar	σ_{TOA} (m)
B0531+21 (Crab Pulsar)	88.5
J0437-4715	6782.0
B1821-24	2764.7
J2124-3358	2.906E4
J1012+5307	2.027E5
J0218+4232	1.314E4
J0751+1807	3.919E4
B1937+21	4.149E4
B1257+12	2.729E5
B1820-30A	42.22
B1620-26	5.343E4
J2322+20	3.858E5
J2019+24	1.06E5
J0030+0451	1.873E4
J1024-0719	2.81E5
J1744-1134	3.048E5

4.1.4.3 Simulation Scenarios.   Based on the aforementioned parameter settings and flags, groups of scenarios were created to answer the questions posed by the research objectives. Table 4.2 displays the scenarios created for the SISRE experiments. Note that the third column displays the order of accuracy, in meters, of the pulsar with highest timing accuracy (i.e., lowest σ_{TOA}) expressed in meters. Each scenario will be described in detail in one of the following sections.

4.1.4.4 Application of the Matlab® Pseudo-random Number Generator. An important aspect of the analysis and creation of each scenario was the application of Matlab®'s pseudo-random number generator to simulate random processes. The pseudo-random number generator uses an algorithm that produces approximately random numbers. In reality, given an initial value (called the 'random seed'), the algorithm will produce the same series of numbers every time it is implemented [8].

4-9

Table 4.2:   Simulation Scenarios

Scenario Number	Description	σ_{TOA} Accuracy For Most Accurate Pulsar (m)
1a	PR observations only	-
1b	PR + TDOAs (16 pulsars)	42.2
1c	PR + TDOAs (16 pulsars)	0.1
1d	PR + TDOAs (2 pulsars)	13.4
1e	PR + TDOAs (2 pulsars)	4.2
1f	PR + TDOAs (2 pulsars)	1.3
1g	PR + TDOAs (2 pulsars)	0.4
2a	PR + TDOAs (16 pulsars)	13.4
2b	PR + TDOAs (8 pulsars)	13.4
2c	PR + TDOAs (4 pulsars)	13.4
2d	PR + TDOAs (2 pulsars)	13.4
2e	PR + TDOAs (1 pulsar)	13.4
2f	PR + TDOAs (1 pulsar)	1.1
3a	PR outage (22 hours) - no TDOAs	-
3b	PR outage (20 hours) - no TDOAs	-
3c	PR outage (18 hours) - no TDOAs	-
3d	PR outage (15 hours) - no TDOAs	-
3e	PR outage (10 hours) - no TDOAs	-
3f	PR outage (22 hours) + TDOAs (16 pulsars)	42.2
3g	PR outage (20 hours) + TDOAs (16 pulsars)	42.2
3h	PR outage (18 hours) + TDOAs (16 pulsars)	42.2
3i	PR outage (15 hours) + TDOAs (16 pulsars)	42.2
3j	PR outage (10 hours) + TDOAs (16 pulsars)	42.2
3k	PR outage (22 hours) + TDOAs (1 pulsar)	1.8
3l	PR outage (20 hours) + TDOAs (1 pulsar)	1.8
3m	PR outage (18 hours)+ TDOAs (1 pulsar)	1.8
3n	PR outage (15 hours) + TDOAs (1 pulsar)	1.8
3o	PR outage (10 hours) + TDOAs (1 pulsar)	1.8
4a	Variable Geometry - 3 planar transmitters at 5 deg apart	0.1
4b	Variable Geometry - 3 planar transmitters at 120 deg apart	0.1
4c	Variable Geometry - 3 orthogonal transmitters	0.1

The simulation used this property of Matlab$^{\circledR}$'s pseudo-random number algorithm to compare the results of separate scenario runs. By assigning sets of scenarios the same random seed value, the SISRE values between different scenarios could be related to one another. A common random seed value allowed each scenario to implement the random processes to realistically simulate measurement noise, clock walk, etc. while at the same time adhering to a baseline that allowed all scenarios to be fundamentally related and thus comparable. Without a common random number seed, any given scenario could not be replicated. Additionally any two scenarios in a given set could not be compared in a meaningful way, because the inherent randomness of each scenario may change the ultimate SISRE values, resulting in unpredictably varying results every time they were run. Without the ability to control the random number algorithm, no analysis could be done between 2 scenarios, because the SISRE magnitude could not be repeated.

As an example, suppose two scenarios with different parameter values were run multiple times in order to make a comparison in their $\text{SISRE}_{constellation}$ values. Without the same random seed in each scenario, the respective SISRE results will vary unpredictably in such a manner that it would be impossible to interpret the $\text{SISREs}_{constellation}$ – are the values the result of a phenomenon in a particular scenario or are they just the result of random effects? The $\text{SISRE}_{constellation}$ for the first scenario may be lower than the second one for the first 3 trials. However, during the next 5 trials, scenario 2 may have a lower $\text{SISRE}_{constellation}$ because of the intrinsic randomness built into the scenarios. Using the same random seed allows the randomness of two disparate scenarios to be normalized so that their results can be compared on a uniform scale.

In this simulation, 2 different types of pseudo-random number algorithms were used. The primary algorithm used in the simulation was the *randn* function which generated a series of normally distributed random numbers and the *rand* function which generated uniformly distributed random numbers. The *randn* function was used to model the random walk of the satellite and ground station clocks, and measurement

4-11

noise in the PRs and TDOAs. Additionally *randn* was used to corrupt the batch filter's initial guess of the GPS satellites' true state vectors so that it was offset from the A1 generated truth model. A second random generator, *rand*, was used to randomly pick initial af_0 and af_1 terms for the ground station clocks because of the unavailability of their true operational values.

For most scenarios, four instances of the exact same scenario were run with different random seeds. Scenarios run with random seeds of 100 were classified as the 10 series (e.g., 1, 2, 3...). Scenarios run with a random seed of 10,000 were classified as the 100 series (e.g., 101, 102, 103,...). Scenarios run with random seeds of 17 were classified as the 200 series (e.g., 201, 202, 203,...). Finally, scenarios run with random seeds of 1977 were classified as the 300 series (e.g., 301, 302, 303,...). Therefore, scenarios across random seeds were comparable based on their assigned number. For example, scenarios 1, 101, 201, and 301 would all represent the same scenario structure type but would have different output values because of the different random seed numbers used. In order to get an average value over all the scenario variants, a RMS value was calculated for each scenario type.

For every individual scenario, a SISRE$_{satellite}$ value was calculated for all 29 satellites in the constellation. Additionally, each scenario computed a SISRE$_{constellation}$ value made up of an average (RMS) of all 29 SISRE$_{satellite}$ values. For every scenario type, a Total RMS SISRE$_{satellite}$ value was calculated as well as a Total RMS SISRE$_{constellation}$ number.

To illustrate this methodology, scenarios 1, 101, 201, and 301 will be used as an example. For each scenario, 29 SISRE$_{satellite}$ values were calculated as well as 1 SISRE$_{constellation}$ value. Next, using each satellite's 4 total SISRE$_{satellite}$ metric values a Total RMS SISRE$_{satellite}$ number was computed. Analogously, in each of the 4 scenarios, a SISRE$_{constellation}$ number was calculated. Taking the average of these 4 numbers, a Total RMS SISRE$_{constellation}$ value was calculated for the scenario

type. For the analysis that follows, naming of a scenario (e.g., scenario 1) implies the combination of all four of the random seed results, unless specifically stated otherwise.

4.2 Batch Filter Functionality Check

Before any scenarios were run through the simulation, the batch filter was tested by adding an arbitrary constant offset to the initial state estimate at epoch. If the measurement errors are subsequently turned off, any differences between the propagated truth states (i.e., the observations) and the corresponding calculated states will be due solely to this initial offset.

Implementing the method mentioned above, an offset of 25 meters was added to each position component (x, y, z) of the initial truth ECEF state as well as the clock bias. This state represented an initial guess, or perhaps the last known estimate of the satellite's position and bias components, which were to be updated/corrected by the filter. In spite of this relatively large offset, the batch filter successfully corrected this initial estimate to within 10^{-7} m of the corresponding truth values in each positional component.

A similar test was performed by introducing an arbitrary offset in the velocity components $(\dot{x}, \dot{y}, \dot{z})$ of the initial truth state as well as in the clock drift. The satellite trajectories were much more sensitive to changes in velocity than to changes in position. Thus, if these offsets were too large, the residuals (i.e., the differences between the truth or observed quantities and the calculated quantities) could have become sufficiently large which would have caused the filter to diverge. Hence, the offsets used were somewhat smaller for this test (5 cm/sec) and resulted in about 4 km of positional error in each component after 24 hours of propagation (2 orbits). Using this offset, the batch filter again corrected initial state estimate to within 10^{-7} m of the corresponding truth values in each velocity/clock drift component.

4.3 Test 1: Qualify the Improvement of TDOAs from Pulsars on GPS SISRE

Test 1 attempted to quantify, through two separate experiments, the overall impact of using TDOAs to decrease the SISRE in a PR-only GPS system. Scenario 1, listed in Table 4.2, simulated an operational GPS system without the supplemental TDOA observations. This scenario served as a baseline reference for the all of the PR + TDOA scenarios used in this test. Using the four different random seed variants of scenario 1 (i.e., 1, 101, 201, 301), the $SISRE_{satellite}$ values for each satellite were calculated. Figures 4.1 – 4.4 demonstrate the variability of $SISRE_{satellite}$ values depending on the random seed used.
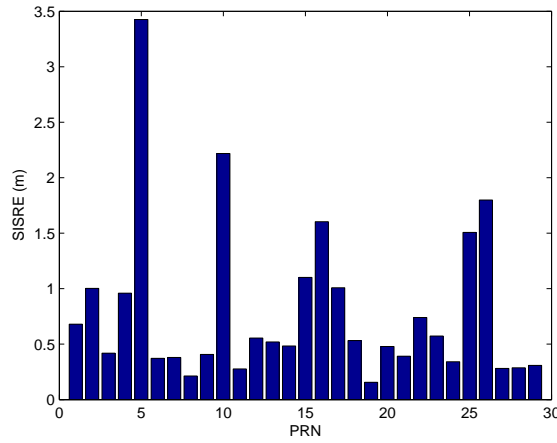
Figure 4.1:   PR-only $SISRE_{satellite}$ Values (Random Seed = 100)

Examining each figure, the variability of each PRN's (satellite) $SISRE_{satellite}$ value is made clear. This variability from one random seed scenario to the next makes it difficult to judge overall PRN performance. It was therefore determined that individual scenario $SISRE_{satellite}$ values could not be used, because no meaningful comparison could be made to other scenario types (i.e., which $SISRE_{satellite}$ value would be used in the comparison to other scenario types?). Thus, in any analysis involving individual satellites that follows, only the Total RMS $SISRE_{satellite}$ value
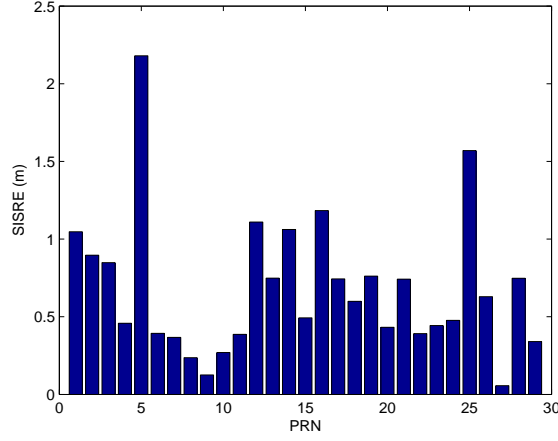
Figure 4.2:   PR-only SISRE$_{satellite}$ Values (Random Seed = 10000)
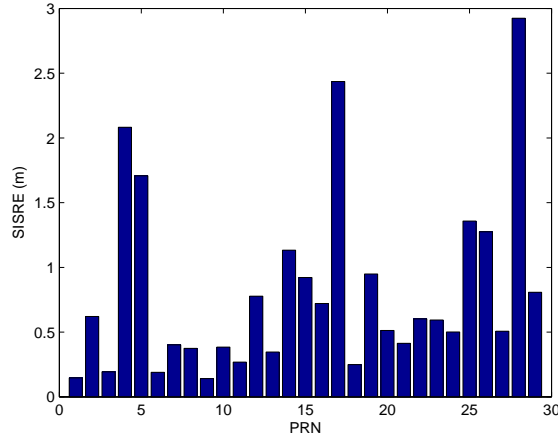
Figure 4.3:   PR-only SISRE$_{satellite}$ Values (Random Seed = 17)

(referred hereafter as RMS SISRE$_{satellite}$), which represents each satellite's average SISRE$_{satellite}$ value, will be referenced.

4.3.1   Evaluating the Effect of Adding Nominal TDOA Measurements.   The first experiment of Test 1 compared the SISRE values of a PR-only (scenario 1a) scenario to that of a PR + nominal TDOA (scenario 1b) scenario. In scenario 1b, 16 pulsars were introduced into the simulation, creating 42,016 additional measurements

4-15
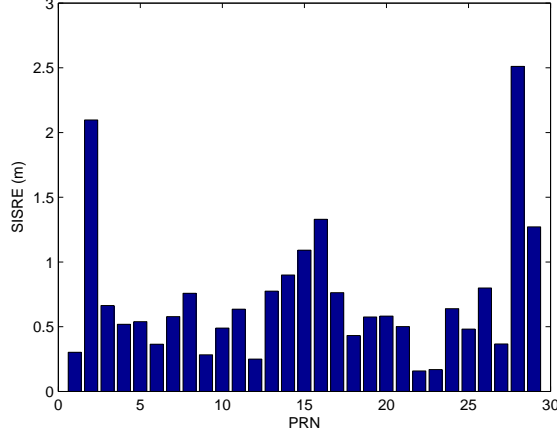
Figure 4.4:   PR-only SISRE$_{satellite}$ Values (Random Seed = 1977)

in the form of TDOA observations. The nominal σ_{TOA} values from Table 4.1 were used.

First, the RMS SISRE$_{satellite}$ values for scenarios 1a and 1b were plotted and compared. Figure 4.5 compares the average RMS SISRE$_{satellite}$ values for each satellite. The data shows that overall, 12 of the 29 satellites had a RMS SISRE$_{satellite}$ that was higher after TDOAs were introduced to the filter.

To explain the apparent satellite-by-satellite SISRE degradation for those 12 satellites, state vector and SISRE component (radial, along-track, cross-track) comparisons were made in an attempt to correlate the decreased accuracy with actual differences (errors) between the batch filter's estimate of certain parameters and the truth model's actual values for these parameters. The "difference" or "error" was always defined as the (estimate - truth).

The first parameter comparison involved calculating the actual spatial distance between the estimated state at epoch and the truth state at epoch. Using the distance formula, a 3-dimensional physical distance between the estimated and true epoch states was calculated. In essence, the distance between the estimated state and truth state can be considered the position error for each satellite (3-D Position Error(RMS)). Figure 4.6 shows these differences between scenarios 1a and 1b. This indicates the

4-16
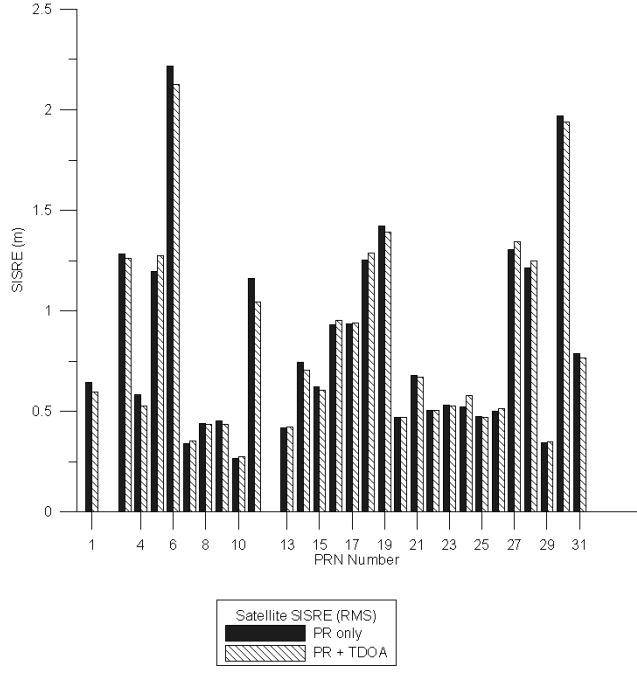
Figure 4.5:   RMS SISRE$_{satellite}$ Comparison Between PR-only (Scenario 1a) and PR + Nominal TDOA (Scenario 1b)

random nature of the results and the need to look at a metric that is more general than the satellite-by-satellite RMS SISRE$_{satellite}$.

Comparing the satellites that had overall degrading SISREs in Figure 4.5 with those in Figure 4.6 did not appear to present a one-to-one correlation. In other words, those PRN's that had RMS SISRE$_{satellite}$ values that became worse in scenario 1b did not necessarily have a worse position error in scenario 1b when compared to their position error in scenario 1a.

Next, the errors in the SISRE components were compared. Figures 4.7 – 4.10 used the SISRE-based frame to display each satellite's three position component errors and clock bias error (measured in meters).

The results from Figures 4.7 – 4.10 also did not show a direct correlation to RMS SISRE$_{satellite}$ degradation in scenario 1b for selected PRN's when compared to scenario 1a.

4-17
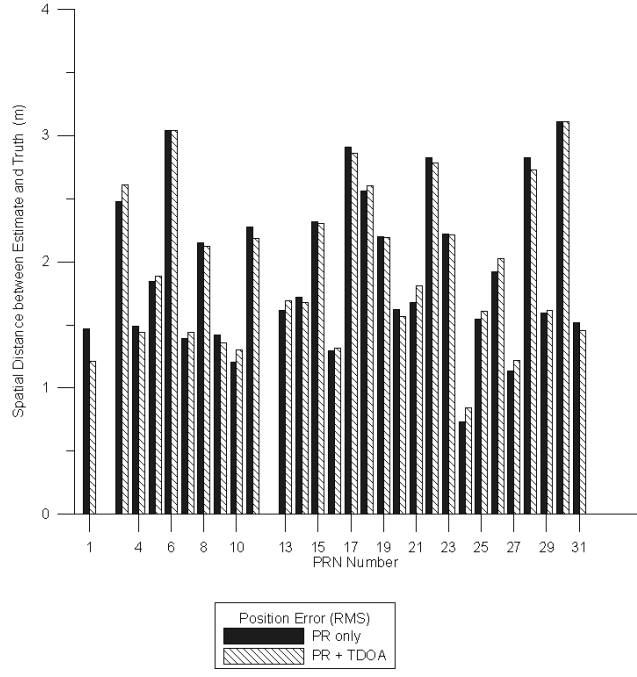
Figure 4.6:   Satellite RMS 3-D Position Error
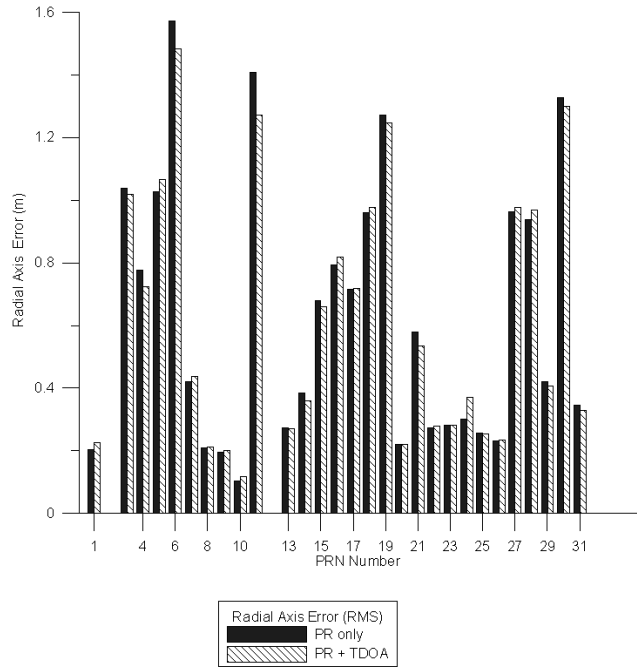
Figure 4.7:   RMS Error in Radial Axis

Ultimately, Figures 4.5 – 4.10 indicate that there is great variability in SISRE performance on an individual satellite level. The effects of RMS SISRE$_{satellite}$ getting worse with the introduction of TDOAs cannot be directly attributed to the batch

4-18
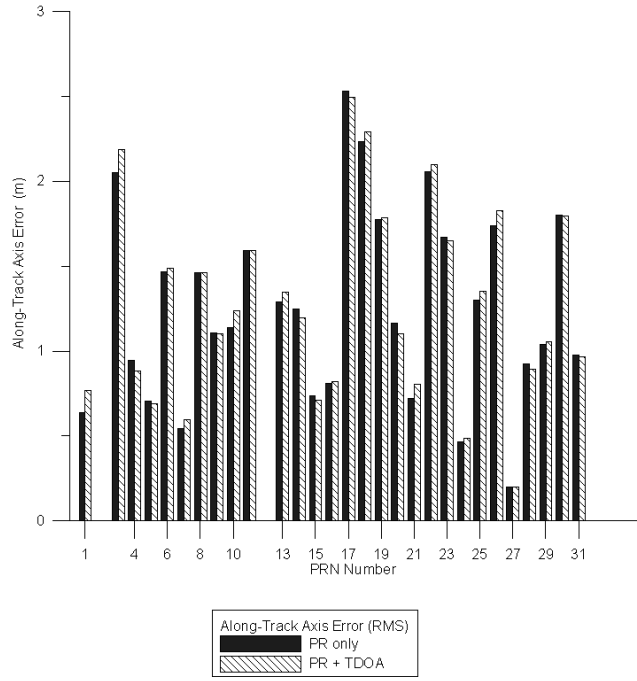
Figure 4.8:   RMS Error in Along-Track Axis
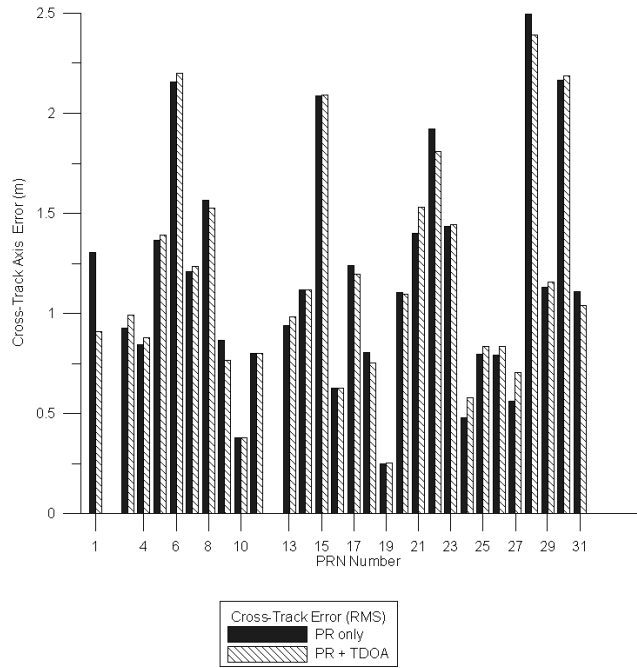
Figure 4.9:   RMS Error in Cross-Track Axis

filter's estimate of (x, y, z) position error, along-track error, cross-track error, radial error, or bias error on an individual basis.
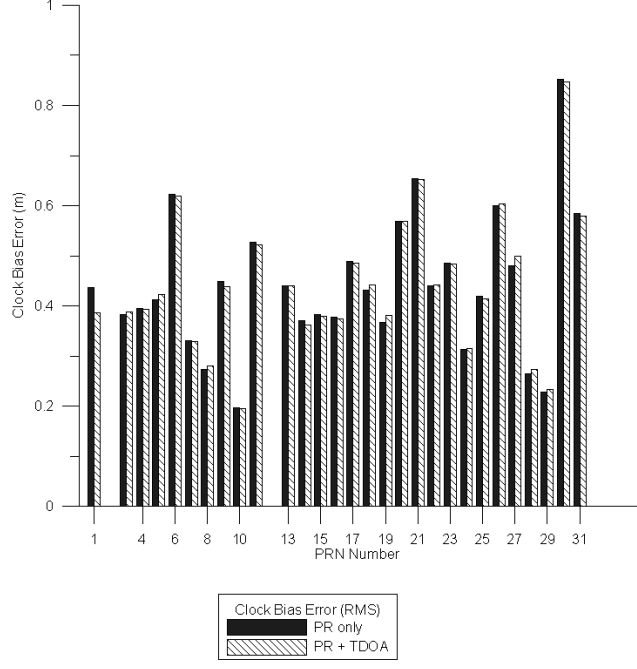
Figure 4.10:   RMS Error in Clock Bias

The degrading of RMS SISRE$_{satellite}$ between scenarios 1a and 1b can most likely be attributed to the variable nature of the SISRE$_{satellite}$ metric. One possible explanation for the SISRE$_{satellite}$ variability has to do with the statistics of using different random seeds for each scenario. It is plausible that in using the SISRE$_{satellite}$ metric, the random errors that pervade each scenario are not being averaged out with the number of samples that were used (4 different random seeds per scenario).

The variability between RMS SISRE$_{satellite}$ values necessitated that the Total RMS SISRE$_{constellation}$ (referred hereafter as the RMS SISRE$_{constellation}$) metric be utilized over RMS SISRE$_{satellite}$. A meaningful assessment of SISRE improvement could not be made using RMS SISRE$_{satellite}$ and therefore, an attempt was made to smooth the random effects of each random seed by using the RMS SISRE$_{constellation}$. The SISRE$_{constellation}$ was useful because it indicated the overall average of the improvement of SISRE on a constellation scale.

Table 4.3 shows the RMS errors in position, along-track, cross-track, radial and bias for scenarios 1a and 1b, the RMS of SISRE$_{constellation}$, the $\sigma_{constellation}$ values along

with the overall percent improvement of scenario 1b over scenario 1a for each of these measurements.

Table 4.3: Performance Comparison Between PR-only (Scenario 1a) and PR + Nominal TDOAs (Scenario 1b)

	PR-only (Scenario 1a)	PR + Nominal TDOA (Scenario 1b)	% Improvement
3-D Position Error (RMS)	2.031 m	2.031 m	0.00
3-state $\sigma_{constellation}$	1.987 m	1.974 m	.65
Along-Track Error(RMS)	1.372 m	1.391 m	-1.40
Cross-Track Error (RMS)	1.293 m	1.282 m	0.89
Radial Error (RMS)	0.753 m	0.738 m	2.07
Clock Bias Error (RMS)	0.461 m	0.460 m	0.31
RMS of SISRE$_{constellation}$	0.963 m	0.953 m	1.03

Results from Table 4.3 show that there was no significant improvement in the position error between scenario 1a and 1b. To verify this result, a three-state (x, y, z) covariance, $\sigma_{constellation}$ (also shown in Table 4.3), was calculated for both scenarios. The $\sigma_{constellation}$ values above appear to indicate that indeed TDOAs do help to decrease the position error of the GPS constellation as a whole.

Theoretically, the RMS position errors and the $\sigma_{constellation}$ covariance values for scenarios 1a and 1b should be closely aligned. In a zero mean sample of data, there is a relationship between the RMS of the data and its corresponding standard deviation. Therefore, the RMS based position error should approximate the three-state covariance, $\sigma_{constellation}$, which is a standard deviation. Indeed Table 4.3 illustrates that each $\sigma_{constellation}$ is similar in magnitude to the 3-D RMS Position Error which verifies the theory that the RMS and standard deviation of a sample of data should approximate each other.

Additionally, Table 4.3 shows that, as a constellation, the radial error improved the most and AT error degraded slightly. One possible explanation for the radial error improvement could be that the augmented observation geometry provided by

the addition of TDOAs has given the batch filter more information to solve for the error that is most known by the GPS system already. In the operational GPS system, the radial error is relatively low (compared to the AT and XT errors) because the pseudorange observations measure the distance to the GPS satellites from the Earth in the radial direction. Additionally, the radial distance of each GPS satellite is well known because the orbital period of each satellite is a function of the radial distance from the center of the Earth. It is possible that the TDOAs have enabled the filter to more accurately solve for an error that is well known already. It is unknown why the AT error became worse with the addition of TDOAs in the batch filter.

Finally, the overall RMS $\text{SISRE}_{constellation}$ was calculated for both scenarios 1a and 1b using each scenarios's four separate randomized scenario variants. It was expected that comparing these two values would indicate if, overall, TDOAs would aid in decreasing SISRE levels in the GPS constellation. Table 4.3 compares the RMS $\text{SISRE}_{constellation}$ of scenario 1a with scenario 1b. The results indicated that TDOA's can very slightly decrease the SISRE levels in a constellation of satellites whose positions are determined using only pseudorange observations. The percent improvement of scenario 1b over scenario 1a was approximately 1.03%.

One possible explanation for the improvement is the fact that with the addition of approximately 40,000 TDOA observations, the batch filter has more data to perform the least squares estimate and thus, can perform the estimate more accurately. The reason for the marginal improvement of scenario 1b over scenario 1a may be attributed to the overall lower accuracy of the TDOAs with respect to the PR observations. The pulsars had TDOA measurements that were, at best, accurate to 42 m. In contrast, PR measurements were accurate to approximately 1 m. Therefore, the filter did not weigh the TDOA measurements equally with the pseudoranges. Based on the comparison between the PR-only and PR + TDOA (nominal) scenarios, it can be asserted that adding 16 pulsars whose timing accuracies are equal to or worse than 40 m will only marginally improve the estimates of an operational PR-only GPS system.

4.3.2 Evaluating the Effect of Increasing the Accuracy of the Nominal TDOA Measurements. The next experiment attempted to quantify the actual improvement in SISRE that could be achieved when nominal TDOA measurements were replaced with TDOA measurements that were orders of magnitude more accurate. The PR + highly accurate TDOA (scenario 1c) scenario was compared to the PR-only (scenario 1a) scenario in order to analyze the effects of incorporating more accurately timed x-ray pulses at each satellite. This comparison between scenarios 1a and 1c was then contrasted with the previous section's comparison of scenarios 1a and 1b (PR, PR + nominal TDOA) to investigate the effectiveness of incorporating increased accuracy TDOAs on the SISRE.

Table 4.4 lists the same pulsars as in Table 4.1. However, the σ_{TOA} values are orders of magnitude lower than those in Table 4.1. Thus, each pulsar contributes TDOA observations to the batch filter, through a more accurate detector, that are orders of magnitude more accurate than those of the PR + nominal TDOA scenario.

Table 4.4: Highly Accurate Pulsar σ_{TOA}

Pulsar	σ_{TOA} (m)
B0531+21 (Crab Pulsar)	0.177
J0437-4715	13.6
B1821-24	5.5
J2124-3358	58.1
J1012+5307	405.5
J0218+4232	26.3
J0751+1807	78.4
B1937+21	8.3
B1257+12	545.8
B1820-30A	0.08
B1620-26	107.3
J2322+20	771.8
J2019+24	212.2
J0030+0451	37.5
J1024-0719	562.1
J1744-1134	609.8

Table 4.5 shows the RMS of SISRE$_{constellation}$, errors (estimate - truth) in 3-D position (RMS), along-track, cross-track, radial and bias for scenarios 1a and 1c. Additionally, the $\sigma_{constellation}$ values along with the overall percent improvement of scenario 1c over scenario 1a for each of these measurements.

Comparing the RMS SISRE$_{constellation}$ values of scenario 1c and 1a shows that overall, SISRE$_{constellation}$ can be significantly lowered with the introduction of increasingly accurate TDOAs. Using the RMS SISRE$_{constellation}$ values for scenario 1a and 1c listed in Table 4.5, the average improvement of using highly accurate TDOAs (as compared to the nominal TDOAs implemented in scenario 1b) versus only PR observations is approximately 26%.

A comparison was also made between scenarios 1a and 1c of their 3-D position errors and RMS SISRE$_{constellation}$ component errors. This comparison was analogous to the comparison made in Table 4.3. Table 4.5 shows that indeed each error decreased in scenario 3.

Table 4.5:   Performance Comparison Between PR-only (Scenario 1a) and PR + Highly Accurate TDOAs (Scenario 1c)

	PR-only (Scenario 1a)	PR + Highly Accurate TDOAs (Scenario 1c)	% Improvement
RMS SISRE$_{constellation}$	0.963 m	0.713 m	26.0
3-D Position Error (RMS)	2.031 m	1.405 m	30.8
3-state $\sigma_{constellation}$	1.987 m	0.203 m	89.8
Along-Track Error (RMS)	1.372 m	0.800 m	41.7
Cross-Track Error (RMS)	1.293 m	0.999 m	22.8
Radial Error (RMS)	0.753 m	0.580 m	23.0
Clock Bias Error (RMS)	0.461 m	0.363 m	21.4

Comparing the along-track error results of Table 4.5 with Table 4.3, it was noticed that the along-track error had the most variability. In Table 4.3, results showed that the PR + TDOA (nominal) scenario's along-track error was slightly degraded as compared to scenario 1a's along-track error. With the introduction of

highly accurate TDOAs in scenario 1c, Table 4.5 indicates an overall improvement of almost 42%. However, the jump in along-track error (RMS) (see Table 4.3) magnitude cannot be explained.

Using the results Table 4.5, it can be said that the introduction of highly accurate TDOAs would greatly help the batch filter's estimate of the GPS satellite positions. This assertion was further verified when the 3-state covariance, $\sigma_{constellation}$, was calculated for scenario 1c and compared to the $\sigma_{constellation}$ value of scenario 1a.

Table 4.5 shows that scenario 1c $\sigma_{constellation}$, was calculated to be 0.203 m. Compared to the $\sigma_{constellation}$ values of 1.987 m scenario 1a, it is evident that scenario 1c's highly accurate TDOAs have improved the filter's estimation capabilities. Furthermore, scenario 1c's $\sigma_{constellation}$ is much lower than the $\sigma_{constellation}$ of the nominal TDOA case (scenario 1b) shown in Table 4.3 corroborating the assertion that highly accurate TDOAs represent a greater benefit to lowering the SISRE than nominal TDOAs. Note that the $\sigma_{constellation}$ for scenario 1c is significantly lower than the corresponding 3-D position error (RMS) value possibly indicating that there may be biases in the SISRE values not evident in the $\sigma_{constellation}$. Ideally, as stated in the previous section, the magnitude of 3-D position error (RMS) of scenario 1c would have approximated its $\sigma_{constellation}$.

The reason for the dramatic SISRE improvement can be directly linked to the increase in pulsar TOA accuracies over the nominal TOA accuracies listed in Table 4.1. In both scenarios 1b and 1c, approximately 40,000 additional data points in the form of TDOA observations were added to the batch filter. The important difference of scenario 1c is that the TDOAs were, at best, three orders of magnitude better in scenario 1c (0.08 m for PSR B1820-30A in scenario 1c versus 42.2 m in scenario 1b). Correspondingly, based on Equation (3.60), the filter assigned a larger weight to TDOA observations. The combination of increased σ_{TOA} accuracies and higher weighting values assigned by the batch filter in the W matrix drove SISRE values down for scenario 1c. Essentially, the filter was able to use more accurate information

through scenario 1c, that allowed it to calculate a more accurate GPS state vector estimate.

4.3.3 SISRE Sensitivity Analysis.   A sensitivity analysis was conducted to evaluate the impact of increasingly accurate σ_{TOA} values on RMS SISRE$_{constellation}$ performance. The two previous sections illustrated an overall affect of using TDOAs to lower SISRE. In this experiment, the accuracy of σ_{TOA} for each pulsar was progressively improved to ascertain any SISRE performance trends by artificially varying elements of Equation (2.20). Scenarios 1d, 1e, 1f, 1g referenced in Table 4.2 were used to implement the changes to σ_{TOA} and observe the trend in SISRE.

Figure 4.11 illustrates how RMS SISRE$_{constellation}$ responds to changes in σ_{TOA}. In order to plot the SISRE behavior, the independent variable σ_{TOA} is depicted in the figure by the σ_{TOA} of the strongest pulsar, PSR B1820-30A, which would represent a detector's accuracy ceiling (i.e., since PSR B1820-30A's σ_{TOA} is the smallest out of the pair of PSRs used, its σ_{TOA} value represents the detector's upper accuracy limit).
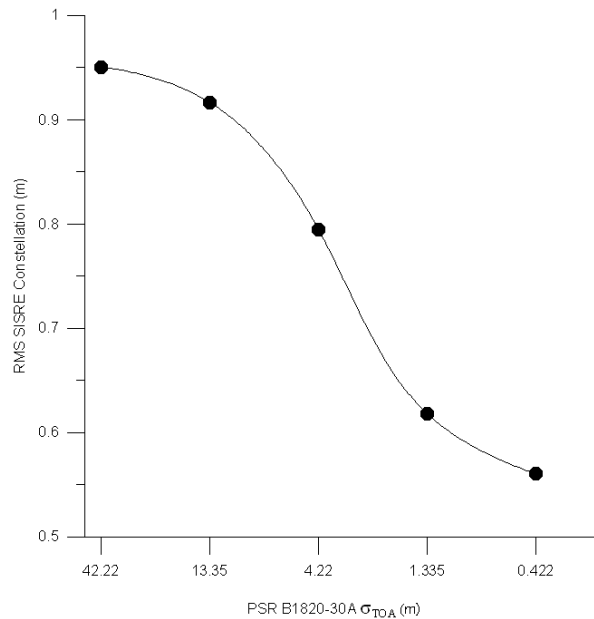
Figure 4.11:   Comparison of RMS SISRE$_{constellation}$ Performance with Increased σ_{TOA} Accuracy

Figure 4.11 shows that the performance of RMS SISRE$_{constellation}$ behaves non-linearly as the σ_{TOA} drops in orders of magnitude. The apparent leveling trend that appears between the σ_{TOA} of 1.335 m and 0.422 m may indicate that increasing the accuracy of the detector after a certain point, whether through increased area or increased observation time, etc., may not yield SISRE improvements that are orders of magnitude better. It is unknown why there may be an apparent SISRE vs pulse timing accuracy threshold.

4.4 Test 2: Quantify the Number of Pulsars Needed to Lower GPS SISRE

With the possibilities of SISRE improvement demonstrated through scenarios 1b and 1c, the next test endeavored to determine the number of pulsars needed to appreciably lower the GPS SISRE. Under operational conditions, the use 16 of pulsars to create TDOA measurements may not be feasible or even possible because of detector pointing limitations, etc. Therefore this test incrementally decreased the number of pulsars used to create TDOA measurements. Pulsars were successively eliminated based solely on their σ_{TOA} values. The pulsars that could create the most accurate (i.e., lowest σ_{TOA}) TOA measurements were eliminated last.

Referencing Table 4.2, scenarios 2a, 2b, 2c, 2d, and 2e were used to incrementally step down the number of pulsars used from 16 pulsars down to 1 pulsar. Table 4.6 lists each pulsar and its corresponding σ_{TOA} for these set of scenarios.

Table 4.7 shown below lists the RMS SISRE$_{constellation}$ as well as the 4-state (x, y, z, bias) covariance, $\sigma_{constellation}$, for each scenario in Test 2. Additionally scenario 2f, which used the single pulsar from scenario 2e with an increased σ_{TOA} accuracy, is also displayed. However, scenario 2f will be discussed later in the section.

Table 4.7 indicates that the magnitude of the SISRE for all scenarios is driven by the most accurately timed pulsar. The value of the SISRE$_{constellation}$ for the scenarios varied marginally ranging from 0.916 m in scenario 2a ,which utilized 16 pulsars, to

Table 4.6:   Pulsar σ_{TOA} for Scenarios 2a – 2e

Pulsar	σ_{TOA} (m)
B0531+21 (Crab Pulsar)	27.98
J0437-4715	2144.66
B1821-24	874.28
J2124-3358	9189.55
J1012+5307	6.41E4
J0218+4232	4155.38
J0751+1807	1.24E4
B1937+21	1312.07
B1257+12	8.63E4
B1820-30A	13.35
B1620-26	1.69E4
J2322+20	1.22E5
J2019+24	3.35E4
J0030+0451	5923.9
J1024-0719	8.89E4
J1744-1134	9.64E4

0.911 m in scenario 2e, which relied on a single pulsar. It may be possible to infer from this experiment that using only one pulsar, which can be very accurately timed, may be equivalent to or better than using tens of pulsars with very weak timing statistics. Indeed there appears to be a 5% SISRE improvement between scenario 2e, using 1 pulsar, and scenario 1a (see Test 1) using only PR observations. This improvement is greater than the 1.03% improvement of scenario 1b (PR + nominal TDOA) over scenario 1a discussed in the previous section.

However, even scenario 2e's SISRE$_{constellation}$ of 0.911 m (only millimeter level improvement) is not much justification to augment the GPS observation matrix with TDOA measurements when scenario 1's PR-only SISRE$_{constellation}$ was 0.963 m. As demonstrated in Section 4.3, the pulsars, even with increased accuracy, are still weighted much less than a pseudorange observation. Therefore, it was desirable to observe how the RMS SISRE$_{constellation}$ value would behave if the TDOAs received a weighting equivalent to each pseudorange (i.e., if pulsar measurements were as accurate as a pseudorange measurement). In the next experiment (scenario 2f), one pulsar

Table 4.7:   Performance Values for Scenarios 2a – 2f

Number of Pulsars (Scenario #)	RMS SISRE$_{constellation}$ (m)	$\sigma_{constellation}$ (m)
16 (scenario 2a)	0.916	1.915
8 (scenario 2b)	0.916	1.915
4 (scenario 2c)	0.916	1.915
2 (scenario 2d)	0.916	1.915
1 (scenario 2e)	0.911	1.915
1 (Highly Accurate) (scenario 2f)	0.681	1.056

was used and the timing accuracy of the detector was increased to a level that would allow the batch filter to weight each TDOA with the same weight as a pseudorange measurement. In order to accomplish this weighting, the pulsar's σ_{TOA} was artificially set to 1.05 m. Table 4.7 lists the SISRE characteristics of scenario 2f.

With the increased pulsar timing accuracy; scenario 2f dramatically lowered the SISRE level from the plateau of scenarios 2a through 2e. The RMS SISRE$_{constellation}$ level, in scenario 2f, improved by 25% to a level of 0.681 m. The reason for this improvement can possibly be attributed again to the fact that through the TDOA observations, which were more accurate than previous scenarios and thus were weighted more heavily, the filter was able to use the least squares algorithm to more accurately adjust its estimate of truth for each satellite position and clock bias.

The results of this analysis were further verified using a comparison of the $\sigma_{constellation}$ values for scenario 2a – 2f, also listed in Table 4.7. The $\sigma_{constellation}$ results from Table 4.7 corroborate the results depicted in the assertions made about scenario 2f's performance. Scenarios 2a – 2e all had approximately equivalent SISRE$_{constellation}$ values because the SISRE$_{constellation}$ magnitude was being driven by the strongest (i.e., smallest σ_{TOA}) pulsar. Correspondingly, the $\sigma_{constellation}$ values for scenarios 2a – 2e were equivalent demonstrating that the filter's ability to estimate errors in GPS satellite position and clock bias were approximately equal. With the addition of more accurate pulsar measurements in scenario 2f, the batch filter's uncertainty in position and clock error decreased, which was expected based upon the SISRE results.

4.5 Test 3: GPS Ground Station Outage Experiment

The next experiment attempted to determine if TDOAs could support GPS in the event that ground stations could no longer be used to obtain pseudorange observations. It was postulated before these simulations were run that TDOAs could help sustain manageable SISRE levels in the event that pseudoranges were not present for a limited amount of time. Three sets of scenarios (see scenarios 3a – 3o in Table 4.2) were created to incrementally simulate total ground station blackouts for hours at time. Scenarios 3a – 3e represented a GPS system without the benefit of TDOA observations during a PR outage. Scenarios 3f – 3j represented a GPS system that incorporated TDOA observations garnered from 16 pulsars using a pulsar x-ray detector that was accurate to approximately 40 m (see Table 4.1). Finally, scenarios 3k – 3o represented a GPS system that utilized 1 pulsar to make TDOAs during a PR outage. For each outage scenario, pseudoranges were generated for 1 – 5 hours initially before the outage began. The outages lasted from 10 – 22 hours before the pseudoranges resumed during the last interval to complete the 24 hour simulation run.

Figure 4.12 shows the results of the simulation being run to compare outages that only used PRs and outages that used TDOAs to sustain the observation geometry of the GPS constellation. The results indicated that using TDOAs in the absence of PRs for a limited amount of time may aid the OCS in keeping track of the GPS satellites until the ground station links to the constellation could be reestablished.

To further explore this phenomenon, a feasibility study was conducted using scenarios 3k - 3o. These scenarios duplicated the efforts of scenarios 3f - 3j in that the scenarios divided the observations into three blocks. Block 1 began with pseudoranges only for the first hour or more. Block 2 simulated a complete ground station outage by denying the constellation the use of PRs. However, instead of using 16 pulsars, only 1 pulsar was used. The 1 pulsar used was PSR B0531+21 (Crab Pulsar) which is a very well known bright pulsar in the Crab Nebula [28]. Feasibly, if GPS x-ray detectors were
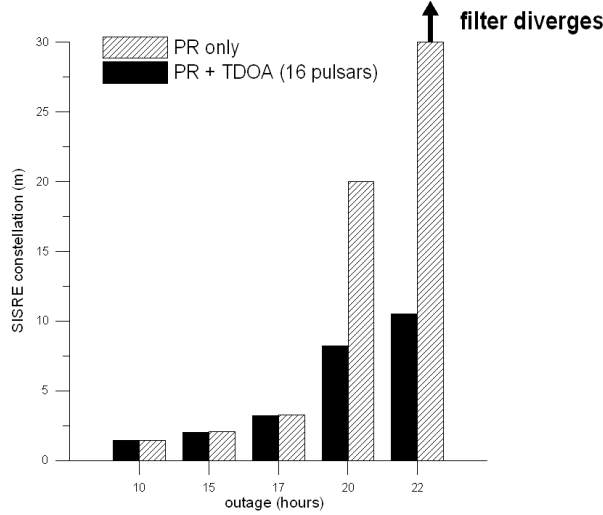
Figure 4.12: Comparison of SISRE$_{constellation}$ values during GPS Ground Station Outages. The PR + TDOA scenarios used 16 pulsars to create TDOAs. Scenarios 3a, 3b, 3c, 3d, 3e represent PR-only outages of 22 hrs, 20 hrs, 18 hrs, 15 hrs, 10 hrs respectively. Scenarios 3f, 3g, 3h, 3i, 3j represent PR + TDOA outages of 22 hrs, 20 hrs, 18 hrs, 15 hrs, 10 hrs respectively.

limited to the use of one bright x-ray emitting pulsar during the TDOA observation window, the Crab Pulsar would be a very good candidate because its characteristics have been widely studied and therefore a detector could be optimally designed to specifically detect its pulse profile. In this simulation, GPS x-ray detectors were simulated to have accuracies on the order of 1.8 m while solely observing the Crab Pulsar. Block 3 simulated a reestablishment of PRs and therefore TDOA observation use was discontinued for the remainder of the 24 hour simulation.

Figure 4.13 depicts the comparison between PR-only based outage scenarios and outage scenarios where TDOA observations were allowed. The results of this experiment seem to say that using one pulsar that can be accurately timed to the order of 1.8 m may be sufficient to sustain manageable SISRE$_{constellation}$ needs until pseudoranges can be reintroduced.
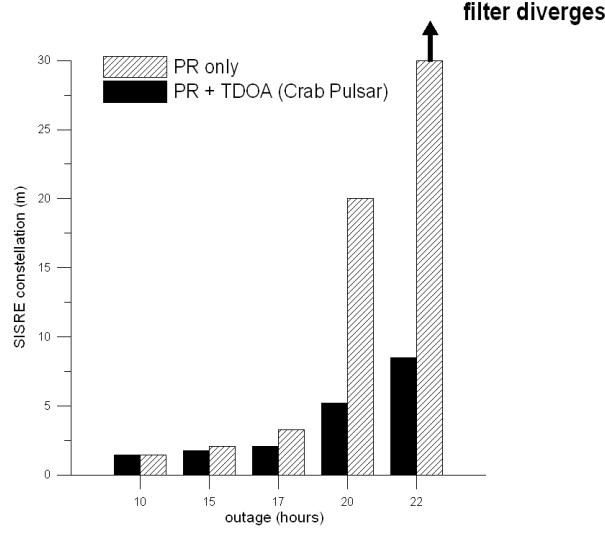
Figure 4.13: Comparison of SISRE$_{constellation}$ values during GPS Ground Station Outages. Scenarios 3a, 3b, 3c, 3d, 3e represent PR-only outages of 22 hrs, 20 hrs, 18 hrs, 15 hrs, 10 hrs respectively. Scenarios 3k, 3l, 3m, 3n, 3o represent PR + TDOA outages of 22 hrs, 20 hrs, 18 hrs, 15 hrs, 10 hrs respectively using only the Crab Pulsar.

Overall results from these two experiments seem to indicate that from a constellation perspective, the use of TDOA observations in the absence of pseudoranges can sustain the observability needed for the batch filter to maintain the satellite geometry. It is important to note that in reality, a ground station outage would not create such catastrophic results in such a short time period. The real OCS, in the event of a total communications blackout, would be able to draw on past state vector data via the Kalman filter and use that data to propagate the satellite states forward in time (see Chapter 2). Using the Kalman filter, it is estimated that the OCS could predict the satellite state vectors for at most two weeks without an update in information [30] (although with a degradation in accuracy). Consequently for this simulation to mirror reality, the use of a Kalman filter and a longer outage time period would be necessary to simulate the real effects of an outage. However, the results of this simulation do demonstrate that TDOAs could be used to aid a filter in the maintenance of a reasonable SISRE level for the GPS constellation.

4-32

As with previous tests, the results of each scenario, embodied in their respective SISRE$_{constellation}$ value, were checked against their corresponding $\sigma_{constellation}$ estimates. Figure 4.14 plots the $\sigma_{constellation}$ values for the three sets of scenarios as a function of the outage times.
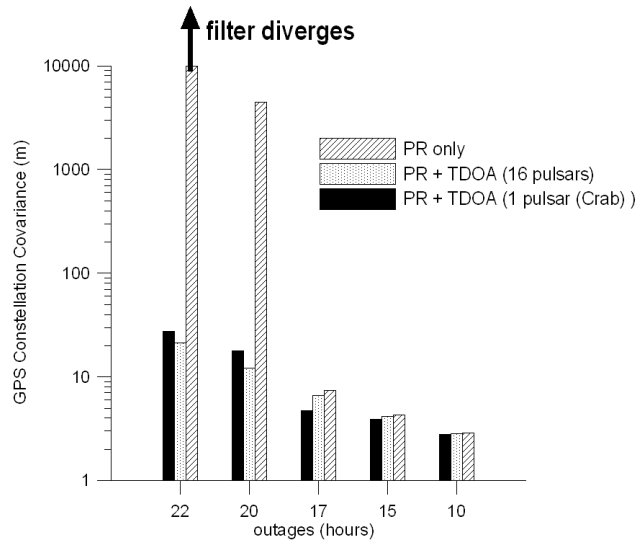
Figure 4.14:   Comparison of 4-state (position and bias) $\sigma_{constellation}$ values during GPS Ground Station Outages. Scenarios 3a, 3b, 3c, 3d, 3e represent PR-only outages of 22 hrs, 20 hrs, 18 hrs, 15 hrs, 10 hrs respectively. Scenarios 3f, 3g, 3h, 3i, 3j represent PR + TDOA outages (16 pulsars) of 22 hrs, 20 hrs, 18 hrs, 15 hrs, 10 hrs respectively. Scenarios 3k, 3l, 3m, 3n, 3o represent PR + TDOA outages (Crab Pulsar) of 22 hrs, 20 hrs, 18 hrs, 15 hrs, 10 hrs respectively.

One interesting result of this comparison is that at outage values of 20 and 22 hours, the scenarios using 16 pulsars seemed to have a lower estimate uncertainty than the scenarios that used 1 pulsar. However, at outage values of 10, 15, and 17 hours scenarios using 1 pulsar had the lower $\sigma_{constellation}$ values. One possible explanation for this phenomenon is that at a certain outage threshold, the GPS constellation needs the benefit of variable pulsar positions which in turn add more TDOA measurements to maintain observability. This result seems to indicate that in the event of a long PR outage, a geometry of multiple pulsars may be more important than the strong

timing characteristics of one pulsar. The reason for this behavior may be that in the scenarios using 16 pulsars, the filter is benefiting more from the information gathered via the dispersed TDOA geometry. Over time, a variable geometry may be more important to maintaining constellation observability. Another possible explanation is that there are along-track and cross-track data biases that are deweighted in the SISRE equations, so consequently they would not show up in the $\text{SISRE}_{constellation}$ results. However these biases may be appearing in $\sigma_{constellation}$ because they receive equal weighting compared to the radial error and the clock bias.

4.6   Test 4: Pulsar Geometry and TDOA Transmitter Experiment

The final experiment attempted to optimize the decrease in SISRE by analyzing possible pulsar geometries that could minimize SISRE levels. However, two factors obviated the need for this test to be conducted as originally stated.

First, the test conducted in Section 4.4 indicated that numerous pulsars were not needed to dramatically decrease SISRE levels. The most significant contributing factor that leads to a decline in SISRE seems to be σ_{TOA}, the accuracy to which a detector can measure pulsar pulses. The σ_{TOA} directly contributes to the accuracy of the TDOA which indicates that SISRE decrease is directly related to an increase in TDOA accuracy. With moderate (≈ 13.4 m) or better accuracies in measuring 1 pulsar, the results are very competitive to measuring 16 pulsars with nominal (≈ 40 m) or worse accuracies. Therefore, unless several pulsars are able to be detected to an equivalently accurate degree (which seems unlikely because of individual pulsar traits such as HWHM, flux,etc.), there is no need to augment the observation geometry.

Additionally, research of the pulsar RA/Dec positions reveals that the 16 pulsars used were already in a favorably diverse geometry. Figures 4.15 and 4.16 display the pulsar RA and Declination coordinates of each pulsar respectively. The figures indicate that on the RA axis the pulsar are well spread around the Earth. In terms of declination, there are a desired equal number of pulsars above and below the ecliptic (Declination = 0 deg).
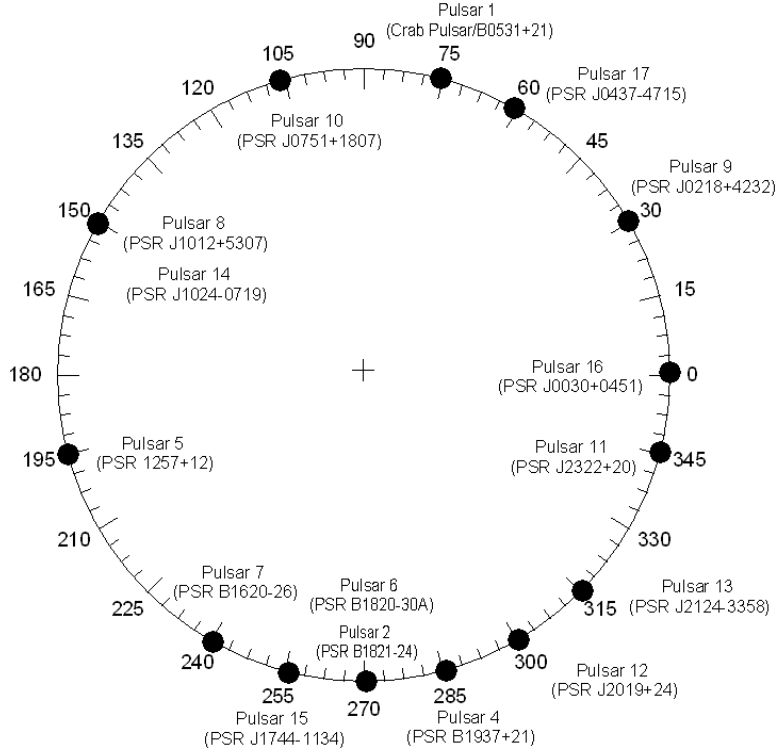
Figure 4.15:   Pulsar Right Ascension Coordinates (deg)

It is for these reasons that the last experiment was ultimately modified to simulate the TOA accuracies that may be engineered for man-made transmitters closer to Earth. These artificial transmitters were all given the measurement accuracy of typical simulated pseudoranges (1.05 m). Scenarios 4a – 4c simulated 3 variable geometry case studies. The purpose of these studies was to observe the effects of obtaining TDOA measurements on several separate axes and determining their corresponding effect on SISRE$_{constellation}$ values. The goal of the experiment was to be able to isolate the effects of TDOAs on the errors in separate dimensional planes (ECI based X, Y, Z) based on placing TDOA transmitters in different spacial orientations.

As a baseline, the three TDOA transmitters were first placed within 5 degrees of each other (scenario 4a). It was postulated that this geometry would be the most unfavorable because all of the TDOAs obtained would produce duplicated information about the relative distances between satellites. Next the transmitters were placed on the ecliptic at 120 degree increments (RA = 0 deg, 120 deg, 240 deg) around

Plot of Pulsar Declination Coordinates
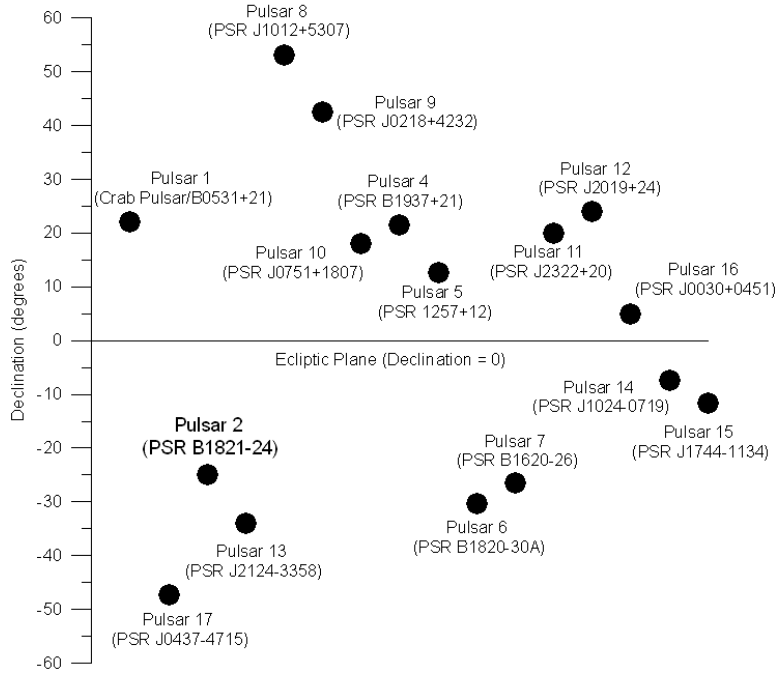
Figure 4.16:   Pulsar Declination Coordinates (deg)

the earth (scenario 4b). In scenario 4c, the transmitter's were placed in orthogonal positions with respect to the center of the earth. Two transmitters were placed on the ecliptic at 90 degrees apart in terms of their RA. The third transmitter was placed at a declination of 90 degrees (above the North pole). It is important to note that the geometry which stationed a transmitter at a declination of 90 degrees (above the North Pole) is operationally infeasible but serves to show the effects of multiplanar TDOAs on a batch estimation problem. It was predicted that the most favorable geometries would be the ones where the three transmitters were orthogonal because TDOA information was being supplied in two dimensions thus giving the filter additional data for satellite estimations.

Figure 4.17 shows the results of these 3 scenarios as a bar chart. Surprisingly, the best overall geometry seemed to be a planar 120 degree geometry in terms of which geometry yielded the lowest relative $SISRE_{constellation}$.
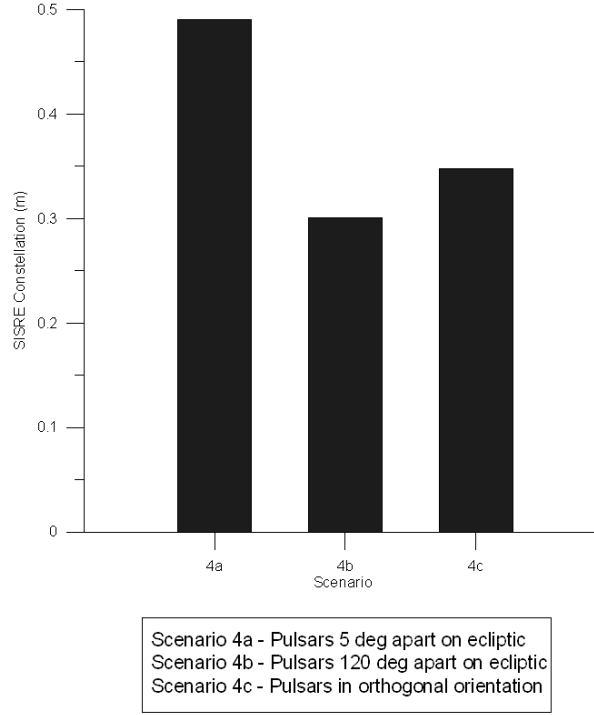
Figure 4.17:   Plot of SISRE$_{constellation}$ values for Scenarios 4a - 4c. TDOA Transmitter Locations (RA/Dec) (deg): Scenario 4a (0/0; 5/0; 355/0), Scenario 4b (0/0; 120/0; 240/0), Scenario 4c (0/0; 90/0; 0/90).

To further verify the optimal effects of having 3 transmitters 120 degrees apart, the errors (estimate - truth) in the ECI frame were calculated for each scenario's geometry. An attempt was made to correlate the differing ECI positions of the TDOA transmitters with an improvement or degradation in the errors for the X, Y, and Z ECI axes. The position of each of the transmitters was first rotated to the ECI frame. Subsequently, the errors in the X, Y, Z axes were calculated in order to be directly compared to one another.

Table 4.8 depicts the errors for each axis for each scenario along with the percent improvement of scenarios 4b and 4c over the baseline scenario 4a. Theoretically, because scenario 4b had the lowest SISRE, the errors in X, Y, and Z should also be the lowest out of all the scenarios.

Table 4.8:   Errors Along X, Y, and Z Axes (ECI) and Percent
Improvements over Scenario 25

Scenario	X Error (Constellation RMS)	X-Axis % Improvement	Y Error (Constellation RMS)	Y-Axis % Improvement	Z Error (Constellation RMS)	Z-Axis % Improvement
4a	0.327 m	-	0.326 m	-	0.389 m	-
4b	0.030 m	90.9	0.023 m	92.9	0.035 m	89.3
4c	0.171 m	47.7	0.210 m	35.8	0.139 m	57.5

As predicted, the data in Table 4.8 shows that on each axis, Scenario 4b (each trans-mitter 120 degrees apart) allows the batch filter to better estimate the positions of each GPS satellite better than any other geometry.

The covariance estimates, $\sigma_{constellation}$, for each of the five variable geometry scenarios corroborated the results of Figure 4.17 and Table 4.8 above. Table 4.9 lists the $\sigma_{constellation}$ values. The lowest $\sigma_{constellation}$ value came from scenario 4b which correspondingly had the lowest SISRE$_{constellation}$ value. It is important to note that scenarios 4a – 4c were run in a separate random seed environment than the scenarios for Tests 1 – 3. Therefore these SISRE$_{constellation}$ values should not be compared to the previous tests. The relative SISRE$_{constellation}$ differences between the scenarios of this test are the important factors of these results.

Table 4.9:   Comparison of $\sigma_{constellation}$ Values for Scenarios 4a
– 4c

	Scenario 4a	Scenario 4b	Scenario 4c
$\sigma_{constellation}$	0.209 m	0.063 m	0.069 m

The results above came as a surprise during analysis, because it was initially pos-tulated that the GPS constellation would benefit more from a 3-dimensional TDOA geometry than from TDOAs only garnered in a single plane. Scenario 4c, which placed a transmitter on an orthogonal axis, was thought to be superior to scenarios 4a and 4b because additional information from another dimension was being supplied to the filter. However, the results show that a planar 120 degree geometry is preferred to all geometries tested because of its relatively low SISRE$_{constellation}$ and $\sigma_{constellation}$.

One possible explanation is that an orthogonal (North pole) transmitter actually contributes less to the GPS constellation because as the GPS satellites orbit with an inclination of 55 degrees, the orthogonal transmitter periodically loses visibility with the satellites in their orbit and thus the filter is forced to estimate state vectors with less information.

The results however, do seem to indicate that a one-to-one correlation cannot be drawn between errors on one specific axis and the addition of TDOAs in that direction. The 120 degree geometry may be better because it is feeding the filter information it needs to solve the entire network estimation problem more accurately. If all of the different estimated parameters are correlated then each TDOA measurement cannot be treated as an independent measurement. Every parameter is affected when any knowledge about the states is obtained through the addition of TDOA measurement information. Ultimately, because every parameter is being estimated at once, the network cannot be easily dissected to analyze one specific attribute.

4.7 Summary

This Chapter presented the results and analysis of the simulation. Accuracy metrics SISRE$_{satellite}$, SISRE$_{constellation}$, and estimate covariance, $\sigma_{constellation}$, were introduced. Next simulation initial conditions and overall simulation assumptions were discussed. The basic structure of a simulation scenario was then described. Next, the use of Matlab's® pseudo-random number generator was explained. Finally, the results and analysis from Tests 1 – 4 was presented. Chapter 5 will summarize the results of this chapter and make recommendations for further research.

V. Conclusions and Recommendations

This chapter summarizes the research results of the navigation potential of pulsar-based TDOAs. Following this, future algorithm development and testing is recommended to further explore using pulsars and TDOAs to increase the accuracy of GPS satellite orbit determination methods.

5.1 Summary of Results

This section summarizes the test results presented in Chapter IV. Analysis results will be presented according to the research objectives stated in Chapters 1 and 3.

- **Quantify impact of using pulsars to decrease the GPS SISRE to levels lower than pseudorange-only based SISREs**

  Test 1 demonstrates that TDOAs, based on pulsar x-ray observations, can lower the SISRE of the GPS constellation as a whole. Individual $\mathrm{SISRE}_{satellite}$ values displayed a variability that made it difficult to ascertain SISRE improvement on a satellite-by-satellite basis. $\mathrm{SISRE}_{satellite}$ values appear to be functions of the number of random seed samples used. Therefore overall SISRE improvement was based on $\mathrm{SISRE}_{constellation}$.

  Results indicate that a marginal $\mathrm{SISRE}_{constellation}$ improvement 1.03% can be achieved if the x-ray detector is accurate to an order of 40 m. Test 1 results also indicate that increasing the accuracy of the x-ray detector is an effective way to lower GPS constellation SISRE. For example, detectors with accuracies on the order of 0.4 m yielded a percent improvement of 25.9% over the pseudorange-only based GPS system.

- **Conduct a tradeoff study to determine how many pulsars are needed to make pulsar measurements a significant contributor to SISRE decrease**

The results of Test 2 illustrate that the magnitude of the SISRE for the GPS constellation is driven by the pulsar with the strongest timing statistics (i.e., lowest σ_{TOA}). SISRE$_{constellation}$ values remained essentially unchanged when the number of pulsars used to create TDOAs was successively paired down from 16 pulsars to 1 pulsar. This is due to the fact the strongest pulsar (combination of low pulse period and highest flux) had a σ_{TOA} that was, at times, orders of magnitude lower than the any other pulsar. The disparity in σ_{TOA} magnitude caused its resultant TDOA observations to dominate in the batch filter. The value of the SISRE$_{constellation}$ for the scenarios in Test 2 varied marginally, ranging from 0.916 m (16 pulsars) to 0.911 m (1 pulsar). It may be possible to infer from this experiment that using only one pulsar, which can be very accurately timed, may be equivalent to or better than using tens of pulsars with very weak timing statistics.

- **Analyze possible advantages of using pulsars in certain galactic geometries in the attempt to decrease the SISRE**

A plot of the Right Ascension/Declination coordinates of the 16 pulsars used in the simulation illustrated a pulsar geometry that was equally spread around the Earth as well as evenly dispersed above and below the ecliptic (declination = 0 deg). Therefore the results of Test 3 show that adding 15 faint (combination of high pulse period and low flux) pulsars to the TDOA geometry of 1 accurately timed pulsar does not aid in lowering SISRE.

Test 4 investigated the effects of multiplanar TDOAs on the behaviors of the GPS constellation X, Y, Z errors. Multiplanar TDOAs were generated by artificially placing 3 transmitters at various geometries around the Earth. Analysis of the results indicate that 3 transmitters placed at 120 deg increments (RA/Dec (deg): 0/0, 120/0, 240/0) around Earth's ecliptic created optimal geometry conditions (i.e., lowest SISREs and X, Y, Z errors) when compared to putting 3 transmitters in orthogonal directions with respect to the Earth.

- **Study the use of pulsars measurements in the absence of pseudoranges**

  Test 3 investigated the utility of using TDOAs to maintain GPS SISRE$_{constellation}$ values in the absence of pseudoranges for $10 - 22$ hours in a 24 hour simulation. The results indicate that using TDOAs in the absence of pseudoranges for a limited amount of time may aid the OCS in keeping track of the GPS satellites until the ground station links to the constellation can be reestablished. Scenarios in which pseudorange outages were supplemented with TDOAs from 16 pulsars versus scenarios in which no observations were available were compared. The TDOA supplemented scenarios showed improvements of greater than 100% (22 hours) to 1.6% (10 hours) over their no-observation scenario counterparts. Preliminary analysis shows that when 16 pulsars are used to create TDOAs (accurate to, at best, 40 m), the benefits of using TDOAs is more evident when outages are 20 hours or more. Additionally, Test 3 results corroborated the results of the parametric study conducted in Test 2 concerning the number of pulsars needed to achieve SISRE improvements. Test 3 also illustrated that using 1 pulsar with moderate timing accuracy statistics (≈ 8 m), can achieve SISRE levels as good as or better than the SISRE magnitudes observed using 16 pulsars with nominal timing statistics (≈ 40 m).

5.2 Future Work

The future work recommendations are divided into two sections: (1) simulation/algorithm development, and (2) system testing. Each of these are discussed below

5.2.1 Recommendations for Future Work.   After developing and analyzing the results, many suggestions for improving the system and expanding the research are available. The two primary goals of simulation development should be to produce SISRE values that approximate operational SISRE results and to create pulsar models

that are more consistent with their observed characteristics. The principal areas requiring additional development are:

- Incorporate Ground Station Clocks in Estimation Model
- Implement a Kalman Filter in Estimation Algorithm
- Improved Error Model
- Improved Pseudorange observation algorithm
- Improved TDOA observation algorithm
- Substitute HWHM approximation for real measured values

- **Incorporate Ground Station Clocks in Estimation Model**

  Incorporating ground station clocks into the batch filter would fundamentally change the estimation problem of this research. Operationally, the ground station clocks are estimated by the filter because they are not assumed to be perfect. Therefore, in order to more closely approximate reality, the satellite position, velocity and clock states must be estimated simultaneously with the clock states of each ground station.

- **Implement a Kalman Filter in Estimation Algorithm**

  As discussed in Chapter 2, there are fundamental differences between the batch filter used in this simulation and the sequential Kalman filter used by the OCS. One advantage of using a Kalman filter to estimate the states of the GPS satellites is that a Kalman filter can use information from past estimates to formulate a more accurate current estimate. Using a Kalman filter in this simulation would allow the SISRE results, especially those results found in the outage scenarios of Test 3, to more closely depict reality.

- **Improved Error Model**

  Two separate areas of the simulation that would benefit from more accurate error models are the orbit propagator algorithm and the operational pseudorange generator algorithm. This simulation implemented an error-free 2-body orbit propagator which does not closely align with reality. Ideally, in order to generate

operational-like SISREs, the simulation would implement an error model that approximated error growth on the order of that observed by the OCS's Kalman filter. However, this does not mean that every deterministic error accounted for by the OCS Kalman filter should be modeled. Instead, this simulation should strive to model the stochastic errors (e.g., y-axis bias, etc.) that must be approximated by the Kalman filter. It is recommended that the magnitude of these small stochastic errors be approximated by first implementing an Earth geopotential model (e.g., EGM96) in the truth model's orbit propagator. Next, a truncated geopotential model should be incorporated into the batch filter which would simulate an imperfect approximation of the truth model's geopotential. The amount of truncation between the truth model and batch filter could be set to approximate the combined magnitude of all the stochastic force accelerations experienced by each GPS satellite.

Additionally, the real multipath and receiver errors observed by the OCS and GPS receivers will tend to be time-correlated. The multipath and receiver errors modeled in this simulation did not account for this time correlation. In order to produce pseudorange observations that closely resemble real pseudoranges, the time correlation nature of these errors should be modeled.

- **Improved Pseudorange observation algorithm**

  In order to create more realistic pseudorange observations, W, the the measurement weighting matrix, will need to be modified. In this simulation, all pseudorange observations were given equal weighting. In reality, the pseudoranges measured at low-elevations will generally have larger errors associated with them because the signals must propagate through a larger volume of atmosphere [30]. Therefore, it is recommended that the batch filter be modified to account for the elevation-dependent accuracy of the measured pseudoranges using a varied weighting scheme in the W matrix.

- **Improved TDOA observation algorithm**

In order to create more realistic TDOA observations, R, the measurement covariance matrix, will need to be modified. There is a correlation between TDOA measurements at a given epoch, because they all share the same base satellite. This will lead to cross-correlation terms in the R matrix. These cross-correlations were not accounted for in the current simulation.

Additionally, the a new visibility scheme will need to be generated in order to generate TDOAs using man-made transmitters situated around the Earth. The pulsar visibility scheme assumed infinite distance with respect to the MEO altitude GPS satellites. Transmitters possibly stationed in a geosynchronous or cislunar orbit could not make the infinite distance assumption. Therefore, the total number of TDOA observations could vary because of Earth blockage of TDOA signals.

- **Substitute Pulsar *HWHM* Approximations for Real Measured Values**

The *HWHM* for each pulsar was approximated in this simulation as a fraction of the pulse period. In reality, each pulsar has a naturally occurring *HWHM* that can be measured. The ability of this simulation to model an operational x-ray detector was limited by the *HWHM* approximations for each pulsar. In order to achieve more realistic detector σ_{TOA} values, it is recommended that real (measured) pulsar *HWHM* values be used.

5.2.2 System Testing. This section outlines additional testing to further research presented in this Thesis. The four main areas to expand upon are:

- Using Black Holes as x-ray Transmitters
- Using Earth Orbiting Satellite Assets as TDOA signal transmitters
- X-ray/TDOA Detector Development

- **Using Black Holes as X-ray Transmitters**

An alternative to using pulsar-based x-ray signals to generate TDOAs would be to use x-ray signals from black hole sources to create TDOA observations.

X-ray signals from black holes are typically aperiodic (as opposed to the period signals from pulsars), which because of signal cross-correlation, is advantageous for creating TDOAs between two detectors.

- **Using Earth Orbiting Satellites as TDOA Signal Transmitters**

A feasibility study should be conducted to ascertain the advantages of using man-made Earth orbiting satellites to create TDOA observations. The preliminary results of this simulation indicate that the majority of the pulsars are too faint to create useable TDOAs using a detector that could feasibly be attached to a GPS satellite. However, this simulation could be modified to simulate signal transmitters in an Earth orbit (e.g., geosynchronous). Using transmitters closer to the GPS constellation would be advantageous because it is theorized that the detector used to generate those TDOA measurements would be much smaller than the x-ray detector necessary for pulsar-based TOAs. Using current technology, it is reasonable to assume that satellites designed for another mission (e.g., communication assets, etc.) could be outfitted with the ability to transmit signals that are engineered to be specifically used by GPS in the event of a complete ground station black out. These assets could have other primary missions. However, in times of emergency or, if increased user accuracy was desired, these satellite assets could activate a TDOA-optimal signal for use by the GPS satellites. These signals, which could be engineered to have the accuracy of pseudoranges (on the order of 1 m), have already been proven by this study to be of great help in lowering SISRE for the constellation.

- **X-ray/TDOA Detector Development**

Once the simulation is able to duplicate operational SISREs and more closely model the observed characteristics of pulsars, an engineering tradeoff study should be performed to determine realistic specifications of an x-ray detector that could be attached to a GPS satellite. Engineering tradeoffs would need

to be made primarily between the size of the detector and its desired accuracy based on the σ_{TOA} equation presented in Chapter 2.

Appendix A. GPS Satellite State Vectors

This section provides the complete set of initial state vectors for the 29 GPS satellites.

Table A.1: Position State Components at Epoch for PRN's 1
– 15

PRN	X	Y	Z
1	2817.521102	-14600.538964	22163.008123
3	15163.432538	-12009.542515	-18197.696199
4	-15779.438286	32.367963	21414.987878
5	-1474.333893	21346.885766	15705.286273
6	18952.219524	13222.464156	13406.318497
7	-26071.606507	60.179616	4991.986472
8	-16528.978241	-9478.738892	-18831.610277
9	4451.485543	25535.991272	-7077.597942
10	-16406.899639	20589.003872	-2154.792449
11	-6778.025885	-25085.884478	-5867.707499
13	-20551.854149	-12043.745365	11612.646062
14	26172.201547	2426.408289	3820.913833
15	15631.122714	394.877520	-21712.264618

Table A.2:   Position State Components at Epoch for PRN's 16 – 31

PRN	X	Y	Z
16	19244.837556	-17830.655909	4120.080050
17	-4004.020865	23364.107861	12937.663667
18	12485.425474	8739.659561	-21699.744876
19	2249.602308	-15064.534421	-21647.310638
20	445.290781	-19602.246117	17836.842472
21	15097.643462	17588.509224	-13374.791316
22	19597.856243	-2588.164317	-17591.472699
23	-7016.355234	-15688.425837	20170.572099
24	-10496.446586	13903.582011	20325.899433
25	14520.404147	-6013.661410	21782.964897
26	-5957.461092	13835.571622	-22114.177069
27	-15961.606040	-18158.503959	-11019.087448
28	-19314.701391	3226.249962	-17590.172237
29	-11168.355879	12096.628220	-20565.654235
30	8445.437509	13677.054742	20920.732062
31	-26152.308981	-5240.775579	-2167.289626

Table A.3:   Velocity State Components at Epoch for PRN's 1 – 15

PRN	$\dot{X}$	$\dot{Y}$	$\dot{Z}$
1	2.705497	0.594387	0.045711
3	2.272755	0.470713	1.616071
4	-0.793714	-2.594449	-0.549807
5	-1.394713	1.479347	-2.105884
6	-1.692515	-0.011693	2.428269
7	-0.532314	-0.435636	-3.045444
8	-0.577047	-2.268929	1.632951
9	-0.534676	-0.684044	-2.964383
10	-0.359544	0.038434	3.220130
11	0.702129	0.495344	-2.917111
13	1.489672	0.115122	2.748301
14	0.428398	0.309150	-3.166256
15	0.660545	2.620088	0.500756

Table A.4:   Velocity State Components at Epoch for PRN's 16 – 31

PRN	$\dot{X}$	$\dot{Y}$	$\dot{Z}$
16	-0.127125	0.569511	3.121224
17	-0.484726	-1.509850	2.544852
18	-1.878071	2.030136	-0.286573
19	2.697643	0.652678	-0.179250
20	1.601396	-1.630301	-1.824455
21	0.270276	1.671101	2.464245
22	-1.453246	1.744332	-1.857164
23	2.555730	0.382223	1.171314
24	-0.795540	-2.387291	1.248499
25	1.086379	2.454604	-0.046689
26	-2.672138	-0.599707	0.408375
27	-0.324558	-1.445427	2.681290
28	1.372630	-1.839101	-1.854208
29	-2.613872	-0.534806	1.100780
30	-1.761783	2.068776	-0.623240
31	0.277164	-0.293466	-3.083186

Table A.5:   Bias and Drift State Components for PRN's 1 – 15

PRN	af_0	af_1
1	3.5858154300e-004	3.6379788070e-012
3	3.5285949710e-005	3.6379788070e-012
4	-2.5177001950e-004	-1.4551915230e-011
5	4.3869018550e-005	3.6379788070e-012
6	3.6525726320e-004	3.2741809260e-011
7	4.0817260740e-004	-2.1827872840e-011
8	-6.6757202150e-006	0.0000000000e+000
9	-5.9127807620e-005	-3.6379788070e-012
10	4.8637390140e-005	0.0000000000e+000
11	1.4114379880e-004	3.6379788070e-012
13	-2.3841857910e-005	0.0000000000e+000
14	-2.4795532230e-005	0.0000000000e+000
15	3.0612945560e-004	3.6379788070e-012

Table A.6:   Bias and Drift State Components for PRN's 16 – 31

PRN	af_0	af_1
16	7.6293945310e-006	0.0000000000e+000
17	-1.2493133540e-004	-1.0913936420e-011
18	-6.4849853520e-005	-3.6379788070e-012
19	-1.2397766110e-005	3.6379788070e-012
20	-1.3256073000e-004	3.6379788070e-012
21	7.8201293950e-005	0.0000000000e+000
22	1.6212463380e-005	0.0000000000e+000
23	1.4686584470e-004	1.0913936420e-011
24	4.9591064450e-005	3.6379788070e-012
25	7.3432922360e-005	0.0000000000e+000
26	1.9264221190e-004	1.4551915230e-011
27	3.6430358890e-004	1.8189894040e-011
28	4.0054321290e-005	0.0000000000e+000
29	3.6716461180e-004	-7.2759576140e-012
30	5.5503845210e-004	0.0000000000e+000
31	2.8991699220e-004	1.0913936420e-011

Appendix B.   Pulsar Flux Calculation

Figure B.1 displays a table of pulsars from reference [36]. The ninth column lists the pulsar flux in units of $ergs/cm^2/s$. PSR J0030+0451's energy based flux of 1.27×10^{-13} $ergs/cm^2/s$ can be converted to a photon-based flux with the following procedure.

1. First find the Observation Band (Obs Band) used by the detector to measure the flux. The Obs Band is the energy band of the observation from which the fluxes are calculated [36]. Because there are a range of values for the Obs Band nominal value must be chosen. It is common practice to choose a value near the lower end of the Obs Band because most photons reside in the lower end of the energy spectrum because at higher energies, the photons are absorbed by the interstellar medium, etc. [38]. For this sample calculation .5 $keV/photon$ will be used. The Obs Band value must now be converted into units that are compatible with the energy based flux value of 1.27×10^{-13} $ergs/cm^2/s$. Using the standard energy conversion factor of 1.6×10^{-9} $ergs/keV$ the Obs band is converted.

$$.5keV/photon \cdot 1.6 \times 10^{-9}ergs/keV = 8 \times 10^{-10}ergs/photon \qquad \text{(B.1)}$$

2. Next use the converted Obs Band value to convert the pulsar flux into $photons/cm^2/s$.

$$\frac{1.27 \times 10^{-13}ergs/cm^2/s}{8 \times 10^{-10}ergs/photon} = 1.59 \times 10^{-4}photons/cm^2/s \qquad \text{(B.2)}$$

An analogous procedure is followed when the flux value was not available and only the pulsar's luminosity was listed. The luminosity of a pulsar indicates how much energy is emitted from the source over a given amount of time. The units of luminosity are typically expressed as $ergs/s$. In order to glean a value of flux, $ergs/s$ must be converted to $ergs/cm^2/s$ and subsequently to $photons/cm^2/s$ for the detector. Figure B.2 displays Table 1.1 from [51]. Column 8 displays the pulsed luminosity for

Table 1. Parameters and emission of the 41 sample pulsars.

Pulsar PSR	P ms	$\dot{P}$ 10^{-15} s s^{-1}	$N_{\rm H}$ 10^{21} cm^{-2}	distance kpc	α or kT keV	Obs Band keV	Detector	$f^{(2-10)}$ erg s^{-1}cm^{-2}	$\log L_X^{(2-10)}$ erg s^{-1}	ref
J0030+0451	4.87	1.00×10^{-5}	2.15 ± 0.85	0.230 ± 0.092	2 ± 0.2	0.1–2.4	PSPC	$(1.27^{+0.95}_{-0.61})\times10^{-13}$	$29.88^{+0.54}_{-0.73}$	1
J0218+4232	2.32	7.50×10^{-5}	2 ± 2	5.70 ± 2.28	0.94 ± 0.22	2.0–10.0	MECS	$(4.30^{+0.28}_{-0.22})\times10^{-13}$	$33.20^{+0.32}_{-0.47}$	2
J0437−4715	5.76	1.86×10^{-5}	$0.8^{+1}_{-0.6}$	0.178 ± 0.026	2.35 ± 0.35	0.1–2.4	HRI	$(4.30^{+1}_{-1})\times10^{-13}$	$30.19^{+0.21}_{-0.25}$	3,4
J0751+1807	3.48	8.00×10^{-6}	$4.4^{+4.6}_{-0.4}$	2 ± 0.8	2 ± 0.2	0.1–2.4	PSPC	$(4.29^{+3.54}_{-1.44})\times10^{-14}$	$31.29^{+0.55}_{-0.62}$	3
J1012+5307	5.26	1.46×10^{-5}	0.06 ± 0.01	0.520 ± 0.208	2.3 ± 0.2	0.1–2.4	PSPC	$(1.25^{+0.89}_{-0.61})\times10^{-14}$	$29.58^{+0.53}_{-0.73}$	3
J1024−0719	5.16	2.99×10^{-6}	0.2 ± 0.05	0.350 ± 0.140	2 ± 0.2	0.1–2.4	HRI	$(8.86^{+4.70}_{-3.36})\times10^{-15}$	$29.09^{+0.50}_{-0.79}$	3
J1744−1134	4.07	7.13×10^{-6}	0.1 ± 0.05	$0.357^{+0.043}_{-0.035}$	2 ± 0.2	0.1–2.4	HRI	$(6.44^{+4.08}_{-2.86})\times10^{-15}$	$28.97^{+0.32}_{-0.40}$	3
B1821−24	3.05	1.62×10^{-3}	2.9 ± 2.3	5.1 ± 0.5	1.89 ± 0.21	0.7–10.0	GIS	$(1.25^{+0.33}_{-0.69})\times10^{-12}$	$33.56^{+0.18}_{-0.44}$	5
B1937+21	1.56	1.06×10^{-4}	21 ± 5	3.60 ± 1.44	$1.71^{+0.05}_{-0.08}$	0.5–10.0	LECS+MECS	$(3.70^{+0.40}_{-0.40})\times10^{-13}$	$32.73^{+0.39}_{-0.55}$	6
J2124−3358	4.93	1.30×10^{-5}	0.35 ± 0.15	0.25 ± 0.10	2 ± 0.2	0.1–2.4	HRI	$(8.26^{+0.45}_{-3.48})\times10^{-14}$	$29.77^{+0.32}_{-0.68}$	7
B0950+08	253.07	0.229		0.127 ± 0.013		0.1–2.4	PSPC	$(2.3^{+0.7}_{-0.7})\times10^{-14}$	$28.62^{+0.42}_{-0.62}$	3
B1929+10	226.52	1.16	0.1 ± 0.05	0.25 ± 0.08	0.44 ± 0.046 [c]	0.5–5.0	SIS	$(5.6^{+1.5}_{-1.4})\times10^{-14}$	$29.60^{+0.34}_{-0.46}$	8
B0823+26	530.66	1.71		0.380 ± 0.152		0.1–2.4	PSPC	$(0.6^{+0.2}_{-0.2})\times10^{-14}$	$28.99^{+0.42}_{-0.62}$	3
B0114+58	101.44	5.85	2.57 ± 0.2	2.14 ± 0.856	2.1 ± 0.2	0.1–2.4	PSPC	$(4.25^{+4.25}_{-0.77})\times10^{-15}$	$30.34^{+0.59}_{-0.77}$	9
B0355+54	156.38	4.40	0.2 ± 0.2	2.10 ± 0.84	2 ± 0.5	0.1–2.4	PSPC	$(1.16^{+3.04}_{-0.94})\times10^{-13}$	$31.76^{+0.59}_{-1.17}$	10
J0538+2817	143.16	3.67	0.6 ± 0.6	1.5 ± 0.6	1.5 ± 0.5	0.1–2.4	PSPC	$(8.00^{+8.00}_{-0.77})\times10^{-16}$	$29.31^{+0.59}_{-0.77}$	11
B0633+17	237.09	11.0	0.13 ± 0.13	$0.154^{+0.059}_{-0.034}$	2.19 ± 0.35	0.7–5.0	GIS	$(7.94^{+3.0}_{-2.2})\times10^{-14}$	$29.33^{+0.42}_{-0.36}$	12
B0656+14	384.89	55.0	0.17 ± 0.17	$0.28^{+0.20}_{-0.10}$	1.5 ± 1.1	1.0–5.0	SIS	$(2.05^{+1.72}_{-0.74})\times10^{-13}$	$30.26^{+0.73}_{-0.58}$	13
B1055−52	197.11	5.83	0.26 ± 0.06	0.5 ± 0.2	1.5 ± 0.3	2.0–10.0	GIS	$(1.06^{+0.10}_{-0.09})\times10^{-14}$	$29.48^{+0.33}_{-0.48}$	14
B1951+32	39.53	5.84	3.4 ± 0.5	2.5 ± 0.2	2.1 ± 0.3	0.1–2.4	PSPC	$(2.04^{+0.85}_{-0.79})\times10^{-12}$	$33.16^{+0.22}_{-0.28}$	15
B0833−45	89.33	1.25×10^2	0.4 ± 0.1	0.25 ± 0.03	2.2 ± 0.4	0.2–8.0	ACIS-S	$(1.03^{+1.04}_{-0.55})\times10^{-11}$	$31.86^{+0.40}_{-0.44}$	16
B1046−58	123.67	96.3	5 ± 1	2.98 ± 1.19	2 ± 0.2	0.4–10.0	SIS	$(2.50^{+0.66}_{-0.58})\times10^{-13}$	$32.40^{+0.39}_{-0.56}$	17
J1105−6107	63.19	15.8	8.55 ± 5.25	7.0 ± 2.8	1.8 ± 0.4	2.0–10.0	GIS	$(6.47^{+1.18}_{-1.04})\times10^{-13}$	$33.55^{+0.37}_{-0.52}$	18
J1420−6048	68.18	83.2	22 ± 7	2.0 ± 0.8	1.6 ± 0.4 [b]	2.0–10.0	GIS	$(4.70^{+0.77}_{-0.74})\times10^{-12}$	$33.33^{+0.36}_{-0.52}$	19
B1706−44	102.46	93.0	3.45 ± 3.45	1.80 ± 0.72	1.9 ± 0.9	2.0–10.0	SIS+GIS	$(1.03^{+0.38}_{-0.24})\times10^{-12}$	$32.58^{+0.43}_{-0.56}$	20
B1757−24	124.90	1.28×10^2	35 ± 12	$5.0^{+2.0}_{-0.7}$	1.6 ± 0.6	2.0–10.0	ACIS-S	$(7.9^{+0.6}_{-0.59})\times10^{-13}$	$33.37^{+0.20}_{-0.10}$	21
B1800−21	133.63	1.34×10^2	13 ± 1	5.30 ± 2.12	2 ± 0.2	0.1–2.4	PSPC	$(1.78^{+0.70}_{-0.59})\times10^{-13}$	$32.75^{+0.45}_{-0.70}$	22
J1811−1926	64.67	44.0	13.8 ± 0.8	7.8 ± 2.5	1.89 ± 0.25	4.0–10.0	MECS	$(1.23^{+0.07}_{-0.11})\times10^{-11}$	$34.93^{+0.27}_{-0.38}$	23
B1823−13	101.45	75.5	40 ± 25	4.12 ± 1.65	2 ± 0.2	0.5–2.4	PSPC	$(1.70^{+4.4}_{-1.4})\times10^{-11}$	$34.51^{+0.85}_{-1.20}$	24
B1853+01	267.40	2.08×10^2	2.57 ± 0.2	3.2 ± 1.3	2.3 ± 1.1	0.4–2.0	GIS	$(1.2^{+0.3}_{-0.3})\times10^{-12}$	$33.14^{+0.28}_{-0.57}$	25
J2229+6114	51.62	78.0	6.3 ± 1.3	3 ± 1	1.51 ± 0.14	2.0–10.0	ACIS-I	$(1.30^{+0.09}_{-0.08})\times10^{-12}$	$33.12^{+0.28}_{-0.38}$	26
B2334+61	495.28	1.92×10^2	2 ± 1	2.5 ± 1	2 ± 0.2	0.1–2.4	PSPC	$(4.05^{+2.6}_{-1.7})\times10^{-14}$	$31.46^{+0.52}_{-0.86}$	27
J0205+6449	65.68	1.93×10^2	3 ± 2	2.6 ± 0.6	1.9 ± 0.2 [b]	0.8–10.0	HRC	$(1.5^{+0.3}_{-0.3})\times10^{-11}$	$34.08^{+0.14}_{-0.21}$	28
B0531+21	33.52	4.21×10^2	3 ± 0.5	2 ± 0.5	2.108 ± 0.006	0.3–10.0	MOS	$(9.93^{+0.09}_{-0.43})\times10^{-9}$	$36.65^{+0.20}_{-0.27}$	29
J0537−6910	16.11	51.0	6.9 ± 3.3	47.3 ± 0.8	1.6 ± 0.2 [a] / 2.55 ± 0.15 [b]	0.2–10.0	GIS	$(5.13^{+1.38}_{-1.37})\times10^{-12}$	$36.11^{+0.12}_{-0.15}$	30
B0540−69	50.53	4.73×10^2	4.6 ± 4.6	47.3 ± 0.8	1.83 ± 0.13 [a] / 2.06 ± 0.2 [b]	0.2–10.0	ACIS-I	$(3.33^{+0.97}_{-1.29})\times10^{-11}$	$36.93^{+0.13}_{-0.23}$	31
J1119−6127	407.75	4.02×10^3	15 ± 15	5 ± 3	$1.4^{+1.0}_{-1.2}$	0.7–5.0	GIS	$(4.74^{+6.8}_{-2.7})\times10^{-13}$	$33.13^{+0.80}_{-1.16}$	32
J1124−5916	135.31	7.45×10^2	3.17 ± 0.15	4.8 ± 1.6	1.9 ± 0.2	2.0–8.0	ACIS-S	$(1.1^{+0.2}_{-0.2})\times10^{-11}$	$34.48^{+0.18}_{-0.31}$	33,34
B1509−58	150.66	1.54×10^3	12.7 ± 12.7	4.2 ± 0.5	1.358 ± 0.014 [a] / 2.2 ± 0.005 [b]	2.0–250	PCA	$(1.05^{+0.06}_{-0.33})\times10^{-10}$	$35.32^{+0.12}_{-0.27}$	35
J1617−5055	69.36	1.37×10^2	6.8 ± 6.8	4.5 ± 0.9	1.6 ± 0.3	3.5–10.0	GIS	$(8.86^{+0.49}_{-0.34})\times10^{-12}$	$34.31^{+0.18}_{-0.21}$	36
J1846−0258	323.60	7.10×10^3	47 ± 8	19 ± 5	2.2 ± 0.1	3.0–20.0	PCA	$(3.90^{+0.4}_{-0.4})\times10^{-11}$	$36.22^{+0.28}_{-0.32}$	37,38

Figure B.1:   Table of Pulsar Fluxes

Table 1.1. *Non-Thermal X-ray Detected Rotation-Powered Pulsars[a]*

PSR	P (ms)	$\dot{P}$ $(10^{-15}\,s\,s^{-1})$	d (kpc)	log(B) (G)	log(τ_c) (yr)	log($\dot{E}$) (erg s^{-1})	log(L_x)^p (erg s^{-1})	log(L_x)^t (erg s^{-1})
J1846−0258	324.00	7097.1	19	13.99	2.88	36.92	34.61	36.32
B0531+21	33.40	421	2	12.88	3.12	38.65	35.85	37.02
B1509−58	150	1536	4.3	13.49	3.21	37.26	34.60	34.80
B0540−69	50	479	49.4	13.00	3.24	38.18	36.10	36.92
J1930+1852	136	750.57	5.00	13.31	3.48	37.07	32.63	
J0537−6910	16.10	51.2	49.4	12.26	3.72	38.69	35.52	
J0205+6449	65.70	193	2.6	12.86	3.75	37.43		32.20
J1617−5055	69	140	3.3	12.80	3.91	37.23	33.48	33.76
J2229+6114	52	78.300	3	12.61	4.04	37.34		33.01
B0833−45	89	124	0.25	12.83	4.08	36.84	31.60	32.70
J1420−6048	68	83.167	7.69	12.68	4.13	37.02	34.46	
B1800−21	134	134	3.94	12.93	4.22	36.34		33.06
B1706−44	102	92.2	1.43	12.79	4.27	36.54	32.16	33.15
J1811−1926	64.70	44	5	12.53	4.39	36.81	34.39	
B1951+32	39.53	5.837	2.5	11.99	5.05	36.57		33.79
B0656+14	384	55	0.76	12.97	5.07	34.59	30.26	32.98
Geminga	237	11.4	0.16	12.52	5.54	34.53	29.56	29.79
B1055−52	197	5.8	1.38	12.34	5.75	34.48	29.48	33.42
B1929+10	226	1.15E+00	0.17	12.01	6.52	33.60	29.51	30.00
B1821−24	3	1.60E-03	5.5	9.65	7.49	36.37	31.80	33.24
B1937+21	1.55	1.00E-04	3.60	8.90	8.41	36.03	31.66	32.8
J0218+4232	2.32	7.50E-05	5.85	8.93	8.71	35.38	32.11	32.75
J0437−4715	5.75	5.70E-05	0.18	9.06	9.23	34.08	30.48	30.86
J2124−3358	4.93	1.10E-05	0.25	8.67	9.87	33.56	29.80	30.35
J0030+0451	4.86	1.00E-05	0.23	8.65	9.91	33.54	30.26	

[a] $(L_x)^p$ is pulsed, non-thermal X-ray flux and $(L_x)^t$ is total X-ray flux.

Figure B.2:   Table of Pulsar Luminosities

each pulsar. To convert luminosity into a flux, the luminosity must be divided by the surface area of a sphere to account for the photons emitted from the surface area of the pulsar arriving at the Earth.

The luminosities were converted to fluxes using a modified version for the surface area for a sphere

$$Flux = \frac{(L_x)^p}{4\pi d^2} \tag{B.3}$$

where

$(L_x)^p$ is the pulsed X-ray luminosity from a pulsar in units of *ergs/s*

d is the approximate distance from the pulsar to the Earth in units of kiloparsecs (kpc)

The distance (d) must be converted into cm to yield units of $ergs/s/cm^2$. Once the luminosity was converted into a flux value, Equations (B.1) and (B.2) were used to convert the ergs-based flux value into a photon-based flux.

Bibliography

1. ARINC Research Corporation. *ICD-200C: Navstar GPS Space Segment/Navigation User Interfaces*. Technical Report, United States Air Force, 1993.

2. Arsenault, T., "Navstar GPS Constellation Status," August 2004. Department of Geodesy and Geomatics Engineering University of New Brunswick (http://gge.unb.ca/HomePage.php3).

3. Becker, W. and J. Trumper. "The X-ray emission properties of millisecond pulsars," *Astronomy and Astrophysics*, *341*:803–817 (1999).

4. Becker, W. and J. Trumper. "X-ray emission from Isolated Neutron Stars," *Advances in Space Research*, *21*:203–211 (1998).

5. Brown, Kenneth R. "Characterizations of OCS Kalman Filter Errors." *Proceedings of the ION GPS-91*. 148–158. September 1991.

6. Brown, Kenneth R. "The Theory of the GPS Composite Clock." *Proceedings of the ION GPS-91*. 223–241. September 1991.

7. Brown, R., and P. Hwang. *Introduction to Random Signals and Applied Kalman Filtering*. New York: John Wiley and Sons Inc., 1983.

8. Chapman, Stephen. *MATLAB® Programming for Engineers*. California: Brooks/Cole, 2002.

9. Chester, T.J. and S.A. Butman. *Navigation Using X-ray Pulsars*. Technical Report, NASA, June 1981. N81-27129.

10. Codik, Andrew. "Autonomous Navigation of GPS Satellites: A Challenge for the Future," *Navigation: Journal of The Institute of Navigation*, *32*(3):221–232 (Fall 1985).

11. Conley, R. "Results of the GPS JPO's GPS Performance Baseline Analysis: The GOSPAR Project." *ION GPS-97; Proceedings of the 10th International Technical Meeting of the Satellite Division of the Institute of Navigation*. September 1997.

12. Crum, J.D., S.T. Hutsell, and R.T. Smetek. "The 2SOPS Ephemeris Enhancement Endeavor (EEE)." *Proceedings of the 29th Annual Precise Time and Time Interval (PTTI) Applications and Planning Meeting*. December 1997.

13. Cusumano, G., E. Massaro, and T. Mineo. "Timing Noise, Glitches and the Braking Index of PSR B0540-69," *Astronomy and Astrophysics*, *402* (May 2003).

14. Divine, Dwight, III and Sherman G. Francisco. "Synchromesh, A Practical Enhancement to GPS Service." *IEEE 1984 Position Location And Navigation Symposium*. 169–174. November 1984.

15. Downs, G.S. *Interplanetary Navigation Using Pulsating Radio Sources*. Technical Report, NASA, October 1974. NASA Technical Reports, N74-34150.

16. Eggert, Ryan J. *Evaluating the Navigation Potential of the National Television System Committee Broadcast Signal*. Masters Thesis, Air Force Institute of Technology, 2004.

17. Eikenberry, S.S., G.G. Fazio, S.M. Ransom, J. Middleditch, J. Kristian, and C.R. Pennypacker. "Infrared-to-Ultraviolet Wavelength-dependent Variations Within the Pulse Profile Peaks of the Crab Nebula Pulsar," *The Astrophysical Journal*, *467* (1996).

18. Halsell, Charles A. *Orbit Determination of the Global Positioning Satellite System using Inter-Satellite Range Measurements*. Masters Thesis, University of Texas at Austin, December 1984.

19. Hanson, J.E. *Principles of X-ray Navigation*. Doctoral Dissertation, Stanford University, 1996.

20. Hay, Curtis. "The GPS Accuracy Improvement Initiative," *GPS World*, 56–61 (June 2000).

21. Hutsell, Steven T. "Fine Tuning GPS Clock Estimation In The MCS." *26th Annual Precise Time and Time Interval (PTTI) Applications and Planning Meeting*. 63–74. December 1994.

22. Kaspi, V.M. "High-Precision Timing of Millisecond Pulsars and Precision Astrometry." *Astronomical and Astrophysical Objectives of Sub-Milliarcsecond Optical Astrometry*. August 1994. Proceedings of the 166th Symposium of the International Astronomical Union.

23. Kelso, T.S., "GPS Yuma Almanac." http://celestrak.com/GPS/, August 2004. http://celestrak.com/GPS/almanac/Yuma/2004/almanac.yuma.week0259.589824.txt.

24. Langley, R.B., H. Jannasch, B. Peeters, and S. Bisnath. "The GPS Broadcast Orbits: An Accuracy Analysis." *33rd COSPAR Scientific Assembly, Session B2.1-PSD1, New Trends in Space Geodesy*. July 2000.

25. Lochner, James, "The Rossi X-ray Timing Explorer Learning Center," August 2001. http://rxte.gsfc.nasa.gov/docs/xte/learning_center/index.html.

26. Logsdon, Tom. *The Navstar Global Positioning System*. New York, New York: Van Nostrand Reinhold, 1992.

27. Lorimer, D.R. *Binary and Millisecond Pulsars at the New Millenium*. Technical Report, Arecibo Observatory and Max Planck Institute for Gravitational Physics, June 2001. www.livingreviews.org/Articles/Volume4/2001-5lorimer.

28. Lyne, A.G. and F. Graham-Smith. *Pulsar Astronomy*. New York, NY: Cambridge University Press, 1998.

29. Malys, S., M. Larezos, S. Gottschalk, S. Mobbs, B. Winn, W. Feess, M. Menn, E. Swift, M. Merrigan, and W. Mathon. "The GPS Accuracy Improvement Initiative." *Proceedings of the 10th International Technical Meeting of the Satellite Division of the Institute of Navigation*. 375–384. September 1997.

30. Misra, Pratap and Per Enge. *Global Positioning System; Signals, Measurements, and Performance*. Lincoln, Massachusetts: Ganga-Jamuna Press, 2001.

31. National Research Council. *The Global Positioning System, A Shared National Asset, Recommendations for Technical Improvements and Enhancements*. Technical Report, National Academy Press, Washington D.C., 1995.

32. Northern Lights Software Associates, "http://www.nlsa.com."

33. Parkinson, B.W. and J.J. Spilker. *Global Positioning System: Theory and Applications, Volume 1*. Washington D.C.: American Institute of Aeronautics and Astronautics, Inc., 1996.

34. Parkinson, B.W. and J.J. Spilker. *Global Positioning System: Theory and Applications, Volume 2*. Washington D.C.: American Institute of Aeronautics and Astronautics, Inc., 1996.

35. Pines, Darryll, "3_Overview.pdf," August 2004. https://safe.sysplan.com/ xnav/3_Overview.pdf.

36. Possenti, A., R. Cerutti, M. Colpi, and S. Mereghetti. "Re-examining the X-ray versus spin-down luminosity correlation of rotation powered pulsars," *Astronomy and Astrophysics*, *387*:993–1002 (2002).

37. Raquet, John and David L.M. Warren. "Broadcast vs. Precise GPS Ephemerides: A Historical Perspective," *GPS Solutions* (2003).

38. Ray, Paul, "Telephone Conversations and Meetings with the Naval Research Laboratory." Naval Research Laboratory.

39. Ray, Paul and M. Wolff, "The USA Experiment," July 2004. http://xweb.nrl.navy.mil/usa/.

40. Ray, P.S., K.S. Wood, M.T. Wolff, M.N. Lovellette, S. Sheikh, D.S. Moon, S.S. Eikenberry, M. Roberts, A. Lyne, C. Jordan, E.D. Bloom, D. Tournear, P. Saz Parkinson, and K. Reilly. "Absolute Timing of the USA Experiment Using Pulsar Observations." *American Astronomical Society Meeting 201*. 2003.

41. Rizos, Chris. *Principles and Practice of GPS Surveying*. Technical Report, Satellite Navigation and Positioning Group, University of New South Wales, Sydney, Australia, 1999. http://www.gmat.unsw.edu.au/snap/gps/gps.

42. R.R. Bate, D.D. Mueller and J.E. White. *Fundamentals of Astrodynamics*. New York, NY: Dover Publications, Inc., 1971.

43. Sheikh, Suneel I., "Telephone Conversations and Meetings with the Space Systems Laboratory, University of Maryland." February 2004 - March 2005.

44. Sheikh, Suneel I., Darryll J. Pines, Paul S. Ray, Kent S. Wood, Michael N. Lovel-lette, and Michael T. Wolff. "The Use of X-ray Pulsars for Spacecraft Naviga-tion." *14th AAS/AIAA Space Flight Mechanics Conference*. February 2004. AAS 04-109.

45. Shemar, S., G. Bond, P. Edmonds, B. Ashforth, and S. Harding. "Trial Results of a Prototype System to Locate GPS Radio Interference Sources Using Time-Difference-Of-Arrival Measurements." *Proceedings of the ION National Technical Meeting*. 1018–1025. January 2004.

46. Splaver, Eric M. *Long-Term Timing of Millisecond Pulsars*. Doctoral Disserta-tion, Princeton University, Novemeber 2004.

47. Stairs, Ingrid H. *Testing General Relativity with Pulsar Timing*. Technical Report, University of British Columbia, September 2003. www.livingreviews.org/lrr-2003-5.

48. Storz, Mark, "Private Communications." Headquarters Air Force Space Com-mand/XPYE.

49. Taylor, J.H. and M.F. Ryba. "High Precision Timing of Millisecond Pulsars. 1 . Long Term Monitoring of PSRs B1855+09 and B1937+21," *The Astrophysical Journal*, *371* (1991a).

50. Vallado, David A. *The Fundamentals of Astrodynamics and Applications*. New York: The McGraw-Hill Companies, Inc., 1997.

51. V.M. Kaspi, M. Roberts and A. Harding. "Isolated Neutron Stars," *eprint arXiv:astro-ph/0402136* (February 2004). To appear in *Compact Stellar X-ray Sources, eds. W.H.G. Lewin and M. van der Klis.*

52. *Wiesel, William E.* Modern Orbit Determination. *Beavercreek, OH: Aphelion Press, 2003.*

53. *Wolf, Robert.* Satellite Orbit and Ephemeris Determination using Intersatellite Links. *Doctoral Dissertation, University of the Federal Armed Forces Munich, 2000. http://137.193.200.177/ediss/wolf-robert/inhalt.pdf.*

54. *Wood, K.S. "Navigation Studies Utilizing the NRL-801 Experiment and the AR-GOS Satellite."* Small-Satellite Technology and Applications III, Proceedings of the International Society for Optical Engineering. *105–116. April 1993.*

55. *Zablotney, J.H., D.D. Husch, K.M. Rowe, and J. Discenza. "An Accurate Search and Rescue Location System."* Proceedings of the Forty-Seventh Annual Meeting, "Navigation and Exploration". *459. June 1991.*

1. REPORT DATE (DD-MM-YYYY) 21-03-2005	2. REPORT TYPE **Master's Thesis**	3. DATES COVERED (From – To) August 2003 – March 2005

4. TITLE AND SUBTITLE	5a. CONTRACT NUMBER
The Use of X-Ray Pulsars for Aiding GPS Satellite Orbit Determination	5b. GRANT NUMBER
	5c. PROGRAM ELEMENT NUMBER

6. AUTHOR(S)	5d. PROJECT NUMBER
Woodfork, Dennis W., II, Captain, USAF	5e. TASK NUMBER
	5f. WORK UNIT NUMBER

7. PERFORMING ORGANIZATION NAMES(S) AND ADDRESS(S) Air Force Institute of Technology Graduate School of Engineering and Management (AFIT/EN) 2950 Hobson Way WPAFB OH 45433-7765	8. PERFORMING ORGANIZATION REPORT NUMBER AFIT/GA/ENG/05-01

9. SPONSORING/MONITORING AGENCY NAME(S) AND ADDRESS(ES) HQ AFSPC/XPYA Attn: Dr. Robert A. Racca 1150 Vandenberg St, Suite 1105 Peterson AFB, CO 80914-4650 DSN: 834-3714	10. SPONSOR/MONITOR'S ACRONYM(S)
	11. SPONSOR/MONITOR'S REPORT NUMBER(S)

12. DISTRIBUTION/AVAILABILITY STATEMENT
        APPROVED FOR PUBLIC RELEASE; DISTRIBUTION UNLIMITED.

13. SUPPLEMENTARY NOTES

14. ABSTRACT
This research proposes the use of an existing "signal of opportunity" – namely x-ray pulsars – to improve the accuracy and robustness of the GPS satellite and clock estimation algorithm. Improvement in satellite and clock accuracy results in a direct benefit to the user. A simulation has been developed to determine the effects of using x-ray pulsar measurements on the GPS Operational Control Segment. The epoch-specific position, velocity, and clock errors of all GPS satellites in the constellation were estimated using both pseudoranges and time-difference-of-arrival (TDOA) measurements from pulsars. The primary measure of accuracy is a constellation Signal-In-Space Range Error (SISRE). Results indicate that marginal SISRE improvements (approximately 1%) can be achieved if the x-ray detector is accurate to an order of approximately 40 m for the strongest pulsar. Increasing the accuracy of the x-ray detector by a factor of 100 can yield accuracy improvements up to 26% over the pseudorange-only based GPS system. Additionally, results show that using only 1 strong pulsar to create TDOA observations, may be comparable to using tens of weakly timed pulsars. Pulsar geometry analysis showed that the geometry does have a significant impact on the overall system performance. Results indicate that using TDOAs in the absence of pseudoranges may aid the OCS in keeping track of the GPS satellites until the ground station links can be reestablished.

15. SUBJECT TERMS
Global Positioning System, Pulsars, X rays, Least Squares Method, Time, Arrival, Stars, Kalman Filtering

16. SECURITY CLASSIFICATION OF:			17. LIMITATION OF ABSTRACT	18. NUMBER OF PAGES	19a. NAME OF RESPONSIBLE PERSON Dr. John F. Raquet
REPORT **U**	ABSTRACT **U**	c. THIS PAGE **U**	**UU**	168	19b. TELEPHONE NUMBER (Include area code) (937) 255-6565, ext 4580; e-mail: john.raquet@afit.edu